PROCEEDINGS OF
UGSAS-GU & BWEL
JOINT POSTER SESSION ON AGRICULTURAL AND BASIN WATER ENVIRONMENTAL SCIENCES
2022

ORGANIZERS:

THE UNITED GRADUATE SCHOOL OF AGRICULTURAL SCIENCE
GIFU UNIVERSITY

GIFU UNIVERSITY REARING PROGRAM
FOR BASIN WATER ENVIRONMENTAL LEADERS

CO-ORGANIZER:
INTERNATIONAL CONSORTIUM OF UNIVERSITIES IN SOUTH AND SOUTHEAST ASIA FOR THE DOCTORAL EDUCATION IN AGRICULTURAL SCIENCE AND BIOTECHNOLOGY (ICGU12)

Date: November 9, 2022

UGSAS-GU & BWEL Joint Poster Session on Agricultural and Basin Water Environmental Sciences 2022

Organized by The United Graduate School of Agricultural Science, Gifu University (UGSAS-GU)
Gifu University Rearing Program for Basin Water Environmental Leaders (BWEL)

PROGRAM

Wednesday, November 9
Time: 15:00-17:15

Timetable

15:00-15:05 **Opening remarks**
Prof. Ken Hiramatsu (Dean of UGSAS-GU)

15:10-16:45 **Online poster presentation**

Poster Core Time
Odd numbered posters：15:10-15:50
Even numbered posters：15:50-16:30
Free discussion time：16:30-16:45

16:45-16:50 **Announcement of the winners of the Best Presentation Award**

17:00-17:10 **Best Presentation Award ceremony**

17:10-17:15 **Closing remarks**
Prof. Fusheng Li (Head of the Promotion Office of BWEL)

Presentations

P01: Soil phosphate and potassium solubilization and *Fusarium oxysporu*m inhibition potential of soil fungi isolated from melon (*Cucumis melo*) rhizosphere in Central Java, Indonesia
Desti Dian Amalina (Faculty of Agriculture, Sebelas Maret University, Indonesia; Graduate School of Natural Science and Technology, Gifu University)

P02: Ensemble learning approach to predict soybean yield using UAV-based imagery and weather data
Luthfan Nur Habibi (UGSAS-GU)

P03: Study on the relationship between intumescence injury and calcium supply among several tomato cultivars
Natassia Clara Sita (UGSAS-GU)

P04: Microbial fuel cell on different cultivation systems to reduce N_2O and CH_4 emission in Indonesia
Adhia Azhar Fauzan (UGSAS-GU)

P05: Sustainable pesticide management: Personalized simulation for Indian soil
Kishalay Chakraborty (UGSAS-GU)

P06: Rice yield prediction using UAV-based imagery and deep learning
Md. Suruj Mia (UGSAS-GU)

P07: Effects of transglutaminase on pasting properties and retrogradation of rice flour
Dang Thi Kim Lien (UGSAS-GU)

P08: Dissecting the role of N and S in Arabidopsis root architecture under Al stress through physio-genetics approach
Md. Abir Ul Islam (UGSAS-GU)

P09: Effect of exogenous gibberellin on regreening in Valencia orange fruit
Nichapat Keawmanee (UGSAS-GU)

P10: A coupled TOPMODEL-soil erosion model (TOPEROS): Towards having a compact decision support tool for evaluating hydrological ecosystem services
Emmanuel Okiria (UGSAS-GU)

P11: Evaluation of physical and antioxidant properties of chitosan-based films combing with curcumin nanoemulsion
Fakfan Luangapai (UGSAS-GU)

P12: Evaluation of the impact of climate change on river temperature
Khadiza Akter Mousumi (UGSAS-GU)

P13: Fate of plastic mulch residues in agricultural soil and its influence on soil property response to soil amendment addition
Shiamita Kusuma Dewi (UGSAS-GU; BWEL)

P14: Highly accurate estimation of swell components using wave model
Shota Iguchi (Graduate School of Natural Science and Technology, Gifu University)

P15: High-resolution analysis of atmospheric optical fluctuations for laser communication using WRF model
Naoya Shimpuku (Graduate School of Natural Science and Technology, Gifu University)

P16: Antibiotic resistance genes and 16S rDNA in large *Johkasou* treating residential area domestic wastewater
Haoning Su (Graduate School of Engineering, Gifu University; BWEL)

P17: Statistical analysis of solar radiation under future climate in Chubu region
Tomoki Kitaoka (Graduate School of Natural Science and Technology, Gifu University)

P18: Diagnosis of soil fertility by remote sensing data and GIS
Jieli Zhou (Graduate School of Natural Science and Technology, Gifu University; BWEL)

P19: Potential hosts and transfer of As, Cr, and Pb-induced resistance genes in soil under coal mining disturbance
Yajie Wang (Graduate School of Engineering, Gifu University)

P20: Can activated carbon allow antibiotic resistance genes to access into its pores
Sri Anggreini (Graduate School of Engineering, Gifu University; BWEL)

P21: Improvement of membrane filtration performance by pre-coating with powdered activated carbon
Wenqing Li (Graduate School of Natural Science and Technology, Gifu University; BWEL)

P22: Effect of bacteria on *Uroglena* sp. growth in surface water
Ramayandi (Graduate School of Engineering, Gifu University)

CONTENTS

Soil phosphate and potassium solubilization and *Fusarium oxysporum* inhibition potential of soil fungi isolated from melon (*Cucumis melo*) rhizosphere in Central Java, Indonesia

Desti Dian Amalina[1], Sudadi[1], Widyatmani Sih Dewi[1], Hadiwiyono[2], Ningrum Meliyani Pratama[1], Nadia Ismah Nur Rilansari[1], Rosalinda Hayyin Ayu Arsita[1], Komariah[1] and Haruhisa Suga[3]

1. **Department of Soil Science, Faculty of Agriculture, Sebelas Maret University, Jalan Ir. Sutami 36A Surakarta, Indonesia 57126**
2. **Department of Agrotechnology, Faculty of Agriculture, Sebelas Maret University, Jalan Ir. Sutami 36A Surakarta, Indonesia 57126**
3. **Institute for Glyco-core Research (iGCORE), Gifu University, 1-1 Yanagido, Gifu 501-1193, Japan**

INTRODUCTION

Melon (*Cucumis melo*) is one of important fruit crops in Indonesia. Melon production was 92,446 tons (15,724 ha) in 2017 and 118,708 tons (6,773 ha) in 2018, that makes Indonesia being the one of the largest melons producing country in Southeast Asia (Badami et al. 2020). However, that number only meets about 40% of domestic needs (Annisa and Gustia2017). Farmers usually use chemical fertilizers to increase melon yields, which in long term and continuous use will lead to many disadvantages for soil and environment. Plant growth will be disrupted, and melon yield will decrease. Therefore, we need to change the pattern of cultivation that leads to natural resources conservation and reduce soil quality degradation by utilizing the soil beneficial microbes.

Melon needs a huge amount of nutrition for its growth. Phosphorus (P) and potassium (K) are the essential nutrients and required for all life stages of plant. P is being a structural constituent of nucleic acid, as well as being involved in metabolic energy transfer through Adenosine triphosphate (Olaniyi 2008) while K is involved in photosynthesis, photophosphorylation enzyme activation, turgor maintenance and stress tolerance. Adequate K nutrition has also been associated with increased yields, fruit size and many things that determined the fruit quality (Lester et al. 2010). These two nutrients are very important but their availability in soil is often very low so they need the help of soil microbes to dissolve them.

Melon plants are very susceptible to wilt disease caused by *Fusarium oxysporum*. This disease will reduce the yield and quality of the fruit and even fail to harvest (Oumouloud et al.2013). The fungus *F. oxysporum* is a soil-borne pathogen that can survive for more than 10 years in the form of chlamydiospores in the soil (Rahman et al. 2021). This makes the disease quite difficult to control. Farmers usually used chemical compounds to control this disease However, many negative impacts such as environmental pollution, soil poisoning, and soil degradation came from that (Zhao et al. 2011)

Biological control with soil microbes can be the alternative treatment to control the Fusarium wilt disease. Many antagonistic strains have been proved to be effective biocontrol agents in controlled laboratory or greenhouse conditions (Zhao et al. 2011). One of the microorganisms that used for the biological control is a group of rhizosphere fungi, such as species of the genera *Trichoderma*, *Penicillium*, *Fusarium*, and *Phoma*, which have ability to stimulate the plant immune response upon enemy attack and growth promotion in crop (Jogaiah et al. 2013). The aims of this study are to investigate the rhizosphere fungi that have a beneficial effect for phosphate and potassium solubilization and antagonistic potential to *F. oxysporum* in melon crop.

METHODS

This research was conducted in Laboratory of Soil Biology and Biotechnology, Faculty of Agriculture, Sebelas Maret University, Indonesia from April-August 2022.

Soil Sampling—Soil samples were taken by random sampling with the survey method. Soil sampling was conducted on melon plantation owned by melon farmers in three locations (Table 1). Soil samples were taken randomly at 4 points in each cardinal point and replicated 3 times with a depth of 10—15 cm in the root zone.

Table 1: Description of the soil sampling location

Location	Coordinates	Altitude (m asl)	Soil Type
Wonogiri Regency	7º57'9.37" S 110º52'33.01" E	168	Vertisol
Sragen Regency	7º28'56,12" S 110º57'45,66" E	130	Vertisol
Karanganyar Regency	7º37'50.82" S 110º56'54.52" E	195	Alfisol

The isolation of soil fungi—The isolation of soil fungi was conducted using the dilution method on PDA media. Five grams of soil was diluted in 45 ml of physiological solution and shaken until homogenous. The suspension then diluted by 10^{-5}. The suspension in the 10^{-3} and 10^{-5} dilutions was taken as much as 0.1 ml using a sterile pipette and then spread into a Petri-dish that already contained PDA media and leveled using a dry glass. The isolation was replicated 2 times for each soil sample. The Petri-dish was packed with wrapping paper and incubated at room temperature for 7 days.

Ability to solubilize P and K—Identification of the ability to solubilize P and K was conducted by placing the purified fungi isolates into the specific media, namely Pikovskaya for P and Alexandrof for K. The fungi that have the ability to solubilize P and/or K are characterized by the presence of a clear zone/halo zone that appear in the media around the growing colonies.

Antagonistic potential—The antagonistic potential analysis was carried out by biculture antagonistic test by placing the purified fungi isolates and the *F. oxysporum* isolates side by side on PDA. The *F. oxysporum* isolates obtained from the Laboratory of Plant Pests and Disease, Faculty of Agriculture, Gadjah Mada University, Indonesia. Observation was conducted 7x24 hours after the isolate was incubated by observing the growth direction of the fungi colony and *F. oxysporum*.

RESULTS AND DISCUSSION

The results of this research shown that three isolates have the potency to solubilize phosphate, five isolates have the ability to solubilize potassium, and six isolate have the ability to inhibit

the growth of *F. oxysporum* (Table 2). This means that the fungi from the melon rhizosphere have the potency to be developed into biofertilizer to help provide the soil nutrients and biological agents against the Fusarium wilt disease.

Table 2: Ability of the fungal isolates to solubilize nutrient and to inhibit the growth of *Fusarium oxysporum*

Isolate	Origin	Ability to solubilize nutrient		Percentage to inhibit *F. oxysporum*
		P	K	
KRA 1A	Karanganyar	-	+	25.00%
KRA 1C	Karanganyar	-	-	69.17%
KRA 3A	Karanganyar	+	+	8.33%
WNG 2B	Wonogiri	-	+	0%
SRG 1A	Sragen	+	+	20.83%
SRG 1C	Sragen	-	+	25.00%
SRG 1B	Sragen	-	-	55.83%
SRG 3B	Sragen	-	-	0%
SRG 3A	Sragen	+	-	0%

Ability to solubilize P and K—Formation of the clear zone around the colony on the Pikovskaya (Fig. 1) and Alexandrof (Fig. 2) medium indicated the ability of rhizosphere fungi to solubilize phosphate and potassium.

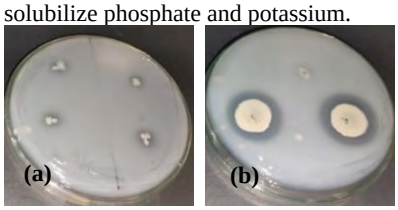

Fig. 1: The halo zones appeared on Pikovskaya media indicated that the isolates SRG 3A (a) and KRA 3A (b) have the ability to solubilize phosphate.

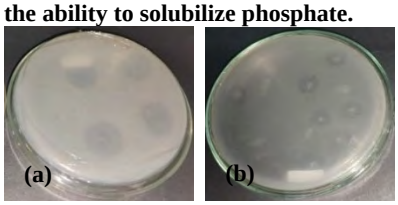

Fig. 2: The halo zones appeared on Alexandrof media indicated that the isolates SRG 1A (a) and WNG 2B (b) have the ability to solubilize potassium.

Antagonistic potential—The antagonistic activity of rhizosphere fungi against *F. oxysporum* that was grown on the PDA showed that six of the nine isolates produced inhibitory zones, this means that the six isolates could inhibit the growth and development of the *F. oxsysporum* (Fig. 3). The formation of inhibitory zones indicated the existence of antimicrobial or antibiotic mechanisms of rhizosphere fungal isolates against *F. oxysporum* (Meike Jaya and Joko 2020). The percentage of ability to inhibit the growth of *F. oxysporum* was shown in Table 2. Isolate that has the highest ability to inhibit *F. oxysporum* is KRA 1C (69.17%).

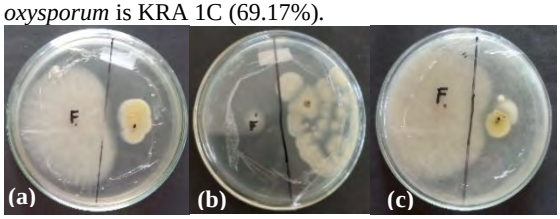

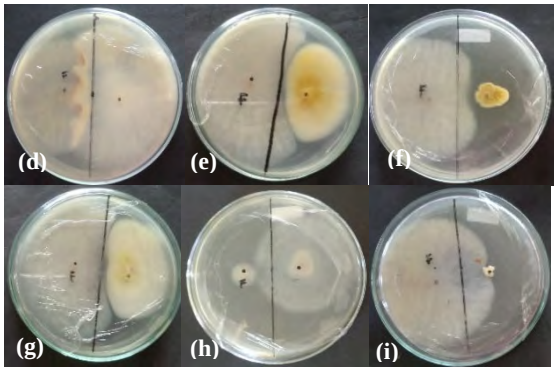

Fig. 3: *In vitro* antagonistic activity of rhizosphere fungi by the biculture method against *F. oxysporum* (a) KRA 1A (b) KRA 1C (c) KRA 3A (d) WNG 2B (e) SRG 1A (f) SRG 1C (g) SRG 1B (h) SRG 3B (i) SRG 3A

ACKNOWLEDGMENTS

The authors would like to thank Sebelas Maret University, which funded part of this research through the Mandatory Research scheme for non-APBN funds for the fiscal year 2022.

REFERENCES

Annisa, P. and Gustia, H. (2017) Response of Growth and Production of Melon Plants to Liquid Organic Fertilizer Tithonia Diversifolia. Proceeding Nasional Seminar 2017, Faculty of Agriculture UMJ, 104–114.

Badami, K., Daryono, B. S., Amzeri, A., and Khoiri, S. (2020). Combining Ability and Heterotic Studies on Hybrid Melon (*Cucumis melo* L.) Populations for Fruit Quality Traits. SABRAO Journal of Breeding and Genetics 52(4):402-417.

Jogaiah, S., Abdelrahman, M., Tran, L. S. P., and Shin-Ichi, I. (2013). Characterization of Rhizosphere Fungi that Mediate Resistance in Tomato Against Bacterial Wilt Disease. Journal of Experimental Botany, 64(12):3829-3842.

Lester, G. E., Jifon, J. L., and Makus, D. J. (2010). Impact of Potassium Nutrition on Postharvest Fruit Quality: Melon (*Cucumis melo* L) Case Study. Plant and Soil 335(1):117–131.

Meike Jaya, R., and Joko, T. (2020). Plant Growth Promoting and Antagonistic Potential of Endophytic Bacteria Isolated from Melon in Indonesia. Plant Pathology Journal 19(3): 200–210.

Olaniyi, J. O. (2008). Growth and Seed Yield Response of Egusi Melon to Nitrogen and Phosphorus Fertilizers Application. Journal of Sustainable Agriculture 2(3):255–260.

Oumouloud, A., El-Otmani, M., Chikh-Rouhou, H., Claver, A. G., Torres, R. G., Perl-Treves, R., and Álvarez, J. M. (2013). Breeding Melon for Resistance to Fusarium Wilt: Recent Developments. Euphytica 192(2):155–169.

Rahman, M. Z., Ahmad, K., Kutawa, A. B., Siddiqui, Y., Saad, N., Geok Hun, T., Hata, E. M., and Hossain, M. I. (2021). Biology, Diversity, Detection and Management of *Fusarium oxysporum* f. sp. *niveum* Causing Vascular Wilt Disease of Watermelon (*Citrullus lanatus*): A Review. Agronomy 11(1310):1-24.

Zhao, Q., Dong, C., Yang, X., Mei, X., Ran, W., Shen, Q., and Xu, Y. (2011). Biocontrol of Fusarium Wilt Disease for *Cucumis melo* Melon Using Bio-organic Fertilizer. Applied Soil Ecology 47: 67–75.

Ensemble learning approach to predict soybean yield using UAV-based imagery and weather data

Luthfan Nur Habibi[1], Tsutomu Matsui[2] and Takashi S.T. Tanaka[2, 3]

1. **The United Graduate School of Agricultural Science, Gifu University, 1-1 Yanagido, Gifu 501-1193, Japan**
2. **Faculty of Applied Biological Sciences, Gifu University, 1-1 Yanagido, Gifu 501-1193, Japan**
3. **Artificial Intelligence Advanced Research Center, Gifu University, 1-1 Yanagido, Gifu 501-1193, Japan**

INTRODUCTION

Estimating soybean yield is key to improving farm management practices through precision agriculture. Remote sensing information such as spectral reflectance and vegetation indices (VIs) derived from Unmanned Aerial Vehicle (UAV) imagery has been proven to give precise information on grain yield. However, spectral reflectance and VIs often have a high linear correlation with each other. Consequently, appropriate feature selection is required to construct the robust prediction model. Moreover, the inclusion of weather data into yield prediction model may be valuable in improving the prediction accuracy. Therefore, this study aimed to explore the yield prediction model's performance using VIs and weather data.

Many researchers reported that machine learning algorithms have been a more robust and efficient approach than conventional statistical analysis in predicting crop yield. Ensemble learning technique combines several regression learners to address overfitting problems caused by single predictive models (Yoosefzadeh-Najafabadi et al., 2021). Thus, this study further aimed to evaluate the effectiveness of ensemble learning on the model accuracy to predict soybean yield.

MATERIALS AND METHODS

Field data collection – Soybean yields were surveyed with 462 samples taken from seven soybean fields between 2018 and 2021 in Gifu Prefecture, Japan, during the maturity stage. All surveyed soybean samples have the same cultivar named 'Fukuyutaka'. Spectral data from UAV-based imagery were also taken from each field using two camera platforms, Parrot Sequoia+ (2018–2019) and Altum MicaSense (2021), during two growing stages (R2 and R5). Moreover, weather data were collected from the Agro-Meteorological Grid Square Data, NARO (https://amu.rd.naro.go.jp/).

Analysis of UAV-based imagery – Vegetation indices calculated from UAV-based imagery spectral data were selected based on the Index Database (https://www.indexdatabase.de/). In this research, we only consider three bands (Green, Red, and Near-InfraRed) from the UAV imagery. A total of 64 features were extracted from UAV-based imagery data, including six raw bands and 58 VIs from two growing stages.

Feature selection techniques – A combination of UAV-based imagery and weather data features creates a high-dimensional data set (106 features). Feature selection is a process of selecting a subset of variables that contribute to the response. In this research, three types of feature selection were performed:

1. Maximum Relevance Minimum Redundancy (MRMR). MRMR is a filtering-based feature selection which selects the relevant features while controlling for the redundancy within the selected features (Zhao et al., 2019).
2. Sequential Backward Search (SBS). This algorithm automatically selects a subset of features from all features and eliminates the one which minimizes performance (Shafiee et al., 2021)
3. Recursive Feature Elimination (RFE). RFE is a wrapper-based feature selection method which selects a subset of variables according to the performance criteria of the regression learner (Corrales et al., 2022). Importance values from random forest regression were selected as the criteria.

Multicollinearity tests using the Variance Inflation Factor (VIF) values were performed after the selection procedures.

Data analysis and statistics – The model accuracy was compared among five models, including three base learners (e.g., Random Forest, XGBoost, and Lasso Regression), stacked ensemble, and averaging-based ensemble. Lasso regression was used as a super learner in staked ensemble model. Accuracy assessment of the established models was conducted using three different methods of nested cross-validation, including:

1. Leave-one-out of field (LOO-F)
2. Clustering-based spatial cross-validation (CS-CV)
3. Random cross-validation (R-CV)

The best model was evaluated based on the coefficients of determination (R^2) and root mean square error (RMSE).

RESULTS AND DISCUSSION

Feature selection – The feature selection aimed to reduce the explanatory variables that could be redundant to the prediction model, which reduce the model's capability. The original feature sets contain many collinear variables from the VIs and weather data. The results from the three feature selection algorithms resulted in different sets of variables, as presented in Table 1 and Figure 1. MRMR chose the largest set of features with 11 features. In contrast, SBS and RFE chose only 7 and 4 features, respectively. All feature selection algorithms could remove perfectly collinear variables that previously existed in the original data set. However, all model subsets still select collinear features reflected from the VIF values that exceeds the standard value (below 10).

Table 1. Feature selection and multicollinearity results.

Feature selection method	Selected variables	VIF range
Maximum Relevance Minimum Redundancy (MRMR)	11	5.21 – 24.57
Sequential Backward Search (SBS)	7	1.84 – 43476
Recursive Feature Elimination (RFE)	4	3.02 – 392

Two features from UAV-based imagery data, CI_{green} (R5) and $NORM_{green}$ (R5) were selected by all methods, indicating the importance of these features to the yield. Herrero-Huerta et al., (2020) also found that CI_{green} in the R5 growth stage was an important covariate to predict soybean yield as it represents the canopy chlorophyll content. Regarding to weather data, only three features out of 48 were selected, that is median value of solar radiation (at vegetative stage) and minimum value of mean temperature (at reproductive stage) selected by MRMR, and maximum value of mean temperature (at vegetative stage) from SBS.

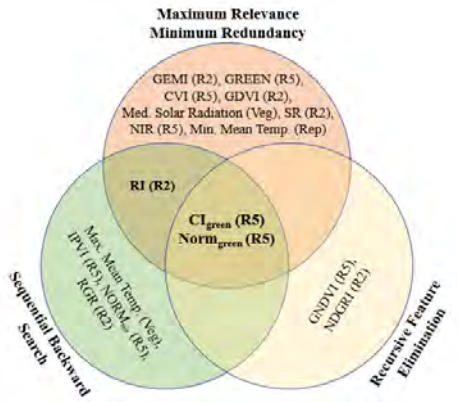

Fig. 1: Venus diagram of variables selected by feature selection methods.

Yield prediction model – Table 2 shows the prediction accuracy of yield models from five regression learners with three validation approaches. Overall, the yield was predicted with RMSE values ranging from 53.54 to 274.39 kg/ha. The best model was SBS-random forest R-CV model. Figure 2 shows an example of a predicted yield map.

Feature selection affected the accuracy of yield prediction models. The model using variables selected by RFE performed the best in the LOO-F approach. However, MRMR and SBS performed better than RFE models in CS-CV and R-CV approaches. The availability of weather variables in SBS and MRMR models might improve the overall accuracy of models because any weather data was not selected in RFE.

On average, models validated using the R-CV approach gave the best results. However, in recent studies, many researchers contend to use spatial CV method as it also accounts for the spatial autocorrelation of response variables, which could bias prediction maps, even though this idea is still controversial (Wadoux et al., 2021). On the other hand, validating the model using truly independent test data set, as we used in LOO-F, might be the most reasonable way to validate the prediction model in real practice.

Our main interest in this research was to explore the effectiveness of ensemble learning technique. According to the results, single learners outperformed the ensemble learners in almost of all cases. This result contradicted with common findings in the literature (Yoosefzadeh-Najafabadi et al., 2021). Simple learners such as Lasso regression could perform better if the objective is map extrapolation, as exhibited in the LOO-F model approach. However, if the aim is to interpolate yield maps, a complex model from machine learning and an ensemble model might be the appropriate method.

In conclusion, feature selection approaches can be used to reduce redundancy and highlight important features from VIs and weather data to predict soybean yield. Moreover, a simple statistical method might still be meaningful for predicting yield aside from complex statistical algorithms from machine learning.

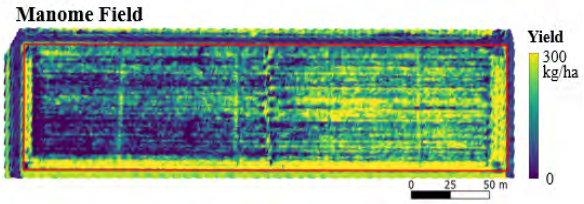

Fig. 2: Example of predicted yield map from MRMR-random forest model with CS-CV approach.

REFERENCES

Corrales, D.C., Schoving, C., Raynal, H., Debaeke, P., Journet, E.P., Constantin, J., (2022). A surrogate model based on feature selection techniques and regression learners to improve soybean yield prediction in southern France. Comput. Electron. Agric. 192.

Herrero-Huerta, M., Rodriguez-Gonzalvez, P., Rainey, K.M., (2020). Yield prediction by machine learning from UAS-based mulit-sensor data fusion in soybean. Plant Methods 16, 1–16.

Shafiee, S., Lied, L.M., Burud, I., Dieseth, J.A., Alsheikh, M., Lillemo, M., (2021). Sequential forward selection and support vector regression in comparison to LASSO regression for spring wheat yield prediction based on UAV imagery. Comput. Electron. Agric. 183, 106036.

Wadoux, A.M.J.C., Heuvelink, G.B.M., de Bruin, S., Brus, D.J., (2021). Spatial cross-validation is not the right way to evaluate map accuracy. Ecol. Modell. 457.

Yoosefzadeh-Najafabadi, M., Earl, H.J., Tulpan, D., Sulik, J., Eskandari, M., (2021). Application of Machine Learning Algorithms in Plant Breeding: Predicting Yield From Hyperspectral Reflectance in Soybean. Front. Plant Sci. 11, 1–14.

Zhao, Z., Anand, R., Wang, M., (2019). Maximum relevance and minimum redundancy feature selection methods for a marketing machine learning platform. Proc. - 2019 IEEE Int. Conf. Data Sci. Adv. Anal. DSAA 2019 442–452.

Table 2. Results of regression learners trained with subset of variables selected by feature selection methods and different validation approaches.

Model subset	Leave-one-out of field		Clustering spatial-CV		Random CV	
	R^2	RMSE	R^2	RMSE	R^2	RMSE
Maximum Relevance Minimum Redundancy (MRMR)						
Random Forest	0.22	68.67	**0.66**	**54.21**	0.68	53.58
XGBoost	0.15	72.88	0.65	54.62	0.66	54.96
Lasso	0.36	61.24	0.65	54.43	0.66	54.67
Ensemble stacking	-48.46	274.39	0.64	55.13	0.67	54.23
Ensemble averaging (equal weight)	0.29	65.62	0.60	58.94	0.67	54.29
Sequential Backward Search (SBS)						
Random Forest	0.24	64.11	0.65	54.61	**0.68**	**53.54**
XGBoost	0.27	66.62	0.66	54.35	0.64	56.38
Lasso	0.36	60.01	0.64	55.26	0.66	54.77
Ensemble stacking	0.17	68.21	0.65	54.44	0.67	54.21
Ensemble averaging (equal weight)	0.32	61.31	0.60	59.26	0.67	54.93
Recursive Feature Elimination (RFE)						
Random Forest	0.33	62.45	0.62	57.28	0.64	55.98
XGBoost	0.23	68.31	0.59	59.07	0.56	62.26
Lasso	**0.40**	**58.38**	0.63	55.91	0.65	55.42
Ensemble stacking	0.32	63.24	0.63	55.73	0.66	55.09
Ensemble averaging (equal weight)	0.35	61.03	0.57	61.52	0.65	56.60

The best models for each case are highlighted with bold letters

Study on the relationship between intumescence injury and calcium supply among several tomato cultivars

Natassia Clara Sita[1,2], Asuka Kousaka[2], Risa Tamoi[2], Chiaki Ozawa[3], Yoshikazu Kiriiwa[2,3] and Katsumi Suzuki[2,3]

1. **The United Graduate School of Agricultural Science, Gifu University, 1-1 Yanagido, Gifu-shi, Gifu 501-1193, Japan**
2. **Department of Bioresource Sciences, Faculty of Agriculture, Shizuoka University, 836 Ohya, Suruga, Shizuoka 422-8529, Japan**
3. **Graduate School of Integrated Science and Technology, Shizuoka University, 836 Ohya, Suruga, Shizuoka 422-8529, Japan**

INTRODUCTION

Intumescence injury is a physiological disorder characterized by irregular outgrowth and elongated epidermal or parenchymal cells on the adaxial and/or abaxial surface of leaves. In tomatoes, this phenomenon occurs when ultraviolet (UV) light is lacking and the humidity is high, and the severity increases over time (Suzuki et al., 2020). Calcium (Ca) is a macronutrient that serves as an intracellular messenger, as well as providing structural support for the cell wall and membranes (Marschner, 1995; White and Broadley, 2003). According to previous studies, there were variances in the occurrence of intumescence injury across various tomato cultivars (Ozawa et al. 2018), and this incidence was discovered to be a Ca-related injury (Schabow and Palta, 2019). Ca foliar spray was found to repress the incidence of blossom-end rot in tomatoes (Mazumder et al., 2021), but its effect on intumescence injury was still unknown. This study aimed to investigate the relationship between Ca supply and intumescence injury among various tomato cultivars and to mitigate intumescence injury in tomatoes by Ca foliar spray.

MATERIALS AND METHODS

Experiment 1: Six different cultivars of tomato (*Solanum lycopersicum*) were used in this study (Fig. 1). After 7 days of sowing, the seedlings were transferred into artificial climate chamber and were supplied from the bottom with nutrient solution (Ohtsuka Ekihi SA formula ½). The treatment was started after one week of cultivation, with three different Ca concentration, which were 0.5 me (low Ca), 4.5 me (control) and 14.5 me (high Ca). Tomatoes were conditioned in high humidity and lack of UV irradiance, and intumescence injury was observed after 3 days. Experiment 2: The Ca foliar spray experiment was performed using cultivar 'CF Rinka 409'. In this experiment, tomatoes were conditioned under low UV and high humidity conditions for 7 days. The Ca foliar spray solution was sprinkled into adaxial and abaxial surface of tomato leaves with five different treatments: no spray (control), DW (distilled water spray), Ca-1x (spray once), Ca-2x (spray once every three days) and Ca-7x (daily spray for a week). To investigate the intumescence injury, tomato leaves were stained by Toluidine blue O, scanned, and the degree of intumescence was calculated as the percentage of stained leaf area using ImageJ software. Ca concentration in tomato shoots was quantified by using Inductively Coupled Plasma (ICP) Spectrometer in both experiments.

RESULTS AND DISCUSSION

Intumescence injury is a physiological disorder that commonly occurs in the Solanaceae family of plants, including tomatoes (Lang and Tibbitts, 1983), potatoes (Douglas, 1907), and sweet potatoes (Craver et al., 2014). Previous study in Russet Burbank potato suggested that intumescence injury is related with the Ca concentration in the leaf (Schabow and Palta, 2019). In this study, it was clarified that Ca concentration in the shoot is related to the intumescence injury on tomato leaves.

The cultivar variations tomato shoot Ca content and susceptibility to intumescence injury under various Ca concentration supplies were described in Fig 1. Based on their sensitivity to intumescence injury, tomatoes were divided into three groups: tolerant ('CF Momotaro York' and 'Momotaro Select'), moderate ('Momotaro Natsumi' and 'Misora 64'); and sensitive ('CF Rinka 409' and 'Reika'). When subjected to low Ca concentrations, the sensitive cultivars suffered from high degree of intumescence injury while the moderate cultivars developed less. However, despite the low Ca level in tomato shoots, tolerant cultivars only had minimum degree of intumescence. Along with the increasing concentration of Ca supply, the degree of intumescence injury decreased in all cultivars. This experiment showed that Ca concentration treatment significantly affected the Ca content in the shoot and the degree intumescence injury. According to a previous study about the use of supplemental addition of Ca to reduce intumescence injury in Russet Burbank potatoes (Schabow and Palta, 2019), application of a high Ca concentration supply can lower the incidence of intumescence injury in tomatoes.

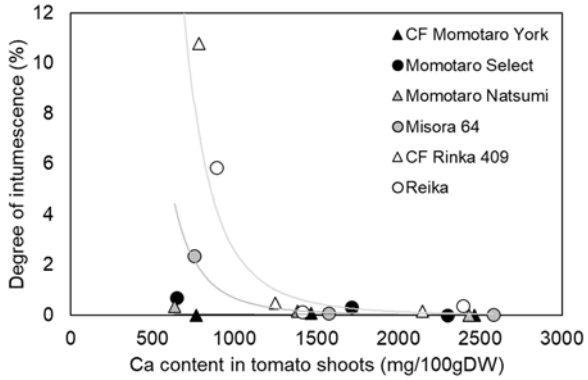

Fig. 1: Cultivar differences in susceptibility to intumescence injury and Ca content of tomato shoots at different Ca concentration supplies. (Black: tolerant cultivars; grey: moderate cultivars; white: sensitive cultivars).

The effect of Ca-spray on the intumescence injury in tomato shoots of cultivar 'CF Rinka 409' was also examined (Fig 2). The intumescence injury was found highest when no foliar Ca was applied, and daily application of Ca spray will significantly reduce this incidence. According to Kumazaki et al. (2010) in Ueno et al. (2018), spraying leaves with a potassium (K) solution helps prevent leaf tips from dying from a K deficit. With a regular supply of foliar Ca, intumescence injury in the present study was greatly reduced. Therefore, it is

recommended that the frequency of foliar spraying be increased.

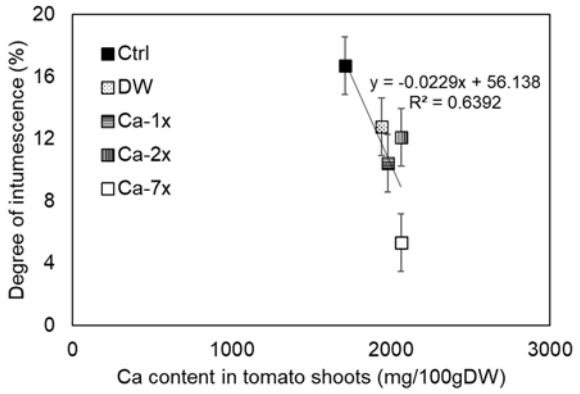

Fig 2: Correlation between Ca content and intumescence injury in tomato leaves with foliar Ca spray applied. (Ctrl: no foliar spray; DW: distilled water foliar spray; Ca-1x: Ca foliar spray once in a week; Ca-2x: Ca foliar spray twice in a week; Ca-7x: daily Ca foliar spray for one week).

Based on the experiment, it can be concluded that different cultivars of tomato developed different degree of intumescence injury susceptibility, and Ca concentration supplies affected their severity The application of Ca foliar spray was also found to reduce the intumescence injury incidence in tomatoes.

REFERENCES

Craver, J. K., Miller, C. T., Williams, K. A., and Boyle D. L. (2014) Characterization And Comparison of Lesions on Ornamental Sweet Potato 'Blackie', Tomato 'Maxi Fort', Interspecific Geranium 'Caliente Coral', and Bat-Faced Cipher 'Tiny Mice'. J. Amer. Soc. Hort. Sci. 139: 603–615.

Douglas, G. E. (1907) The Formation of Intumescences on Potato Plants. Botanical Gazette. 43: 233–250.

Lang, S. P. and Tibbitts T. W. (1983) Factors Controlling Intumescence Development on Tomato Plants. Journal of the American Society for Horticultural Science. 108: 93-98.

Kumazaki, A., Kawakami, M., Asano, Y., and Suzuki T. (2010) Effect of Fertilization Method to Suppress Burned Leaf Tip of Tomato. Hort. Res. (Japan) 9 (Suppl. 1): 135 (In Japanese).

Ozawa, C., Tonooka, C., Kiriiwa, Y., and Suzuki K. (2018) Cultivar Difference in Occurrence of Edema in Tomato. Hort. Res. (Japan) 17: 436. (in Japanese).

Marcshner, H. (1995) Mineral Nutrition of Higher Plants, 2nd edn. Academic Press.

Mazumder, M. N. N., Misran, A., Ding, P., Wahab, P. E. M., and Mohamad. A. (2021) Preharvest Foliar Spray of Calcium Chloride on Growth, Yield, Quality, and Shelf Life Extension of Different Lowland Tomato Varieties in Malaysia. Horticulturae. 7, 466. https://doi.org/10.3390/horticulturae7110466

Schabow, J. E. and Palta J. P. (2019) Intumescence Injury in The Leaves of Russet Burbank Potato Plants is Mitigated by Calcium Nutrition. American Journal of Potato Research. 96: 6–12.

Suzuki, K., Ozawa, C., and Kiriiwa Y. (2020) Morphological Study on the Incidence of Intumescence Injury in Tomato Plant Leaves. Hort. J. 89: 567-574.

White, P. J. and Broadley M. R. (2003) Calcium in Plants. Annals of Botany. 92: 487-511.

Ueno, H., Maeda, T., Katsuyama, N., Katou, Y., Matsuo, S., Yano, K., Ando, A., Nagasuga, K., Yamada, M. and. Imanishi S. (2018) Cation Measurements and Gene Expression Analysis Suggest Tomato Leaf Marginal Necrosis is Caused by a Jasmonate Signal Induced by K^+ Starvation in The Tip Region of Leaflets. The Horticulture Journal. 87: 206-213.

Microbial fuel cell on different cultivation systems to reduce N_2O and CH_4 emission in Indonesia

Adhia Azhar Fauzan[1], Ken Hiramatsu[2] and Takeon Onishi[2]

1. **The United Graduate School of Agricultural Science, Gifu University, 1-1 Yanagido, Gifu 501-1193, Japan**
2. **Faculty of Applied Biological Sciences, Gifu University, 1-1 Yanagido, Gifu 501-1193, Japan**

INTRODUCTION

In Rice paddy fields there is a reduction of NO_3 (Nitrate) to form N_2O (Nitrous oxide) and a reduction of CO_2 (Carbon dioxide) to form CH_4 (Methane). N_2O and CH_4 are greenhouse gasses playing a key role in global warming with a global warming potential (GWP) that is 265 and 28 times higher than that of CO_2 per unit mass for 100 years scale (Yang et al., 2019). The availability of oxygen in the soil of rice paddy fields is very important for microbes because oxidants are used as electron acceptors from microbial activity. Anaerobic conditions in rice paddy fields cause low oxygen availability. The availability of oxygen in the soil is influenced by the concentration of soil oxidants such as NO_3, SO_4, Fe_2O_3, MnO_4, and CO_2. The low oxygen content in the soil causes redox to occur. Although not as frequently observed as pH, redox also highly influences chemical and biological processes in soil.

A microbial Fuel Cell (MFC) is a device using metabolic catalysis of microorganisms to generate electric energy by utilizing organic matter in the environment (Logan et al., 2006). The electrons and protons were produced by the substrate that was used by the electricians at the anode. An external circuit and internal texture make the electrons and protons travel through them to the cathode, where eventually oxygen reacts to them, then produces electricity (Zhang et al., 2021). In short, MFC can function as electron acceptors as a result of microbial activity. The presence of MFC as an electron acceptor will prevent microbes from using the oxidants in the soil.

Indonesia is the world's third-largest rice producer and one of the world's biggest rice consumers. Indonesia's climatic conditions allow rice to be cultivated throughout the year. The Rice area in Indonesia in 2010 is 13.2 million ha, representing 24% of the total agricultural area in Indonesia. Rice yield increased slightly from 4.3 t/ha in 1995 to 5 t/ha in 2010. 84% of the total rice field in Indonesia in 2012 were irrigated and flooded(International Rice Research Institute., 2013). The total area and irrigation treatment in rice fields in Indonesia have the potential for large CH_4 and N_2O emissions. Understanding and quantifying the N_2O and CH_4 budget is important for assessing realistic pathways to mitigate climate change. Indonesia has developed a cultivation system to increase rice production. It is called "Jajar Legowo". The idea is to create an open row after several regular rows. For compensating the open row, plant spacing within each of the edge rows is half of the normal plant spacing. Adjusting plant spacing is one of the important agronomic practices for increasing crop yield and reducing plant competition with weeds and plant-to-plant competition for available water and nutrient and light.

The occurrence of an increase in redox in flooded soil with MFC proves that MFC has succeeded in becoming an electron acceptor in anaerobic conditions of rice paddy soil (Ranatunga et al., 2018). The absence of NO_3 and CO_2 as electron acceptors makes these oxidants available and can be utilized by plants. The utilization of NO_3 and CO_2 as elements for plant growth is estimated to suppress N_2O and CH_4 emission production. Furthermore, it is hoped that the emission of N_2O and CH_4 will decrease.

MATERIALS AND METHODS

Two different treatments will be analyzed in this study: without MFC (control) and with MFC. Using the conventional and cultivating systems from Indonesia, "Jajar Legowo". Using 3 m x 2 m per plot. Spacing 25 cm x 25 cm for conventional system and (25 cm x 50 cm) x 12.5 cm for Jajar Legowo system. Carbon graphite-felt melt (S-221; Osaka Gas Chemical Co., Ltd.) will use as an anode with a total surface area of 100 cm2 (length 10 cm x length 10 cm x thickness 1 cm). As a cathode, a graphite rod (C-072591; Nilaco Corporation) with a length of 10 cm and diameter of 0.5 cm upper the water.

The Eh meter (PRN-41; Fujiwara Factory Co., Ltd.) will be use to measure the redox potential. Applying a closed chamber method, gas was sampled once per week. N_2O and CH_4 concentrations will be measured by gas chromatography (GC-2014; Shimadzu CO., Ltd.). Gas samples will be taken at 15-minute intervals between 7 and 8 am.

To determine the mass balance of nitrogen in this study, we will analyze nitrogen in soil and water.

Fig. 1: conventional cultivation systems. Source: https://www.goodnewsfromindonesia.id/2021/05/07/miliki-jutaan-hektare-lahan-inilah-10-provinsi-dengan-lahan-sawah-terluas-di-indonesia

Fig. 2: Jajar Legowo cultivation systems. Source: https://tabloidsinartani.com/detail/indeks/agri-penyuluhan/15688-Kenali-Kembali-Sistem-Jajar-Legowo

REFERENCES

International Rice Research Institute. (2013). *Rice almanac : source book for one of the most economic activities on Earth.*

Logan, B. E., Hamelers, B., Rozendal, R., Schröder, U., Keller, J., Freguia, S., Aelterman, P., Verstraete, W., & Rabaey, K. (2006). Microbial fuel cells: Methodology and technology. In *Environmental Science and Technology* (Vol. 40, Issue 17, pp. 5181–5192). https://doi.org/10.1021/es0605016

Ranatunga, T., Hiramatsu, K., & Onishi, T. (2018). Controlling the process of denitrification in flooded rice soils by using microbial fuel cell applications. *Agricultural Water Management*, *206*(April), 11–19. https://doi.org/10.1016/j.agwat.2018.04.041

Yang, shihong, Xiao, Y., Sun, X., Ding, J., Jiang, Z., & Xu, J. (2019). Biochar improved rice yield and mitigated CH4 and N2O emissions from paddy field under controlled irrigation in the Taihu Lake Region of China. *Atmospheric Environment*, *200*, 69–77. https://doi.org/10.1016/j.atmosenv.2018.12.003

Zhang, K., Wu, X., Wang, W., Chen, J., Chen, J., & Luo, H. (2021). Roles of external circuit and rhizosphere location in CH4 emission control in sequencing batch flow constructed wetland-microbial fuel cell. *Journal of Environmental Chemical Engineering*, *9*(6). https://doi.org/10.1016/j.jece.2021.106583

Sustainable pesticide management: Personalized simulation for Indian soil

Kishalay Chakraborty[1], Atsuhiro Shimada[1] and Akio Ebihara[1]
1. The United Graduate School of Agricultural Science, Gifu University, 1-1 Yanagido, Gifu, 501-1193, Japan

INTRODUCTION

Food security is a major challenge in the 21st Century. Due to the increasing population and decreasing agricultural land share, we will be in scarcity of food in the next few years. To tackle this issue, steps were taken in the last century. Many of them are currently considered detrimental, due to their irreversible impact on human health, the environment, and also soil health leading to a long-term loss in productivity. The unregulated use of pesticides is a major factor among them. There is a lack of awareness about application methods and quantity. The key stakeholders in the agriculture processes, the farmers, are mostly unaware of the effects of pesticides on health, the environment, and soil. The effect of pesticide residues on soil may be predicted by mechanistic methods by modeling the soil conditions in a simulation system. This may be a useful tool for farmer awareness.

Tang F. H. M. et.al. reported a pesticide residue simulator using a Global perspective by simulating soil texture, weather, pesticide application, etc. in BRTSIM software (Tang & Maggi, 2021). La Cecilia reported the simulation of Glyphosate degradation in soil(la Cecilia & Maggi, 2018). Hendrik Rathjens modeled pesticide and Metabolite concentration in soil using the SWAT+ tool (Rathjens et al., 2022). Victoria Kolupaeva modeled the transport of pesticides and water in the soil(Kolupaeva et al., 2022).

India is a country with a large population and very diverse agriculture systems and climatic conditions. The same pesticide protocol does not apply to all soil and climatic conditions. Personalized pesticide protocol is required for individual farms, based on their soil and climatic conditions. A firm-level personalized simulation system for Indian conditions will be developed in this work. Soil/climate properties and the application rate of pesticide species will be the input for developing the model. The system will predict the time required for the pesticide to degrade. This information will help to manage pesticide application sustainably and safely.

The government of India developed a database of soil parameters by lab testing soil samples from individual farmers. (Soil Health Card, n.d.). This individual farmer's data will be used in this study to make the personalized model. The data generated from this research may produce a heatmap of high pesticide concentration areas in India. This data may be helpful for Government and other regulatory agencies in developing pesticide-related policies in those areas. This work will be a small step towards sustainable agriculture.

MATERIALS AND METHODS

Simulation tool – BRTSim — BRTsim is a Computational solver for biochemical reactions and transport of fluids in porous and nonporous media. In this study, BRTSim will be used to model the soil based on soil property and weather data and simulate the degradation and movement of Pesticide compounds in soil with water.

Soil Health Card (SHC) data— The government of India launched this program to test individual farmers' land for nutrient parameters and scientifically prescribe crops relevant to fertilizer requirements. This scheme has tested 5,47,46,153 samples in the laboratory for 12 soil parameters including pH, Organic Carbon, EC, Macro and micronutrients, etc. The data is published in SHC Portal and available for free. The data is downloaded from the portal for the North-East part of India and processed using Python scripts to extract the pH and Organic Carbon concentration which are useful for this study.

Soil Texture and Porosity— Soil texture is the ratio between three types of soil particles Sand, Silt, and Clay. This data is collected in the form of a NetCFD file from the GLDAS Fractions of clay, sand, and silt Database (Rodell et al., 2004) at a spatial resolution of 0.25 degrees. The data is processed with Python script and netCDF4 library.

Time series Rainfall and Temperature data — Time-series Rainfall (Pai et al., 2014) and Temperature (Bhaskar Rao et al., 2009) data are collected from the Indian government weather portal. The daily minimum, maximum and average temperature are available at the spatial resolution of 0.25 and 1.0 degrees respectively. The data is available as binary files which are processed using the 'c' scripts provided along with the data. The binary files are converted to CSV format and then processed using the custom python scripts.

Time series solar radiation data— Solar radiation is the source of energy on earth. The visible ray or shortwave radiation reaches the earth's surface and heats the earth's surface. The heat is also reflected from soil to the atmosphere as long-wave radiation. CRU JRA v2.3 (Kobayashi et al., 2015)database is collected which provided both shortwave and longwave radiation of the earth's surface at 0.5 degrees spatial resolution at an interval of 6 hours. The data is available as a NetCFD file and processed using python and netCFD4 libraries. The unit of both shortwave and longwave radiation are Watt/m^2 or J/s m^2.

Time series potential evapotranspiration data— CRU TS4.06 database (Harris et al., 2020) contains time-series data of potential evapotranspiration as a daily average at monthly intervals. The data is represented as mm/day. This dataset is also available as a NetCFD file and processed using python and netCFD4 libraries.

Pesticide application data — Pesticide application data is collected from the Government of India Ministry of Agriculture and farmers welfare, directorate of plant protection, quarantine & storage Statistical database. The data is available in excel files for 2017-18 to 2021-22 in the form of State-wise consumption of chemical pesticides [C_{cons} in Metric Ton] and Pesticide wise Total consumption in the country. Total agricultural land use is accessed from Area and production statistics Ministry of Agriculture and Farmers welfare's Area Production and Yield Information System. [$A_{Cultivation}$ in Hactere]. State-wise average pesticide application rate [R_{avg}] is calculated from Consumption [C_{cons}] and area [$A_{Cultivation}$] as Equation1. The average pesticide application rate is plotted in Fig. 1.

$$R_{avg} = \frac{Ccons \ x\,1000}{ACultivation \ x10000} \ [\text{in Kg/m}^2] \quad (1)$$

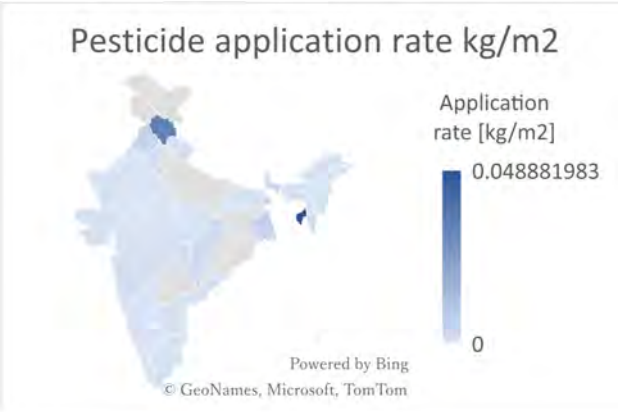

Fig. 1: Average Pesticide application rate 2017-2021

Development of model — The model is developed by following Tang & Maggi (2021) and introducing new input data. The system is divided into 2 atmospheric layers and 4 soil layers F01-F04. The pesticide 'Acephate' is selected randomly to simulate using this system.

RESULTS

Test case 1 — In test case 1 pesticide is applied only at time t=0 at the top soil layer. The model is simulated for 5 years. The gradual movement of pesticide (and gradual decay) from one layer to another can be observed in Fig. 2.

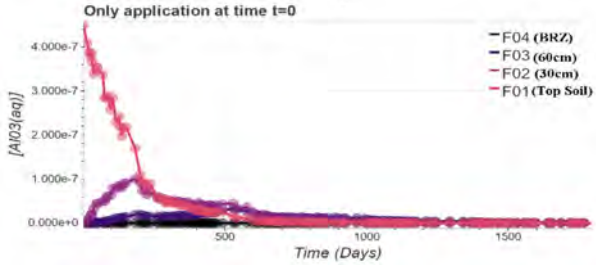

Fig. 2: Test case 1 Result. F01-F04: Soil Layers top to BRZ(Bellow Root Zone) respectively.

Test case 2 — In this case pesticide is applied repeatedly over the entire 5 years simulation time. The result is shown in Fig.3. The exponential decay of concentration is not observed in this case due to continuous pesticide input.

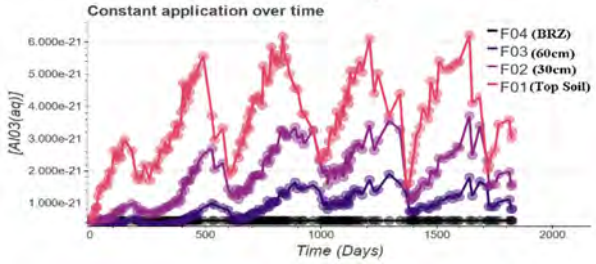

Fig. 3: Test case 2 Result. F01-F04: Soil Layers top to BRZ(Bellow Root Zone) respectively.

Test case 3 — In this case, a total of 84 land samples are simulated by applying respective Average pesticide application, soil texture, pH, and Organic Carbon Content for 3 years duration. The final pesticide concentration for the individual data point is shown in Fig. 4

Fig. 4: Test case 3 Result. Individual data points

DISCUSSION

Using BRTSim software, Chemical residue for the pesticide 'Acephate' in Indian soil conditions for 84 farmers samples were simulated in this work. Although all the parameters are not introduced yet in this system. As a result, in Case 3 the major factor seems to be the pesticide application rate only. Furthermore, data from 47 individual pesticides are available to be simulated. We are preparing the system to introduce all the parameters together and apply time series input pesticide concentration to make the system robust.

ACKNOWLEDGMENTS

We are grateful to Prof. Federico Maggi, The University of Sydney, for advice on the use of the BRTSim software, which is publicly available at https://sites.google.com/site/thebrtsimproject/home.

We acknowledge the support and guidance from Professor Naoto Ogawa from Shizuoka University, Shizuoka, Japan.

REFERENCES

Bhaskar Rao, Srinivas, D., & Ratna, S. B. (2009). Development of a high resolution daily gridded temperature data set (1969 – 2005) for the Indian region. *Atmospheric Science Letters*, *10*(October), 249–254.

Harris, I., Osborn, T. J., Jones, P., & Lister, D. (2020). Version 4 of the CRU TS monthly high-resolution gridded multivariate climate dataset. *Scientific Data*, *7*(1), 1–18.

Kobayashi, S., Ota, Y., Harada, Y., Ebita, A., Moriya, M., Onoda, H., Onogi, K., Kamahori, H., Kobayashi, C., Endo, H., Miyaoka, K., & Kiyotoshi, T. (2015). The JRA-55 reanalysis: General specifications and basic characteristics. *Journal of the Meteorological Society of Japan*, *93*(1), 5–48.

Pai, D. S., Sridhar, L., Rajeevan, M., Sreejith, O. P., Satbhai, N. S., & Mukhopadhyay, B. (2014). Development of a new high spatial resolution (0.25° × 0.25°) long period (1901-2010) daily gridded rainfall data set over India and its comparison with existing data sets over the region. *Mausam*, *65*(1), 1–18.

Rodell, M., Houser, P. R., Jambor, U., Gottschalck, J., Mitchell, K., Meng, C. J., Arsenault, K., Cosgrove, B., Radakovich, J., Bosilovich, M., Entin, J. K., Walker, J. P., Lohmann, D., & Toll, D. (2004). The Global Land Data Assimilation System. *Bulletin of the American Meteorological Society*, *85*(3), 381–394.

Tang, F. H. M., & Maggi, F. (2021). Pesticide mixtures in soil: A global outlook. *Environmental Research Letters*, *16*(4). https://doi.org/10.1088/1748-9326/abe5d6

Rice yield prediction using UAV-based imagery and deep learning

Md Suruj Mia[1,2] and Takashi S. T. Tanaka[2,3]

1. **The United Graduate School of Agricultural Science, Gifu University, 1-1 Yanagido, Gifu 501-1193, Japan**
2. **Faculty of Applied Biological Sciences, Gifu University, 1-1 Yanagido, Gifu 501-1193, Japan**
3. **Artificial Intelligence Advanced Research Center, Gifu University, 1-1 Yanagido, Gifu 501-1193, Japan**

INTRODUCTION

Rice, a cereal crop is the most widely consumed staple food for half of the world's population (Zhou et al., 2022) mostly in Asia and Africa. To fulfill present and future demands, there is an increasing need to enhance yield gains per unit land area while preserving natural resources (Grassini et al., 2013). In agricultural sector timely, non-destructive, inexpensive, and reliable yield forecast at large scale is important and prerequisite for preventing climate risk and ensuring food security, especially with climate change and extreme events (Kang et al., 2009).

To predict yield before harvesting a variety of methods have been presented and used, including ground-based field surveys, farmers' expert knowledge, crop growth models (A.J.W. de Wit, C.A. van Diepen, 2008), remote sensing-based methods (Wang et al., 2010), and crop growth models combined with environmental factors and remote sensing data (Betbeder et al., 2016). The usual statistical approach should not be utilized to analyze data collected on farms as it does not meet the requirements of the experimental design (Zhou et al., 2021).

Since 1970s, satellite data have been extensively employed with varying spatial, temporal, and spectral resolutions for agricultural yield prediction over the glove (Battude et al., 2016). However. clumsy geographical resolution and subpar temporal sampling, make it difficult to use satellite data for yield prediction (Wang et al., 2010). As compared with compared airborne and satellite platforms, Unmanned Aerial Vehicles (UAVs) has significantly promoted for data collecting due to the superior spatial, spectral, and temporal resolution (Maimaitijiang et al., 2020). A reliable technique for monitoring agricultural crops is the extraction of visual indices (VIs) and color indices (CIs) from multispectral and RGB images (Zhou et al., 2022). The physiological and geometric properties of vegetation such as leaf chlorophyll content, leaf area index (LAI), nitrogen concentration, plant height, biomass yield and grain yield can be estimated from canopy spectral information derived from UAV-based multispectral and hyperspectral imagery (Maimaitijiang et al., 2020).To attain precise yield estimation for a variety of crops, many statistical and machine learning (ML) approaches have been developed. Deep Learning (DL) can automatically learn representations from data using a multi-layer architecture, which supports complex nonlinear functions that are learned from the hierarchal outputs of the previous layers. In many fields, DL outperforms conventional feature extraction techniques in the domain of image and semantic recognition, natural language processing and video analysis (Ji et al., 2013). According to Krizhevsky et al. (2012), convolutional neural network (CNN) is the most effective DL technique for image classification and regression tasks. The CNN architectures receive input images with dimensions of width, height, and depth, and extract the features through a sequence of operations including convolution and pooling (Yang et al., 2019).

The objective of this study was to develop rice yield prediction model using CNN and UAV-based high-resolution multispectral images during the heading stage. Thus, we compared the prediction accuracy between traditional linear model based on VI and CNN model. We further explored the feasibility of the CNN model for on-farm experimentation (OFE) with different fertilization treatment plots.

MATERIALS AND METHODS

Rice was grown at different location of Japan from 2017–2021. To evaluate different fertilizer application rates, strip trials were performed at nine fields in different locations of Gifu, Japan from 2020–2021. In OFEs, 8-row rice transplanters with a 2.4-m working width were used to adjust the application rates of basal fertilizer. The nitrogen (N) fertilizer was applied in the OFE fields at a rate of 0, 250, 300, 350, and 400 kg ha^{-1}.

Image data for yield prediction of rice was collected by using two multispectral cameras (Sequoia+, Parrot, Paris, France and Rededge-Altum, MicaSense, Seattle, USA) mounted on a UAV platform at the heading stage. Using structure-from-motion software (Pix4D mapper version 4.4.12, Pix4D, Prilly, Switzerland), the captured multispectral images were processed to generate reflectance imagery. The ground sample distance (GSD) ranged from 0.01 to 0.06 m per pixel. A total of 641 plant samples with georeference were harvested within an approximately of 1-m^2 area. Utilizing those georeferenced yield data and corresponding 1-m^2 images clipped from the reflectance imagery, CNN models for crop yield prediction were developed. The input bands were green, red, and nearinfrared. The total dataset was randomly split into training (59.90%, n = 384), validation (19.97%, n = 128) and test (20.13%, n = 129) datasets. Using AlexNet and CNN architecture the CNN model was built. The patience, epoch, batch size, and learning rate were 15, 100, 32, and 0.001, respectively. The training dataset was augmented by rotating and flipping the resized images. The reflectance maps for prediction were split into 1-m^2 images.

RESULTS AND DISCUSSION

The relationship between observed and predicted yield are shown in Figure 1 (a) and (b) for AlexNet and CNN architecture, respectively. The root mean square error (RMSE) in the predicted rice yield for Alexnet architecture-based Model was 0.691, 0.945 and 0.748 t ha^{-1} for the training, validation, and test datasets, respectively, while the percentage of error (RMSPE) was 13, 18 and 16 for the training, validation, and test datasets, respectively. The RMSE in the predicted rice yield for CNN architecture-based Model was 0.854, 1.054 and 0.943 t ha^{-1} for the training, validation, and test datasets, respectively and the percentage of error (RMSPE) was 15, 20 and 18 for the training, validation, and test datasets, respectively. The R^2 for Alexnet architecture-based Model was 0.691, 0.543, and 0.614 for the training, validation, and test datasets, respectively and for CNN architecture-based Model was 0.598, 0.431, and 0.533 for the training, validation, and test datasets, respectively. Table 1 shows the performance of both architectures. The AlexNet architecture-based CNN model is outperformed regarding R^2 and RMSE. The RMSE and R^2 values of the models specify that the AlexNet architecture-based model can estimate the rice grain yield more accurately than CNN architecture-based model from the multispectral images collected by UAV at heading stage.

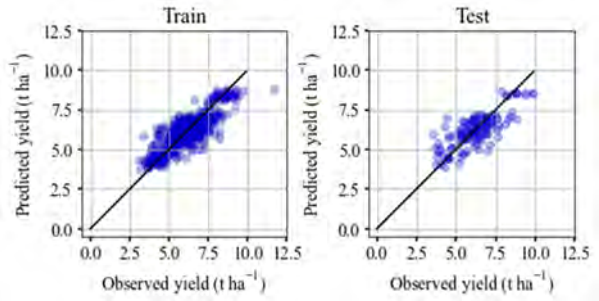

Fig. 1 (a): Relationship between observed and predicted grain yield derived from the Alexnet architecture-based CNN model.

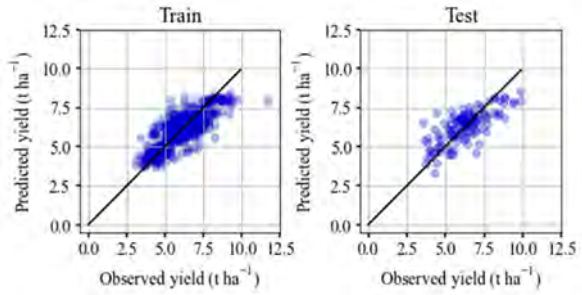

Fig. 1 (b): Relationship between observed and predicted grain yield derived from the CNN architecture-based CNN model.

Table: Results of prediction models based on RGB images

	Alexnet architecture		CNN architecture	
	Train	Test	Train	Test
r^2	**0.691**	0.614	0.598	0.533
RMSE (tha^{-1})	0.748	0.858	0.854	0.943
RMSPE (%)	13	16	15	18

By using the developed models, the yield prediction was done on OFE field. Figure 2 (a) and 2 (b) shows the predicted yield maps of one of the investigated fields with the AlexNet and CNN architecture-based model, respectively. The estimated yield map in both prediction models clearly displayed spatial variability. Both models identified the different fertilizer treatments in the field and low estimation in the boundary side. CNN architecture-based model tended to overestimate to whole field than Alexnet architecture-based model.

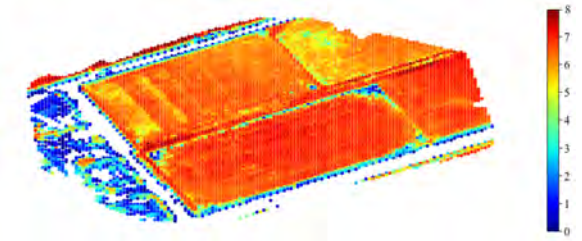

Fig. 2 (a): Spatial variation of yield on OFE-field derived from the Alexnet architecture-based CNN model.

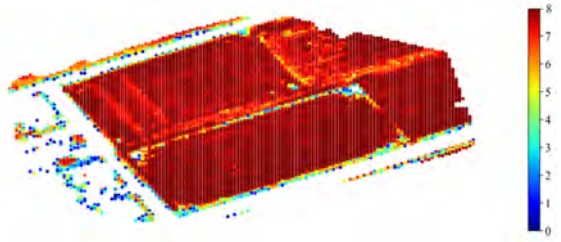

Fig. 2 (b): Spatial variation of yield on OFE-field derived from the CNN architecture-based CNN model.

REFERENCES

A.J.W. de Wit, C.A. van Diepen, Crop growth modelling and crop yield forecasting using satellite-derived meteorological inputs, International Journal of Applied Earth Observation and Geoinformation, Volume 10, Issue 4

Battude, M., Al Bitar, A., Morin, D., Cros, J., Huc, M., Sicre, C.M., Le Dantec, V., & Demarez, V. (2016).

Betbeder, J., Fieuzal, R., & Baup, F. (2016). Assimilation of LAI and Dry Biomass Data From Optical and SAR Images Into an Agro-Meteorological Model to Estimate Soybean Yield. Ieee Journal of Selected Topics in Applied Earth Observations and Remote Sensing, 9, 2540-2553

Collobert, R., Weston, J., 2008. A unified architecture for natural language processing: deep neural networks with multitask learning. Proc. 25th Int. Conf. Mach. Learn. 160–167. https://doi.org/10.1145/1390156.1390177.

Grassini, P., Eskridge, K. M., and Cassman, K. G. (2013). Distinguishing between yield advances and yield plateaus in historical crop production trends. Nat. Commun. 4:2918. doi: 10.1038/ncomms3918

Ji, S., Yang, M., Yu, K., 2013. 3D convolutional neural networks for human action recognition. Pami 35, 221–231. https://doi.org/10.1109/TPAMI.2012.59.

Kang, Y., Khan, S., & Ma, X. (2009). Climate change impacts on crop yield, crop water productivity and food security–A review. Progress in natural Science, 19, 1665-1674

Krizhevsky, A., Sulskever, Ii., Hinton, G.E., 2012. ImageNet classification with deep convolutional neural networks. Adv. Neural Inf. Process. Syst. 60, 84–90. https://doi.org/10.1145/3065386.

Maimaitijiang M., Sagan V., Sidike P., Hartling S., Esposito F., Felix B. Fritschi, Soybean yield prediction from UAV using multimodal data fusion and deep learning, Remote Sensing of Environment, Volume 237, 2020, https://doi.org/10.1016/j.rse.2019.111599.

Qi Yang, Liangsheng Shi, Jinye Han, Yuanyuan Zha, Penghui Zhu, Deep convolutional neural networks for rice grain yield estimation at the ripening stage using UAV-based remotely sensed images, Field Crops Research, Volume 235, 2019, Pages 142-153. https://doi.org/10.1016/j.fcr.2019.02.022

Wang, K., Franklin, S.E., Guo, X., & Cattet, M. (2010). Remote sensing of ecology, biodiversity and conservation: a review from the perspective of remote sensing specialists. Sensors, 10, 9647-9667

Xinbin Zhou, Yusuke Kono, Aung Win, Tsutomu Matsui & Takashi S. T. Tanaka (2021) Predicting within-field variability in grain yield and protein content of winter wheat using UAV-based multispectral imagery and machine learning approaches, Plant Production Science, 24:2, 137-151, DOI: 10.1080/1343943X.2020.1819165

Zhou, J.; Lu, X.; Yang, R.; Chen, H.;Wang, Y.; Zhang, Y.; Huang, J.; Liu, F. Developing Novel Rice Yield Index Using UAV Remote Sensing Imagery Fusion Technology. Drones 2022, 6, 151. https://doi.org/ 10.3390/drones606015

Effects of transglutaminase on pasting properties and retrogradation of rice flour

Dang Thi Kim Lien[1,2] and Takahisha Nishizu[2]

1. **The United Graduate School of Agricultural Science, Gifu University, 1-1 Yanagido, Gifu 501-1193, Japan**
2. **Faculty of Applied Life Sciences, Gifu University, 1-1 Yanagido, Gifu 501-1193, Japan**

INTRODUCTION

Rice is one of the most important food sources in human diet for many reasons. It is the primary consumption of more than half of the world's population. Products prepared from rice flour always remain highly referable due to the digestibility and hypoallergenic properties. However, the critical concern about rice flour prepared products is the deterioration of starch during storage caused by retrogradation.

Most of the studies about retrogradation focused on the effects on starch component, but the effects on proteins which is the second abundance component have not been investigated deeply. From previous studies, it showed that protein fractions and its structure in rice affected the physical characteristics of cooked rice (Furukawa, 2008). Therefore, the modification on protein molecules possibly affects the product properties during.

Transglutaminase (TG) is protein-glutamine c-glutamyl-transferase (EC 2.3.2.13) that catalyzes the cross-linking reaction between glutamine and lysine. It has been successfully applied to alter the technological and functional properties of food matrices containing proteins, resulting in improvements of elasticity, water holding capacity and other functional properties. The action of TG on rice protein can possibly affect properties of rice flour during processing. Renzetti et al. (2007) has also proved that TG modified main protein fractions in rice flour and resulted in the formation of high molecular polymers which improved water holding capacity in rice batter. In addition, the patent on application of TG in rice cooking (Kitagawa, 2002) shown its effectiveness on maintaining the texture of cooked rice in excessive amount of water and consequence to an reduce in retrogradation process. However, there is no report about the effects of TG on pasting properties and retrogradation tendency of rice flour which are significant factors in predicting and controlling the quality of rice products.

The aim of this paper is to investigate the effects of TG on starch pasting properties and starch retrogradation, and thus get a better insight on the application of TG in rice products.

MATERIALS AND METHODS

Materials—Rice flour contained 6% of protein (Kumamoto Co., Japan) was purchased from local supermarket. Activa TG-K contained 1% of microbial Transglutaminase was provide by Ajinomoto Co. (Tokyo, Japan).

Transglutaminase purification—Activa TG-K preparation contained 1% of TG, 75% Calcium lactate, 24% dextrin and others. These background substances may interfere the results, therefore, purification was required. Two grams of Activa TG-K was dissolved in 10 ml of 0.1 M Tris/HCl buffer (pH 7.5). The mixture was centrifuged at 15,000 rpm at 4°C for 30 mins. The supernatant was collected and dialyzed at 4°C for 6hrs in Tris/HCl buffer (pH 7.5) solution. The solution was changed every 2hrs. The obtained solution was used as a 0.2% TG solution for enzymatic reaction.

Pasting properties of rice flour—Three grams of rice flour and 25 g of water were put into RVA canisters. TG was added to this mixture at the concentration of 0.5 and 1 % w/w of protein. The mixture was incubated for 30 mins at 55°C in a water bath. The pasting properties of samples were determined with a Rapid Visco Analyser (RVA) Super 3 (Newport Scientific Inc., Australia). The temperature profile involved an initial 10 s high-speed (960 rotations min^{-1}) stir that dispersed the sample prior to the beginning of the measuring phase at 160 rotations min^{-1}. Temperature was held at 50 °C for 1 min and then raised to 93 °C in 4 mins, held for 7 min, cooled to 50 °C in 4 mins, and held for 3 mins.

XRD samples preparation and measurement —The samples (1:2 dry matter of rice flour-to-water ratio) with TG 0.5 and 1 % w/w of protein were incubated for 30 mins at 55°C in a water bath, then gelatinized by steaming in an autoclave at 104°C for 30 mins. Subsequently, the gelatinized samples were stored at 4°C for 5 and 7 days to allow them to retrograde. Afterward, these samples were lyophilized. The freeze-dried samples were ground, and then the powder samples were passed through a 100-µm sieve before XRD.

Freeze-dried rice gel powder was added 0.8% Zinc Oxide for standardization and 0.7 times of water (w/w of rice flour) right before measurement. The XRD was conducted using a SmartLab X-ray diffractometer (Rigaku Co., Japan) equipped with a copper tube operating at 45 kV and 200 mA. Measurements were collected at room temperature with a scanning rate of 2°/min and a diffraction angle range of 10–37° (2-Theta° range), where theta is the angle of incidence of the X-ray beam on the sample. The degree of crystallization was analyzed using Origin 2022 software (OriginLab Co., USA).

Statistical analysis— Statistical analysis was performed with SPSS 26.0 software (IBM, USA) on all tests using a one-way ANOVA and Tukey's post hoc test to detect significant differences.

RESULTS and DISCUSSION

Pasting properties—The pasting behaviors of control and TG treated samples were showed in table 1. The addition of TG significantly increased peak, breakdown and final viscosity. The higher peak viscosity with TG treatments was also aligned with the result of Palabiyik et al. (2016) who used TG and other enzymes to modified the pasting properties of gluten-free flour. It was possible that the modification of protein structure and strengthening the gel network via cross-links by TG activity has affected the starch swelling and increased the initial viscosity. The significant higher breakdown value with increasing TG concentration may refer to the surface modification of proteins. Ribotta & Rosell (2010) also reported that incorporation of TG treated-protein significantly increased peak and breakdown viscosity of starch gel. The increase in viscosity during the cooling period (setback) indicates the tendency of the reassociation of amylose present in the hot paste. The significantly decreased in setback by TG treatment indicated a lower tendency of the starch granules to retrograde (Sandhu et

al. 2007). However, some papers have reported an insignificant change in pasting properties when TG was applied in rice flour and whey protein blend (Marco and Rosell, 2008). This could be explained by the different action of TG with different type of protein.

Table 1. Effects of TG treatment on pasting parameter of rice flour.

Samples	Peak Vis (mPa.s)	Breakdown (mPa.s)	Final Vis (mPa.s)	Setback (mPa.s)
Control	2515.33 a	1202.67a	2602.00a	1289.33 b
TG 0.5	2743.67 b	1285.67b	2700.33b	1242.33 a
TG 1	2812.33 b	1400.00c	2649.00a b	1236.67 a

Means of triplicate. Values within a column that have different letters indicate a significant difference (P = 0.05)
TG 0.5: Sample treated with 0.5 % of TG
TG 1: Sample treated with 1 % of TG

Retrogradation of storage rice gel—Data from XRD showed that the retrogradation degree increased with the increase of storage day. This could be explained by the continuous cross-linking and recrystallization of starch molecules to form an ordered structure during the retrogradation. Compared with the rice gel without TG, rice gel with added TG was lower in retrogradation degree after 5 days storage. However, there was insignificant difference between samples after 7 days storages. Renzetti et al. (2007) proposed that a strengthened protein network consequent to protein cross-linking has improved ability to trap water in rice bread and increased in water holding capacity of rice batter, so a possible explanation for this paper results might be the enhance in water holding capacity due to TG action inhibited the retrogradation of rice gel.

In conclusion, the TG treatment had significant effects on pasting properties of rice flour, but it shown slight effect on retarding the retrogradation. It is possible that the concentration of TG has not reached optimum amount to alter the retrogradation behavior of rice gel during storage. Also, further studies need to be conducted to understand the mechanism of TG action on rice flour properties.

REFERENCES

Furukawa, S. (2008). Rice Proteins Bring Good Relationship between Eating Quality of Cooked Rice and Brewing Suitability of Sake. Journal of The Brewing Society of Japan, 103 (3), 145-149.

Kitagawa, T., Kawasaki, M., Hiki, Y., & Nemoto, K. (2002). Production method of highly hydrous rice (Japan. Patent No.JP331008B2).

Marcoa, C., & Rosell, C. M. (2008). Effect of different protein isolates and transglutaminase on rice flour properties. Journal of Food Engineering, 84(1), 132-139.

Palabiyik, I., Yildiz, O., Toker, O. S., Cavus, M., Ceylan, M. M., & Yurt, B. (2016). Investigating the addition of enzymes in gluten-free flours–The effect on pasting and textural properties. LWT-Food Science and Technology, 69, 633-641.

Renzetti, S., Dal Bello, F., & Arendt, E. K. (2008). Microstructure, fundamental rheology and baking characteristics of batters and breads from different gluten-free flours treated with a microbial transglutaminase. Journal of Cereal Science, 48(1), 33-45.

Ribotta, P. D., & Rosell, C. M. (2010). Effects of enzymatic modification of soybean protein on the pasting and rheological profile of starch‐protein systems. Starch‐Stärke, 62(7), 373-383.

Sandhu, K. S., Singh, N., & Malhi, N. S. (2007). Some properties of corn grains and their flours I: Physicochemical, functional and chapati-making properties of flours. Food Chemistry, 101(3), 938-946.

Dissecting the role of N and S in Arabidopsis root architecture under Al stress through physio-genetics approach

Md. Abir Ul Islam[1,2] and Hiroyuki Koyama[2]

1. **The United Graduate School of Agricultural Science, Gifu University, Gifu 501-1193, Japan**
2. **Faculty of Applied Biological Sciences, Gifu University, Gifu 501-1193, Japan**

INTRODUCTION

A significant barrier to crop development, soil acidity (having a pH of less than 5.0), has gradually increased due to natural and/or man-made activities (Von Uexkull and Mutert 1995). This detriment increases the solubilization of Aluminum (Al) into trivalent form (Al^{3+}) represents a major detrimental aspect of economic yield loss of major crops (Kinraide and Parker, 1990; Yokota and Ojima 1995). This Al^{3+} triggered biosynthesis of ethylene and reactive oxygen species (ROS), programmed cell death (PCD) and resulted in inhibition of root growth and development (Reviewed at Alarcon-Poblete et al. 2018). This root inhibition limits the foraging of macro- and micro-mineral nutrients from the soil solution. Recently, detrimental effects of Al have been mitigated with mineral supplements like nitrogen (N) (Liu et al. 2014). Although one of the Al species that contains sulfur, $AlSO_4^-$, is not poisonous to plants, the key macronutrient sulfur (S) has not yet been studied for its potential ameliorative effects under Al stress circumstances (Kinraide 1995). S containing fertilizer Gypsum is commonly used for the abiotic stress tolerance in plants (Carvalho and Van Raijo, 1997; Mora et al., 1999). S containing amino acids like cysteine and methionine help plants to overcome abiotic stress like heavy metals, salinity, etc. (Huang et al. 2021). But the mechanism of S behind the stress alleviation is poorly understood. Therefore, we are trying to find out the molecular mechanism of the S and N during Al^{3+} toxicity. Recently, our laboratory has found some Arabidopsis accessions and mutants (S and N transporter mutant) differential root system architecture (RSA) amid Al stress (Fig. 1). Moreover, some accessions showed sulfate sensitivity and overproduction of lateral roots. From that point of view, we want to examine the combined effect of N and S effect on Al^{3+} toxicity. We will treat plants with short and long-term Al toxicity along with treatments to find out the N and S assimilatory mechanism in tolerance.

Finally, we will try to find out our treatment's effect on the root architecture and also investigate the S-assimilatory pathway dependency on the N-assimilation pathway during amino acid production under Al toxicity. At the end of the study, we hope to find out

I. Responsible S assimilatory genes on Al stress.
II. Complementary expression of N and S assimilation effect genes and enzymes under Al stress.

MATERIALS AND METHODS

Plant materials and growth conditions—Arabidopsis (*Arabidopsis thaliana*) accessions Col-0 (Wild type), STOP1 mutant, ALS3-KO and Ler-1 were used in the first experiment for Al concentrations optimization. For optimizing the concentrations first, we selected 5.0 and then we selected 4.5 as our final pH. Optimization of pH along with or without Al was done by using Msogoya et al. 2008 protocol by using Murashige and Skoog (MS) commercial salt (Table 1 and 2). The concentrations of the Al were 0 µM, 100 µM, 200 µM, 250 µM and 300 µM. Furthermore, we manually prepared the MS media stock solution and selected the strength as ½ MS, 1% agar, 1% sucrose and 1X Gamboge (Sigma-Aldrich) solution for seedling better growth and development. The agar plate media along with the accessions and mutant seeds put vertically in growth chamber. The growth chamber environment was set by following Kobayashi et al. 2007 protocol. After 10 days of growing, we selected 5 plants from each accession and put them in water agar plates and took picture with a digital camera (Canon EOS KissX5) with a fixed focal length and magnification. Then we used EZRhizo software to find out adverse effect of Al in plants.

RESULTS

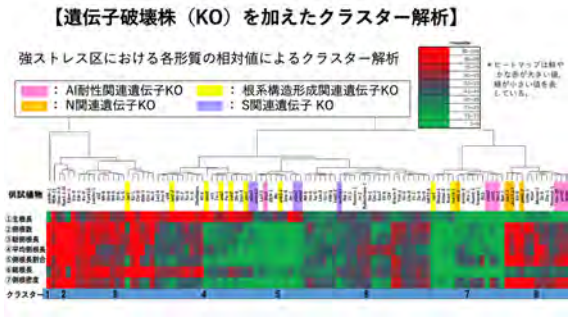

Fig. 1: Clustering Arabidopsis accessions and knock out line in strong Al stress.

Table 1: Optimized of pH in ½ MS media for Al stress.

Initial pH	After Auto clave	50 µM Al	100 µM Al	200 µM Al	250 µM Al	300 µM Al
5.5	5.07	Control				
6	5.48	Control				
6.5	6.035	5.2				
7	6.494		5.072			
7.7	6.907			4.943		
8.0	7.150				5.145	4.568

Table 2: Optimized pH in ¼ MS media for Al stress.

Initial pH	After Auto clave	75 µM Al	100 µM Al
5.4	5.021		
7.0	6.450	4.945	
7.4	6.902		4.904

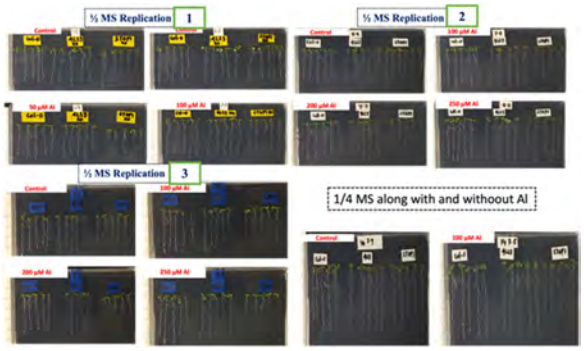

Fig. 2: Observation of Al stress in root system architecture in MS media.

DISCUSSION

Aluminum stress could not observe in the MS agar plate media because of Phosphate (Pi) present in the commercial MS salt (Fig. 2). Pi precipitation occurs in case of high pH when we tried to optimized Al concentration to pH 5.0 that resembled with the finding with da Silva Cerozi & Fitzsimmons (2016). As a result, we remove the phosphate concentration from the MS salt. After getting the Al stress in solid media we will try to see the treatment effects on

ACKNOWLEDGEMENT

We acknowledge the Ministry of Education, Culture, Sports, Science and Technology, Japan.

REFERENCES

Alarcón-Poblete, E., Inostroza-Blancheteau, C., Alberdi, M., Rengel, Z., & Reyes-Díaz, M. (2018). Molecular regulation of aluminum resistance and sulfur nutrition during root growth. Planta, 247(1), 27-39.

Carvalho, M. C. S., & Van Raij, B. (1997). Calcium sulphate, phosphogypsum and calcium carbonate in the amelioration of acid subsoils for root growth. Plant and Soil, 192(1), 37-48.

da Silva Cerozi, B., & Fitzsimmons, K. (2016). The effect of pH on phosphorus availability and speciation in an aquaponics nutrient solution. Bioresource technology, 219, 778-781.

Kinraide, T. B. (1991). Identity of the rhizotoxic aluminium species. In Plant-soil interactions at low pH (pp. 717-728). Springer, Dordrecht.

Kinraide, T. B., & Parker, D. R. (1990). Apparent phytotoxicity of mononuclear hydroxy-aluminum to four dicotyledonous species. Physiologia Plantarum, 79(2), 283-288.

Kobayashi, Y., Hoekenga, O. A., Itoh, H., Nakashima, M., Saito, S., Shaff, J. E., ... & Koyama, H. (2007). Characterization of AtALMT1 expression in aluminum-inducible malate release and its role for rhizotoxic stress tolerance in Arabidopsis. Plant Physiology, 145(3), 843-852.

Liu, B., Luo, C., Li, X., Gray, L., Zhang, F., Liu, M., ... & Lei, B. (2014). Research on the threshold of aluminum toxicity and the alleviation effects of exogenous calcium, phosphorus, and nitrogen on the growth of Chinese fir seedlings under aluminum stress. Communications in soil science and plant analysis, 45(1), 126-139.

Mora, M. L., Schnettler, B., & Demanet, R. (1999). Effect of liming and gypsum on soil chemistry, yield, and mineral composition of ryegrass grown in an acidic Andisol. Communications in soil science and plant analysis, 30(9-10), 1251-1266.

Shen, C., Fu, H. L., Liao, Q., Huang, B., Fan, X., Liu, X. Y., ... & Huang, Y. Y. (2021). Transcriptome analysis and physiological indicators reveal the role of sulfur in cadmium accumulation and transportation in water spinach (*Ipomoea aquatica* Forsk.). Ecotoxicology and Environmental Safety, 225, 112787.

Von Uexküll, H. R., & Mutert, E. (1995). Global extent, development and economic impact of acid soils. Plant and soil, 171(1), 1-15.

Yokota, S., & Ojima, K. (1995). Physiological response of root tip of alfalfa to low pH and aluminium stress in water culture. In Plant-Soil Interactions at Low pH: Principles and Management (pp. 329-331). Springer, Dordrecht.

Effect of exogenous gibberellin on regreening in Valencia orange fruit

Nichapat Keawmanee[1,2], Gang Ma[2,3], Lancui Zhang[2], Masaki Yahata[2,3] and Masaya Kato[2,3*]

1. **The United Graduate School of Agricultural Science, Gifu University, 1-1 Yanagido, Gifu-shi, Gifu 501-1193, Japan**
2. **Department of Bioresource Sciences, Faculty of Agriculture, Shizuoka University, 836 Ohya, Suruga, Shizuoka 422-8529, Japan**
3. **Graduate School of Integrated Science and Technology, Shizuoka University, 836 Ohya, Suruga, Shizuoka 422-8529, Japan**

INTRODUCTION

Regreening occurs in some citrus cultivars, such as Valencia orange. The color of the fruit will reverse from orange (chromoplasts) to green (chloroplasts), when the fruit is left on the tree till the spring or summer season. This process was related to plant pigments such as carotenoids and chlorophylls accumulation in the flavedos. In previous studies, several researchers demonstrated that natural light (Sak et al., 1988), blue LED light (Ma et al., 2021), nitrogen sources (Farag et al., 2014), and gibberellin (Rasmussen, 1973; Coggins and Lewis, 1962) induced the regreening in citrus fruit. Gibberellins, one of the plant hormones, not only delayed the degreening but also induced the regreening in the flavedos of citrus fruits (Rasmussen, 1973). However, the effects of gibberellic acid (GA) treatment on gene expression associated with the pigment accumulation during the regreening remained unknown. Thus, this study aimed to investigate the effects of GA on the accumulation of chlorophyll and carotenoid metabolites and on related gene expression during the regreening in Valencia oranges.

MATERIALS AND METHODS

Fruits of 'Valencia orange' (*Citrus sinensis* Osbeck) from Fujieda farm of Shizuoka University were used as plant materials. The fruit on the tree were separated into two groups, the control (non-treated), and GA-treated group by plastic sheets. 500 μM GA solution was used for spraying the fruit on the tree every 2 weeks for 3 times from April. The fruits in each treatment were harvested at 0, 4, and 6 weeks. After harvest, the flavedo in the top part (the part from the stem end to the middle of the fruit) was sampled, immediately frozen in liquid nitrogen, and kept at -80 °C until use. Chlorophyll was extracted from flavedos using *N*,*N*-dimethylformamide and calculated according to Moran's method (1982). The contents of major carotenoids, all-*trans*-violaxanthin (T-vio), 9-*cis*-violaxanthin (C-vio), lutein (Lut), β-cryptoxanthin (β-Cry), and β-carotene (β-Car), were extracted from the flavedos following Kato's method and measured by HPLC (Kato et al., 2004). Regarding gene expression, the total RNA was extracted by using phenol-chloroform according to Kato's method (Kato et al., 2004). The gene expression analysis was carried out by real-time PCR using TaqMan probes and the set of primers for carotenoid biosynthetic genes (*CitPSY*, *CitPDS*, *CitZ-ISO*, *CitZDS*, *CitCRTISO*, *CitLCYb1*, *CitLCYb2*, *CitLCYe*, *CitHYb*, *CitHYe*, and *CitZEP*), chlorophyll biosynthetic genes (*CitGGDR*, *CitCHLH*, *CitCHLM*, *CitCHL27*, *CitPORA*, *CitCS*, and *CitCAO*), and chlorophyll degradation genes (*CitCLH1*, *CitCLH2*, *CitSGR*, *CitPPH*, *CitPAO*, and *CitRCCR*).

RESULTS

The regreening of citrus fruit was observed in both treatments during the experiment period, especially in GA treatment. Evidently, the color of the flavedo changed from dark orange to pale orange and then turned green. It was related to the increase of chlorophylls contents (Fig. 1A) and decrease of carotenoids contents (Fig. 1B). In GA treatment, the result showed that the contents of chlorophyll *a*, *b*, and total chlorophyll were significantly higher than the control at 6th weeks. In contrast, the contents of total carotenoid, T-vio, C-vio, β-Cry, and β-Car were significantly low levels in the GA treatment compared with the control at the 4th week.

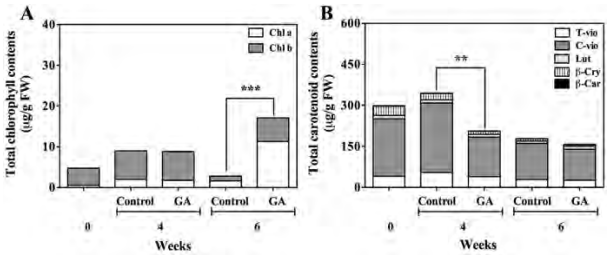

Fig. 1: The contents of chlorophylls (A) and carotenoids (B) of Valencia orange flavedos treated with or without GA at 6th week.

Regarding to the expression of carotenoid and chlorophyll metabolism genes, the expression of eleven carotenoid biosynthetic genes, seven chlorophyll biosynthetic genes, and six chlorophyll degradation genes were investigated. In the present study, the result showed that the up-regulation of chlorophyll biosynthetic genes and down-regulation of chlorophyll degradation and carotenoid biosynthetic genes were observed in both treatments during regreening. In GA treatment, the expression of carotenoid biosynthetic genes (*CitPSY*, *CitPDS*, *CitZDS*, *CitLCYb1*, *CitLCYb2*, and *CitHYb*) were significantly lower, whereas the expression of *CitLCYe* and *CitHYe* were significantly higher than the control treatment at the 6th week (Fig. 2). The expression of genes involved in chlorophyll biosynthesis (*CitGGDR*, *CitCHL27*, *CitPORA*, and *CitCAO*) was significantly up-regulated (Fig. 3A), while the expression of chlorophyll degradation genes (*CitCLH1*, *CitPPH*, and *CitRCCR*) was significantly down-regulated by the GA treatment compared with the control at the 6th week (Fig. 3B).

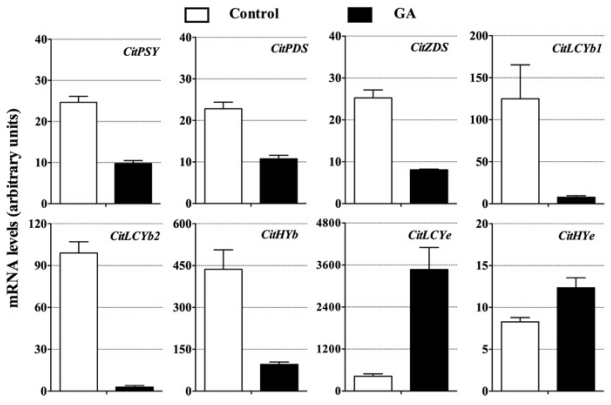

Fig. 2: The expression of genes involved in carotenoid biosynthesis of Valencia orange flavedos treated with or without GA at 6th week.

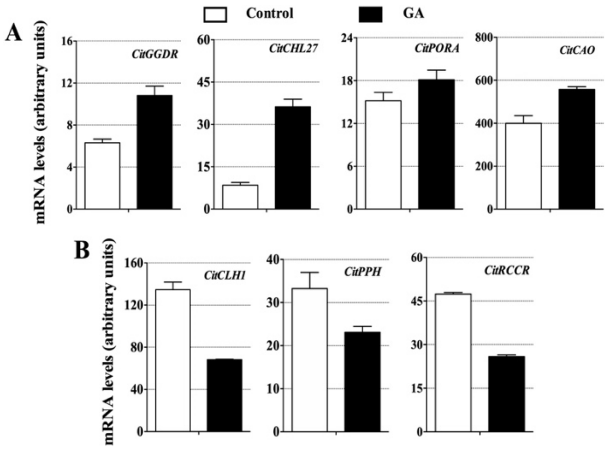

Fig. 3: The expression of genes involved in chlorophyll biosynthesis (A) and chlorophyll degradation (B) of Valencia orange flavedos treated with or without GA at 6th week.

DISCUSSION

In general, the flavedo of citrus fruit accumulated high levels of chlorophyll and β,ε-carotenoids (α-carotene and lutein) in immature fruit. In the mature fruit, the flavedo of citrus fruit turns from green to orange in winter season. The contents of chlorophyll and β,ε-carotenoids decreased, and the accumulation of β,β-carotenoids (β-cryptoxanthin, zeaxanthin, all-*trans*-violaxanthin and 9-*cis*-violaxanthin) was observed (Kato et al., 2004; Ma et al., 2016; Rodrigo et al., 2013). In Valencia orange, the ripened fruit can reverse from orange to green, when the fruit is left on the tree till the spring or summer season (Caprio, 1956). In the present study, the results showed GA treatment induced the accumulation of chlorophylls, whereas reduced the content of carotenoids. The changes in chlorophylls and carotenoid contents were closely related to the expression levels of genes involved in chlorophyll and carotenoid metabolism. The synthesis of chlorophyll and carotenoid shared a common precursor, namely geranylgeranyl diphosphate (GGPP). GGPP was converted into chlorophyll catalyzed by the geranylgeranyl reductase (GGDR) and the tetrapyrrole biosynthetic genes. In the meanwhile, the condensation of two molecules of GGPP forms phytoene by the action of phytoene synthase (PSY), which was the first key step in carotenoid biosynthesis (Alós et al., 2006; Ma et al., 2021). During ripening fruit, the decrease in the gene expression of the *GGDR* was observed, resulting in a decrease in chlorophyll accumulation. In previous studies, exogenous GA was commonly used to delay senescence and loss of chlorophyll in various citrus fruits during pre-harvest or post-harvest (Porat et al., 2001; Alós et al., 2006). In citrus fruit, GA treatment delayed degreening by up-regulation of the transcription of magnesium chelatase (Fujii et al., 2008) and repressed the chlorophyll degradation gene by down-regulation of the gene encoding chlorophyll-degrading pheophorbide a oxygenase (PAO) (Alós et al., 2006). In addition, GA treatments suppressed almost all carotenoid biosynthesis genes, especially the expression of *CitPSY*, *CitHYb*, and carotenoid cleavage dioxygenases in flavedo of citrus fruits (Fujii et al., 2008; Ma et al., 2021).

In conclusion, the results presented in this study suggested that GA treatment induced the regreening in Valencia orange by up-regulation of chlorophyll biosynthesis genes and down-regulation of chlorophyll degradation genes led to the increase of chlorophyll content, and the down-regulation of carotenoid biosynthesis genes led to the decrease of carotenoid contents in the flavedo. These observations indicated that GA acted as a crucial regulator in the regreening process of citrus fruits.

ACKNOWLEDGMENTS

This work was supported by KAKENHI Grant Numbers JP20H02976 (to M.K.) and JP19K06015 (to L.Z.) from Japan Society for the Promotion of Science (JSPS).

REFERENCES

Alós, E., Cercós, M., Rodrigo, M.J., Zacarías, L., and Talón, M. (2006) Regulation of color break in Citrus fruits. Changes in pigment profiling and gene expression induced by gibberellins and nitrate, two ripening retardants. Journal of Agricultural and Food Chemistry 54: 4888-4895.

Caprio, J.M. (1956) An analysis of the relation between re-greening of Valencia oranges and mean monthly temperatures in Southern California. Proceedings of the American Society for Horticultural Science 61: 222-35.

Coggins, C.W. and Lewis, L.M. (1962) Regreening of Valencia orange as influenced by potassium gibberellate. Plant Physiology 37: 625-627.

Farag, K.M., Essa, A.A., Nagy, N.M.N., Haikal, A.M., Attia, S.M. (2014) Influencing of some factors on regreening of "Valencia" orange fruits. Advances in Plants & Agriculture Research 1: 135-140.

Fujii, H., Shimada, T., Sugiyama, A., Endo, T., Nishikawa, F., Nakano, M., Ikoma, Y., Shimizu, T., Omura, M. (2008) Profiling gibberellin (GA3)-responsive genes in mature Mandarin fruit using a citrus 22K oligoarray. Scientia Horticulturae 116 (3): 291-298.

Kato, M., Ikoma, Y., Matsumoto, H., Sugiura, M., Hyodo, H., and Yano, M. (2004) Accumulation of carotenoids and expression of carotenoid biosynthetic genes during maturation in citrus fruit. Plant Physiology 134: 824-837.

Ma, G., Zhang, L.C., Yungyuen, W., Tsukamoto, I., Iijima, N., Oikawa, M., Yamawaki, K., Yahata, M., and Kato, M. (2016) Expression and functional analysis of citrus carotene hydroxylases: Unraveling the xanthophyll biosynthesis in citrus fruits. BMC Plant Biology 16: 148.

Ma, G., Zhang, L.C., Kitaya, Y., Seoka, M., Kudaka, R., Yahata, M., Yamawaki, K., Shimada, T., Fujii, H., Endo, T., and Kato, M. (2021) Blue LED light induces regreening in the flavedo of Valencia orange in vitro. Food Chemistry 335: 127621.

Moran, R. (1982) Formulae for determination of chlorophyllous pigments extracted with *N*,*N*-dimethylformamide. Plant Physiology 69: 1376-1381.

Porat, R., Feng, X., Huberman, M., Galili, D., Goren, R., Goldschmidt, E.E. (2001) Gibberellic acid slows postharvest degreening of Oroblanco citrus fruits. Hortscience 36, 937-940.

Rasmussen, G.K. (1973) The effect of growth regulators on degreening and regreening of Citrus fruit. Acta Horticulturae 34: 473-479.

Rodrigo, M.J., Alquézar, B., Alós, E., Lado, J., and Zacarías, L. (2013) Biochemical bases and molecular regulation of pigmentation in the peel of Citrus fruit. Scientia Horticulturae 163: 46-62.

Saks, Y., Waks, Y., Weiss, B., Franck, A., Chalutz, E. (1988) Light induced postharvest regreening of pummelo fruit. Annals of Applied Biology 113: 375-381.

Evaluation of physical and antioxidant properties of chitosan-based films combing with curcumin nanoemulsion

Fakfan Luangapai [1], Methavee Peanparkdee[2] and Satoshi Iwamoto[1,3]

1. **Division of Science of Biological Resources, The United Graduate School of Agricultural Science, Gifu University**
2. **Department of Food Science and Technology, Faculty of Agro-Industry, Kasetsart University, Bangkok 10900, Thailand.**
3. **Department of Applied Life Science, Faculty of Applied Biological Science, Gifu University, 1-1 Yanagido, Gifu 501-1193, Japan.**

INTRODUCTION

The critical environmental concerned because non-biodegradable plastic wastes affected disposal issues. Biopolymer materials can solve the waste disposal problems because the biopolymer can break down cleanly, in a defined time period. The sea-food processing industry produces a lot of animal wastes like skins and shells of organisms. Conversely, the wastes are excellent sources of chitin. Chitosan, a deacetylated derivative of chitin, considered wide range of applications owing to its biocompatibility, biodegradability, and antimicrobial properties. Nevertheless, chitosan-based films (CH) demonstrate undesirable properties, such as low mechanical strength and high permeability of water vapor transmission, which limit their functions. To overcome the shortcomings and achieve additional functionalities, the studies attempted to incorporate hydrophobic lipid compounds in CH films (Peanparkdee et al., 2016). Curcumin (Cur) has a wide range of beneficial properties, including antioxidant, and antimicrobial properties. However, the utilization of curcumin is restricted due to poor solubility and rapid hydrolysis. Herein, the study focused on the nanoemulsion (NE) technique to overcome dissolubility, stability, and bioactivity of various oil-soluble compounds owing to their small droplet size and high kinetic stability. As effective points of Cur and NE technique, they had high potential to be incorporated with CH-based films in order to improve the films' properties.

This work aimed to ameliorate CH films by incorporating CurNE and determine the alteration of the modified film through its physico-chemical properties, including the water vapor permeability (WVP), mechanical properties, glass transition temperature (T_g), and antioxidant activities.

MATERIALS AND METHODS

Chitosan films preparation

CH powder (2 g) was dissolved in a 1% acetic acid solution. Glycerol was added to the film-forming solution containing 30% w/w CH powder. The solution was heated in a water bath shaking incubator for 4–6 h at 50°C and 120 oscillation/min. The sample solutions were ultrasonicated for 15 min. The modified CH films were prepared via four approaches. First, CH in the film-forming solution as the control sample. Second, CH–NE was the film-forming solution blended with CurNEs. The CH and CH–NE film solutions were separately homogenized and cast on a metal plate. CH–CNE and CH–CO were prepared by modifying the surface with CurNE and curcumin oil (CO). The modified films were conditioned in a chamber for 48 h at 50% relative humidity (RH).

#

Preparation and characterization of curcumin nanoemulsion

Curcumin powder (70 mg) was dispersed in 10 mL of MCT oil to form the oil phase. Tween 80 and distilled water were mixed at 1:8 to form the aqueous phase. Appropriate proportions of the oil and aqueous phases and ultrasonication times as shown in Table 1. Under the various conditions, the size distributions and zeta potentials of the oil droplets were measured on a Zetasizer Nano ZS at 25 °C.

Table 1 formulation of curcumin nanoemulsion.

Sample	Oil: Aqueous phase	Ultrasonic time (minute)
CurNE1	1:4	15
CurNE2	1:4	30
CurNE3	1:4	90
CurNE4	1:4	120
CurNE5	1:6	15
CurNE6	1:8	15
CurNE7	1:9	15

Determination of the WVP of CH-based films

The water vapour transmission rate (WVTR) was evaluated, following the test method of ASTM (2007). The film samples were coated over cups (diameter 5 cm) containing silica gel. The film-covered cups were placed in a chamber that was set to 25 °C and 75% RH. WVTRs ($gm^{-2}d^{-1}$) of the films were determined from the slope of the regression analysis of the moisture weight gain (Δw) obtained through a film area (A) during a definite period (Δt) upon attaining the steady-state (Eq. (1)). The WVTRs of the films were subsequently calculate WVP via Eq. (2). At least five replications of each modified film were tested ($gmmm^{-2}d^{-1}kPa^{-1}$), x is the film thickness (mm), and Δp is the difference between the partial water vapour pressures of the inner (p_1) and outer (p_2) surfaces of the film in the chamber (kPa).

$$\mathrm{WVTR} = \frac{\Delta w}{A\Delta t} \quad \text{Eq. (1)}$$

$$\mathrm{WVP} = \mathrm{WVTR}\ \frac{x}{\Delta p} \quad \text{Eq. (2)}$$

Determination of the mechanical properties of CH-based films

The mechanical properties, tensile strength (TS), and elongation at break (%E) were measured by a universal testing instrument. Three samples (30×50 mm) were tested. The film samples were clamped and deformed under a tensile load at a crosshead speed of 1 mm/min and a gauge length of 30 mm until the samples were broken. TS was calculated by dividing the maximum load (F_{max}) by the initial cross-sectional area (Φ) of the film sample (Pa) (Eq. (3)). Further, %E was calculated as the ratio of the extension of the film (Δl) at the point of sample rupture to the initial length (l_0) of the sample (Eq. (4)).

$$TS = \frac{F_{max}}{\Phi} \quad \text{Eq. (3)}$$

$$\%E = \frac{\Delta l}{l_o} \times 100 \quad \text{Eq. (4)}$$

Determination of the antioxidant activities of CH-based films

The sample (1 mL) was added to the ABTS working solution (4 mL). The mixture was incubated in the dark for 30 min. The ABTS radical scavenging activity (RSA) was calculated employing Eq. (5) and expressed as mmol Trolox/g weight of the dried film:

$$\mathrm{RSA}(\%) = (A_{control} - A_{sample}) / A_{control} \times 100 \quad \text{Eq. (5)}$$

where $A_{control}$ and A_{sample} are the absorbance of the blank and sample.

Determination of the thermal properties of CH-based films

The thermal properties were determined employing a DSC6200/EXSTAR6000 apparatus an inert nitrogen atmosphere at −50 to 150 °C and a heating rate of 10 °C/min.

RESULTS AND DISCUSSION

Size distributions and zeta potential of CurNEs

The mean diameters and zeta potential values of CurNEs are listed in Table 2. CurNE7 exhibited the smallest mean diameter (307.53±6.30 nm) ($p \leq 0.05$). The variety of the size distribution corresponded to the ratio of the oil to the aqueous phases, the increasing adsorption of the concentration of the aqueous phase, the decrease in the interfacial tension, and the formation of fine droplets. CurNE7 exhibited the highest absolute value (−15.43±0.74 mV) ($p \leq 0.05$). Additionally, the ultrasonication time is a crucial factor in preparing NE because prolonged time could increase the temperature from the cavitation-induced thermal effect, thus stimulating the deterioration and aggregation of neighboring droplets. Since CurNE7 exhibited a concise ultrasonication time (15 min) and demonstrated higher stability and uniformity, it was selected and integrated to CH for further investigations.

Table 2 Mean diameters and zeta potential of CurNEs

Condition	Mean diameter (nm)	Zeta potential (mV)
CurNE1	1023.00^{a}±13.00	-0.88^{b}±0.36
CurNE2	758.70^{b}±3.68	-0.69^{b}±0.26
CurNE3	360.67^{e}±2.29	-0.50^{b}±0.33
CurNE4	378.20^{d}±5.59	-0.52^{b}±0.48
CurNE5	533.23^{c}±3.68^{c}	-0.08^{b}±0.21
CurNE6	367.50^{de}±5.20	-0.73^{b}±0.38
CurNE7	307.53^{f}±6.30	-15.43^{a}±0.74

*Different letters in the same column indicate significantly different ($p \leq 0.05$).

Determination of the WVP of CH-based films

The CH–NE condition exhibited the lowest WVP (0.049 ± 0.001 $gmmm^{-2}d^{-1}kPa^{-1}$), followed by CH–CO, CH–CNE, and CH (Table 3). The improved WVP of CH–NE might be due to the presence of CurNEs in the inner film structure enhanced the water barrier properties by increasing the tortuosity, thereby generating the resistance of water vapour through the film. On the contrary, CH–CNE and CH–CO exhibited higher WVP than CH, however, compared with CH–NE, CH–CNE and CH–CO exhibited lower efficiencies, which were attributed to the weak structural integrities of the surface of the film.

Determination of the mechanical properties of CH-based films

CH exhibited the highest TS (8.82±0.19MPa), and CH–NE, CH–CNE, and CH–CO exhibited significant decreases in TS ($p \leq 0.05$) (Table 3). TS of CH–NE was attributed to the role of the NE composites as plasticizers, which affected the mechanical properties (TS) of the film. Therefore, the internal network and cohesiveness of the film were destroyed, and this reduced the TS. The following inconsistency was observed between TS and %E: CH–NE exhibited the highest %E (54.07±10.19), followed by CH, CH–CO, and CH–CNE ($p < 0.05$). This might be attributed to the fact that NE in CH–NE ensured efficient elongation and acted as a plasticizer to retain the extensibility. Furthermore, the increase in %E might be caused by the change in the mobility of the CH molecules.

Table 3 Tensile strength and %Elongation at break of CH composited films

Samples	WVP (g mm m^{-2} d^{-1} kPa^{-1})	Tensile (MPa)	%Elongation
CH	0.130^{a}±0.010	8.82^{a}±0.19	21.13^{bc}±0.64
CH-NE	0.049^{d}±0.001	7.96^{c}±0.22	54.07^{a}±10.19
CH-CNE	0.087^{b}±0.001	6.92^{d}±0.13	14.80^{c}±1.74
CH-CO	0.077^{c}±0.001	8.46^{b}±0.08	30.00^{bc}±7.21

*Different letters in the same column indicate significantly different ($p \leq 0.05$).

Determination of the antioxidant activities of CH-based films

The CH–NE condition exhibited five times higher antioxidant activity than CH (Table 4). Moreover, CH–NE exhibited the highest antioxidant activity probably because of the reduction in the droplet size of the CH incorporated NE, which promoted specific surface interaction, and afforded accelerated and very efficient free radical absorption. Additionally, the reduction in the size of the oil droplets improved the mass transfer and increased the release rate, dispersion, and kinetically stable suspension.

Determination of the thermal properties of CH-based films

CH exhibited a T_g of 80.71 °C, however, the T_g of the CH–NE film sample shifted to 71.34 °C, whereas those of CH–CNE and CH–CO shifted slightly higher to 78.82 and 83.42 °C, respectively (Table 4). It is known that the T_g is an important criterion for the miscibility of the components. In a completely miscible blend of two compounds, only one T_g was observed. The results indicating good miscibility by performing one T_g and forming of new hydrogen bonding networks appear. Furthermore, the decrease of T_g of CH–NE corresponded to the interaction between CH and CurNEs in the amorphous regions. The modification of CH by small amounts of additives, such as NEs, is induced owing to the plasticization effect, thus increasing the chain mobility in the amorphous regions, and decreasing the degree of crystallinity (Luangapai et al., 2021).

Table 4 WVP, antioxidant activities and T_g of CH composited films

Samples	mmol Trolox/g film	T_g (℃)
CH	0.39±0.02^{d}	80.7
CH-NE	2.11±0.09^{a}	71.3
CH-CNE	0.58±0.03^{c}	78.8
CH-CO	0.73±0.00^{b}	83.4

*Different letters in the same column indicate significantly different ($p \leq 0.05$).

In summary, to develop CH-based films by incorporating CurNEs on various modifications. CH–NE exhibited good appearance, enhanced WVP, %E and antioxidant activities. Additionally, the thermal analysis revealed that the films exhibited considerable miscibility of the components from CH and CurNEs. The results initiated and promoted an interesting development as an active ingredient for producing food packaging materials.

REFERENCES

Luangapai, F., Peanparkdee, M., & Iwamoto, S. (2022). Effects of a curcumin nanoemulsion on the physico‐chemical properties of chitosan‐based films. *International Journal of Food Science & Technology*, 57, 101-109.

Peanparkdee, M., Iwamoto, S., and Yamauchi, R (2016). Microencapsulation: A review of applications in the food and pharmaceutical industries. *Reviews in Agricultural Science* 4, 56-65

Evaluation of the impact of climate change on river temperature

Khadiza Akter Mousumi[1], Takeo Onishi[2], Ken Hiramatsu[2] and Toshifumi Imaizumi[3]

1. **The United Graduate School of Agricultural Science, Gifu University, 1-1 Yanagido, Gifu 501-1193, Japan**
2. **Faculty of Applied Biological Sciences, Gifu University, 1-1 Yanagido, Gifu 501-1193, Japan**
3. **Faculty of Agriculture, Shizuoka University, 1-1 Yanagido, Gifu 501-1193, Japan**

INTRODUCTION

In aquatic ecosystems, river temperature is a crucial indicator of biodiversity and sustainability. River discharge and water temperature directly affect water quality (Ducharne 2008; Haag and Westrich 2002; Ozaki et al. 2003), the growth rate and distribution of freshwater organisms (Eaton and Scheller 1996; Ebersole et al. 2001; Mohseni et al. 2003). The dynamics and kinetics of biochemical reactions are influenced by river temperature, which also affects the availability, behavior, and kind of aquatic species in the ecosystem to which it belongs. The availability and temperature of water are also economically important, for example for thermoelectric power production (Forster and Lilliestam 2011; Koch and Vo¨gele 2009; Manoha et al. 2008), drinking water production (Ramaker et al. 2005; Senhorst and Zwolsman 2005), fisheries (Bartholow 1991; FAO 2008; Ficke et al. 2007) and recreation (EEA 2008b; Webb et al. 2008). Climatic conditions have a strong influence on water temperature. The increase in stream temperatures has already been observed in many countries., including Austria (Webb and Nobilis 1994), China (Chen et al. 2016), Germany (Arora et al. 2016), Poland (Kedra and Wiejaczka 2018; Graf and Wrzesinski 2020), UK (Orr et al. 2015), Switzerland (Michel et al. 2020) or USA (Kaushal et al. 2010; Seekell and Pace 2011; Isaak et al. 2018). Changes to natural water temperature regimes can result in myriad effects on aquatic organisms, water quality, circulation patterns, recreation, industry, and utility operations. Consequently, livelihood of the inhabitants depending on the river will also change. So, tracking changes in water temperature is key to better understanding the potential effects of global climate change on freshwater ecosystems.

Predicting the impact of climate change on river systems is imperative for effective management of aquatic ecosystems. This study will demonstrate the potential impact of climate on rivers temperature and how this might affect the future ecological systems. The objectives of the study are:

- To evaluate the processes involving climatic, hydrologic, and their interactions that determine the stream temperature.
- To investigate the impact of air temperature and streamflow changes on river temperature.
- To investigate the effect of changing temperature on aquatic ecosystem.
- To determine the influence of changing stream temperature on water quality, habitats of river and on the lifestyle of people.
- To find the best way to mitigate climate change and to adapt with the changing situation
- To develop long-term strategies and management policies to match with climate change phenomenon.

MATERIALS AND METHODS

The study site for this research is Nagara river. The Nagara River has its source in the city of Gujō, Gifu Prefecture, and its mouth in the city of Kuwana, Mie Prefecture, Japan. With a length of 166 km (103 mi), it drains an area of 1,985 square kilometres (766 sq mi) in the Chūbu region and empties into Ise Bay. To evaluation climate change impacts on the study site the dataset of the following website will be used.

http://www.miroc-gcm.jp/~pub/d4PDF/index_en.html

Present and future climate data will be generated by using a regional climate mode through dynamic downscaling approach. In this study, a watershed hydrology model, Soil and Water Assessment Tool (SWAT) will be utilized to simulate flow which is developed by the United States Department of Agriculture (USDA) and one of the most widely used simulators for hydrologic modelling (Arnold et al. 2012). It is a semi-distributed hydrological simulator used to simulate several processes over an extended period, primarily in rural catchments (Arnold et al. 1998). The SWAT model has been extensively applied to various problems such as land cover changes, agricultural management, and climate changes. The several input data and their sources are given in the following table:

Table 1: Input data for SWAT and their sources

Data	Source
DEM	https://asterweb.jpl.nasa.gov/
Land use	https://www.eorc.jaxa.jp/ALOS/en/dataset/lulc_e.htm
Soil type	https://www.mlit.go.jp/en/
Discharge	http://www1.river.go.jp/

River temperature data will be observed in the research project '水防災・農地・河川生態系・産業への複合的な気候変動影 響と適応策の研究', which is funded by The Environment Research and Technology Development Fund of the Ministry of Environment.

Fig. 1: Points of observation for measuring river temperatures

EXPECTED RESULTS

- The results of the study will provide tool(s) that will determine the climate change effects on river temperature.

- The findings of the study will show the effects of changing river temperature on aquatic ecosystems and the local's livelihood on the river.
- The results of this study can be very useful in water resource planning, effective management of aquatic ecosystems.

REFERENCES

Arnold, J.G., Srinivasan, R., Muttiah, R.S., and Williams, J.R. (1998). Large area hydrologic modeling and assessment part I: model development. Journal of the American Water Resources Association 34 (1): 73–89.

Arnold, J.G., et al. (2012). SWAT: model use, calibration, and validation. American Society of Agricultural and Biological Engineers 55 (4): 18.

Arora, R., Tockner, K., and Venohr, M. (2016). Changing river temperatures in northern Germany: trends and drivers of change. Hydrological Processes, 30(17): 3084-3096.

Bartholow, J.M. (1991). A modeling assessment of the thermal regime for an urban sport fishery. Environmental Management 15: 833–845.

Chen, D., Hu, M., Guo, Y., and Dahlgren, R. A. (2016). Changes in river water temperature between 1980 and 2012 in Yongan watershed, eastern China: Magnitude, drivers, and models. Journal of Hydrology, 533: 191-199.

Ducharne, A. (2008). Importance of stream temperature to climate change impact on water quality. Hydrology and Earth System Sciences, 12(3): 797-810.

EEA, (2008b). Impacts of Europe's Changing Climate – Indicator-based Assessment. EEA, Copenhagen.

Eaton, J. G., and Scheller, R. M. (1996). Effects of climate warming on fish thermal habitat in streams of the United States. Limnology and oceanography 41(5): 1109-1115.

Ebersole, J. L., Liss, W. J., and Frissell, C. A. (2001). Relationship between stream temperature, thermal refugia and rainbow trout Oncorhynchus mykiss abundance in arid‐land streams in the northwestern United States. Ecology of freshwater fish, 10(1): 1-10.

FAO, (2008). Climate Change Implications for Fisheries and Aquaculture. FAO, Rome, Italy, p. 41.

Ficke, A.D., Myrick, C.A., and Hansen, L.J. (2007). Potential impacts of global climate change on freshwater fisheries. Reviews in Fish Biology and Fisheries 17: 581–613.

Forster, H., and Lilliestam, J. (2011). Modeling thermoelectric power generation in view of climate change. Regional Environmental Change 4: 327–338

Graf, R., and Wrzesiński, D. (2020). Detecting patterns of changes in river water temperature in Poland. Water 12(5).

Haag, I., and Westrich, B. (2002). Processes governing river water quality identified by principal component analysis. Hydrological processes, 16(16): 3113-3130.

Isaak, D. J., Luce, C. H., Chandler, G. L., Horan, D. L., and Wollrab, S. P. (2018). Principal components of thermal regimes in mountain river networks. Hydrology and Earth System Sciences 22(12): 6225-6240.

Kaushal, S.S., Likens, G.E., Jaworski, N.A., Pace, M.L., Sides, A.M., Seekell, D., Belt, K.T., Secor, D.H. and Wingate, R.L. (2010). Rising stream and river temperatures in the United States. Frontiers in Ecology and the Environment 8(9): 461-466.

Koch, H., and Vo¨gele, S. (2009). Dynamic modelling of water demand, water availability and adaptation strategies for power plants to global change. Ecological Economics 68: 2031–2039.

Kędra, M., and Wiejaczka, Ł. (2018). Climatic and dam-induced impacts on river water temperature: Assessment and management implications. Science of the Total Environment 626: 1474-1483.

Manoha, B., Hendrickx, F., Dupeyrat, A., Bertier, C., and Parey, S. (2008). Climate change impact on the activities of Electricite de France. Houille Blanche-Revue Inter nationale De L Eau 55–60.

Michel, A., Brauchli, T., Lehning, M., Schaefli, B., and Huwald, H. (2020). Stream temperature and discharge evolution in Switzerland over the last 50 years: annual and seasonal behaviour. Hydrology and Earth System Sciences 24(1): 115-142.

Mohseni, O., Stefan, H. G., and Eaton, J. G. (2003). Global warming and potential changes in fish habitat in US streams. Climatic change 59(3): 389-409.

Orr, H.G., Simpson, G.L., des Clers, S., Watts, G., Hughes, M., Hannaford, J., Dunbar, M.J., Laizé, C.L., Wilby, R.L., Battarbee, R.W. and Evans, R. (2015). Detecting changing river temperatures in England and Wales. Hydrological Processes 29(5): 752-766.

Ozaki, N., Fukushima, T., Harasawa, H., Kojiri, T., Kawashima, K., and Ono, M. (2003). Statistical analyses on the effects of air temperature fluctuations on river water qualities. Hydrological Processes 17(14): 2837-2853.

Ramaker, T.A.B., Meuleman, A.F.M., Bernhardi, L., and Cirkel, G. (2005). Climate change and drinking water production in The Netherlands: a flexible approach. Water Science and Technology 51: 37–44.

Seekell, D. A., and Pace, M. L. (2011). Climate change drives warming in the Hudson River estuary, New York (USA). Journal of Environmental Monitoring 13(8): 2321-2327.

Senhorst, H.A.J., and Zwolsman, J.J.G. (2005). Climate change and effects on water quality: a first impression. Water Science and Technology 51: 53–59.

Webb, B. W., and Nobilis, F. (1994). Water temperature behaviour in the river Danube during the twentieth century. Hydrobiologia, 291(2): 105-113.

Webb, B.W., Hannah, D.M., Moore, R.D., Brown, L.E., and Nobilis, F. (2008). Recent advances in stream and river temperature research. Hydrological Processes 22: 902–918.

Fate of plastic mulch residues in agricultural soil and its influence on soil properties response to soil amendment addition

Shiamita Kusuma Dewi[1] and Yongfen Wei[2]

1. **The United Graduate School of Agricultural Science, Gifu University, 1-1 Yanagido, Gifu 501-1193, Japan**
2. **River Basin Research Center, Gifu University, 1-1 Yanagido, Gifu 501-1193, Japan**

INTRODUCTION

Mulching is a practice of covering the soil to make favorable condition for plant growth, development, and efficient crop production. This technology is important especially in region with few precipitations since it not only has the function of preventing water evaporation, but also has many advantages such as reducing pesticides, preventing weeds and insect pests, and reducing soil erosion.

Polybutylene succinate-co-adipate (PBSA) is biodegradable polymer with high flexibility, processability, excellent impact strength and chemical resistant (Palai et a.l, 2021). Due to its semicrystalline characteristic this material is relatively easy to biodegrade and is used in the production of mulching film and packaging.

Low density polyethylene (LDPE) mulch film is widely used in farmland due to its ability to transmit long wave radiation, good mechanical properties and ease of placement and removal.

Plastic mulching practice has been globally applied for instants economic benefits such as higher yields, improved fruit quality and earlier harvest. However, it is reported that waste plastic mulch recycling rate is low, less than 30%. Residual plastic will accumulate in the soil and becomes smaller and smaller (microplastics) due to repeated fragmentation. As the result, plastic pollution has become one of the most pressing environmental concerns.

On the other hand, farmer often apply soil amendments during the agricultural practice. The addition of organic material such as crop residues, compost, biochar, animal manure can improve soil fertility, soil physical characteristic, and augment microbial activities. However, with the presence of organic material induced in soil, the fate of plastic mulch residues is remained unknown.

To study the fate of plastic mulch residues and to obtain empirical evidence on the potential effect of mulch plastic residue pollution on soil properties and microbial community, particularly when using different farming practice, an indoor soil incubation experiment was designed and carried out.

MATERIALS AND METHODS

Soil sample and amendments – Soil sample was collected from vegetable field located in Gifu University. Compost and biochar were used in the study as soil amendments. The compost came from a local company and was made from food waste and cow manure, and the biochar derived from rice husk and was obtained from TAKII SEED corporation. The soil was sieved through a 2-mm mesh sieve and homogenized for the next stage.

Mulch Plastic – Low density polyethylene (LDPE) and Polybutylene succinate adipate (PBSA) mulch films were cut into a square shape manually with cutter and ruler. The size was 10 mm large. The weight for PBSA was 2.1556 ± 0.11042 mg/piece and LDPE was 1.7004 ± 0.08921 mg/piece. To minimize microbial contamination, mulch plastic film pieces was exposed to ultraviolet in clean bench for 20 minutes.

Mulch plastic and amendments addition to soil – The soil was mixed with each type of mulch plastic film at a concentration of 0.1% (w/w) and soil amendment with dose 15-ton ha^{-1}. Therefore, 0.5 g of each mulch plastic films, and 3.75 g of each soil amendment were mixed into 500 g of soil by stirring with spoon in a big container before transferring the mixture into each experimental box with size of 14.8 cm (length) × 10.8 cm (width) × 10.1 cm (height). Experiment design and treatments were shown in **Fig. 1**. Each treatment has 3 replicates; therefore, totally 27 boxes were prepared.

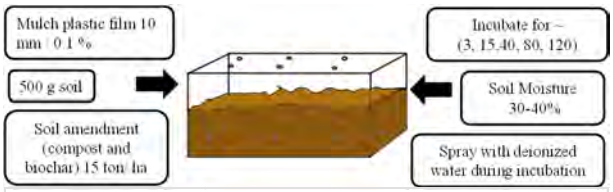

Experimental Treatments		
Control	PBSA	LDPE
Compost	PBSA+Compost	LDPE+Compost
Biochar	PBSA+Biochar	LDPE+Biochar

Fig. 1 Experimental design and treatments (Soil Incubation)

Experiment boxes were kept at 27ºC throughout the incubation period. And to maintain soil moisture at 30-40 %, every 6 days were sprayed with distilled water. Soil was randomly collected on the 3rd, 15th, 40th, 80th, and next 120th days for measurement.

Measurement – The basic physicochemical properties of soil and amendments are summarized in Table 1. The pH and EC (electrical conductivity) were measured in the supernatant suspension of sample in water with ratio 1:5 (w/v), OM (organic matter) was determined as the loss in ignition (LOI) at 600ºC. TN (total nitrogen) and OC (organic carbon) were measured by using a nitrogen and carbon analyzer.

Mulch plastic film pieces were taken manually with tweezers, washed with distilled water and the impurities were removed with Fenton's reagents for 20 min at 25ºC. Dried samples were weighed by analytical microbalance. And surface morphology of mulch plastic films was visualized by scanning electron microscopy (SEM/EDX).

Table 1. Physicochemical properties of the soil and amendments

Parameter	Soil	Compost	Biochar
pH	7.34 ± 0.02	8.08 ± 0.05	10.09 ± 0.04
EC (dS m-1)	0.19 ± 0.00	6.25 ± 0.17	1.01 ± 0.01
OM content (%)	6.08 ± 0.04	67.83 ± 2.61	17.03 ± 4.31
TN (g kg-1)	3.92 ± 0.74	33.39 ± 0.52	5.10 ± 0.97
OC (g kg-1)	16.30 ± 1.05	305.36 ± 12.53	192.07 ± 10.41

Note: values represent mean ± standard deviation (n =3), EC: electrical conductivity; OM: organic matter; TN: total nitrogen; OC: organic carbon.

Statistical analysis – The data are reported as the means ± standard deviation (SD). Significant differences ($p < 0.05$) were tested via ANOVA using SPSS 19.0. The differences in mulch plastic films weight and total nitrogen content were compared between samples incubated in different days while pH values

were compared between sample in different soil amendments ($p < 0.05$) via one way ANOVA in conjunction with Tukey's honestly significant difference (HSD).

RESULTS

Soil properties — The experimental result for soil pH and total nitrogen (TN) after the start of cultivation are as follows: No significant differences found in soil pH with the addition of soil amendments and mulch plastic residue contamination (PBSA and LDPE) compared to control treatment (**Table 2**). However, there was a significant difference in soil pH value on day 3 of the incubation period between the addition of biochar and compost under both mulch film contaminations.

Table 3 shows TN values under different treatments. In cases of Control, PBSA+Compost and LDPE +Biochar treatments, TN were significantly increased on day 15 and declined on day 40. The highest TN value (7.52 g kg^{-1}) was observed on day 15 in the case of LDPE with biochar amendment.

Table 2. Soil pH at different period of incubation

	Periods of Incubation		
Treatment	3 days	15 days	40 days
Control	7.35 ± 0.08 ab	7.53 ± 0.03 ab	7.35 ± 0.06 a
PBSA	7.43 ± 0.12 a	7.54 ± 0.10 ab	7.40 ± 0.04 a
PBSA + Compost	7.17 ± 0.04 b	7.40 ± 0.07 b	7.34 ± 0.04 a
PBSA + Biochar	7.45 ± 0.02 a	7.59 ± 0.06 a	7.41 ± 0.06 a
Control	7.35 ± 0.08 ab	7.53 ± 0.03 a	7.35 ± 0.06 a
LDPE	7.36 ± 0.09 ab	7.56 ± 0.04 a	7.39 ± 0.05 a
LDPE+ Compost	7.23 ± 0.05 b	7.45 ± 0.12 a	7.38 ± 0.01 a
LDPE + Biochar	7.43 ± 0.01 a	7.61 ± 0.03 a	7.31 ± 0.04 a

Note: Value represent mean ± standard deviation (n=3). Different letter (a-b) indicates that significant difference ($p < 0.05$) exists among treatments within the same mulch plastic films contamination.

Table 3. TN of soil at different period of incubation

	Periods of Incubation		
Treatment	3 days	15 days	40 days
Control	4.61 ± 0.45 B	7.05 ± 1.27 A	3.38± 0.65 B
PBSA	4.12 ± 0.56 A	6.12± 1.58 A	3.70 ± 0.65 A
PBSA + Compost	4.11 ± 0.56 B	6.84 ± 1.21 A	3.58 ± 0.39 B
PBSA + Biochar	5.21 ± 1.00 A	5.81 ± 0.96 A	4.26 ± 0.92 A
LDPE	3.46 ± 0.06 A	5.82 ± 1.81 A	3.76 ± 0.63 A
LDPE+ Compost	4.98 ± 0.94 A	6.76 ± 2.15 A	3.62 ± 0.53 A
LDPE + Biochar	3.70 ± 0.26 B	7.52 ± 0.71 A	3.29 ± 0.46 B

Note: Value represent mean ± standard deviation (n=3). Different letter (A-B) indicates that significant difference ($p < 0.05$) exists among treatments within period of incubation.

The weight and surface morphology of mulch plastic pieces- For the weight of mulch plastic pieces, a downward trend was observed in all treatments. After 40 days of incubation, as shown in **Fig. 2,** the weight of PBSA significantly decreased by 29.87% in control treatment, while 16.38% in compost and 19.32% in biochar addition. No significance differences were found in LDPE' weight.

Regarding the surface morphology of LDPE and PBSA, as shown in **Fig. 3c** and **3a,** a smooth surface was observed on day 3 of incubation for both plastics. However, we found that at 40 days PBSA pieces were fragmented into smaller pieces with coarse surface (**Fig. 3b**) upon biochar addition. Even no significant differences were found in weight change of LDPE, the degradation has started to occur which can be seen in **Fig. 3d** that shows the abrasive surface of LDPE under biochar addition.

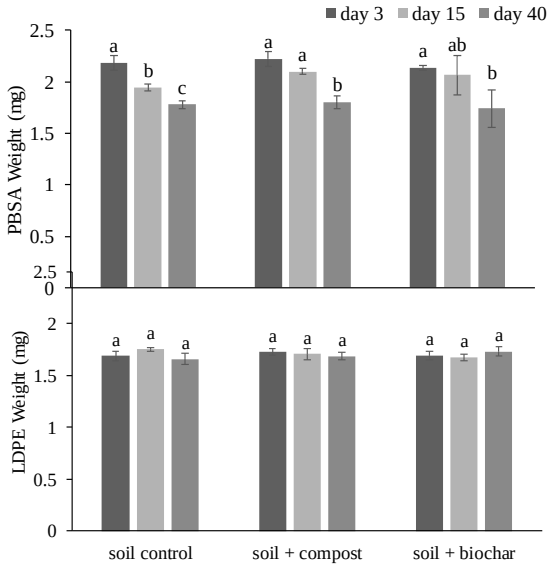

Fig. 2 Changes in weight of plastic mulch pieces with compost and biochar addition.

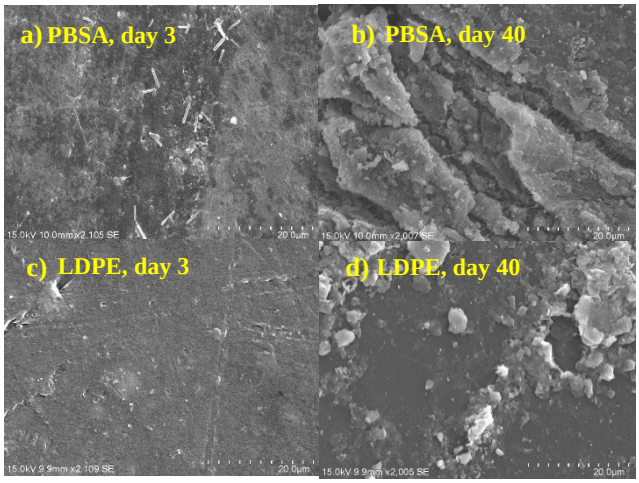

Fig. 3 Surface morphology of PBSA and LDPE on day 3 and day 40 under biochar treatment.

In this study, the fate of plastic mulch residues in agricultural soil and its influence on soil properties response to soil amendment addition was carrying out. The following results were obtained.

1. After 40 days incubation, no significant differences found in soil pH within all treatments.
2. TN observed on day 15 shown significantly increased then declined on day 40 in cases of Control, PBSA+Compost and LDPE+Biochar treatments.
3. Degradation rates of PBSA films ranged from 16.38% - 29.87% after 40 days.

REFERENCE

Palai, B., Mohanty, S. and Nayak, S.K. (2021) A Comparison on Biodegradation Behaviour of Polylactic Acid (PLA) Based Blown Films by Incorporating Thermoplasticized Starch (TPS) And Poly (Butylene Succinate-Co-Adipate) (PBSA) Biopolymer in Soil. Journal of Polymers and the Environment 29(9). pp. 2772–2788

Highly accurate estimation of swell components using ocean wave model

Shota Iguchi[1], Jun Yoshino[1] and Tomonao Kobayashi[1]
1. Gifu University, 1-1 Yanagido, Gifu 501-1193, Japan

INTRODUCTION

Renewable energies are currently attracting attention for realization of a decarbonized society, Offshore wind power is in the spotlight as one of the energies. However, the design and installation of offshore wind towers requires accurate prediction of waves, and wave model have difficulty predicting the swell component of waves. This is because the swell component is easily deformed in shallow water due to its long wavelength and propagates over long distances.

Therefore, this study investigates a calculation setup that can accurately estimate the swell component by changing the size of the calculation domain and calculation parameters using the wave model, named SWAN.

METHODS

In this study, we set up four calculation regions for the analysis points and investigate which region is the best to calculate from by examining how much the estimated values change at each nesting stage. The effect of changing the wave direction resolution will also be investigated.

—Model used and observation data

SWAN used in this study is one of the third-generation wave model, and it takes into account the wave characteristics of shallow-water areas, such as sea-bottom friction and shallow-water breaking waves [1]. It also uses a spectral method, which allows the wave components to be broken down into wind waves and swells, depending on the period. In SWAN, waves with a period of 10 seconds or longer are considered as swells. Data provided by Nationwide Ocean Wave information network for Ports and HArbourS (NOWPHAS) [2] is used as observation data for accuracy comparison. However, since data on the swell component is not provided, comparisons are made based on significant wave heights and periods in wave fields with long significant wave periods.

—Model used and observation data

The computational settings for SWAN in this study are shown in Table 1 and the computational domain for nesting set up is shown in Figure 1. The calculation period shown in Table 1 is one of several periods selected for eases of analysis due to the large changes in wave heights during the year 2019. The first five days of the calculation period are used for spin-up. The calculation was performed off the coast of Fukushima Prefecture, where NOWPHAS stations are located, in the Pacific Ocean coastal region where swells are easily transmitted from far in the ocean. The wave direction resolution and sea-bottom friction coefficient are the settings recommended by SWAN for swell estimation. The computational domain shown in Figure 1 has a grid spacing (resolution) of 2° × 2° (about 220 km × 220 km) for Domain 01, the largest domain, and the spacing decreases by a factor of 4 as the domain becomes smaller (resolution increases by a factor of 4). Table 2 shows case divisions for each stage of nesting.

RESULTS AND DISCUSSIONS

—Estimation results by nesting

Figure 2 shows the results of estimation for each of the cases

Table 1: Statistical error indices of predictions

analysis period	2019/5/15 ~ 2019/5/30
analysis point	Off the coast of Fukushima Prefecture （ 36.95°N, 141.20°E ）
coefficient of friction on the seafloor	0.038m²s²
resolution of wave direction	5°
wind data	NCEP FNL-0.25 [3]
resolution of wind data	0.25° × 0.25°
time interval of wind data	3 hours
submarine topographic data	ETOP01 [4]

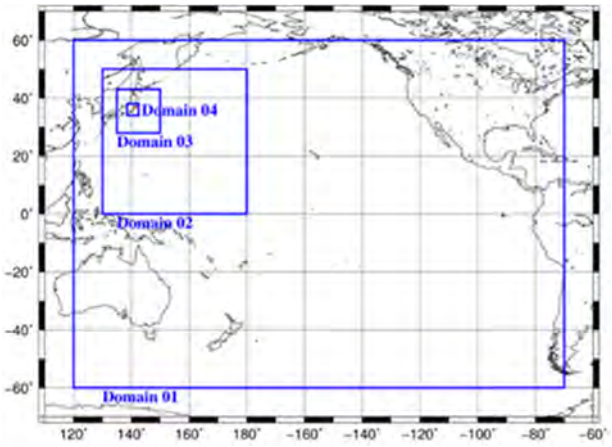

Fig. 1: Range of each calculation area set

Table 2: Nesting phase per case

case A	Domain 01～04
case B	Domain 02～04
case C	Domain 03～04
case D	Domain 04

listed in Table 2. Significant wave heights in the figure seem similar in each case, so the values can be viewed as pure wave heights. The larger the period of a significant wave, the larger the wave component with a longer period, and thus a larger estimated value means that more swell components with long periods are predicted.

The closest to the observed wave height and period to the estimated value was case B. Case A shows almost exact values for the May 21 peak, but slightly larger values overall. On the other hand, for cases C and D, the peak values are quite close to the observed values, but the values are basically smaller than the observed values.

The increase in wave height on May 21 may be induced by the low pressure cyclone in the vicinity of Japan. Figure 3 shows the distribution of the sea surface winds at that time, and it can be seen that the location where the sea surface wind disturbance became larger due to the pressure configuration extends beyond the range of Domain 03. Therefore, Figures 4 and 5, which show the distribution of wave heights on the day, show that the swell

generated in case B came intermittently, while it was interrupted in case C.

—Estimation results by changing wave height resolution

Next, we examined how much the estimated values would change if the wave direction resolution was increased from 5° to 2° to make the wave direction finer. The results are shown in Figure 6. From this figure, it can be seen that both cases E and F are closer to the observed values than the estimated values for cases A and B.

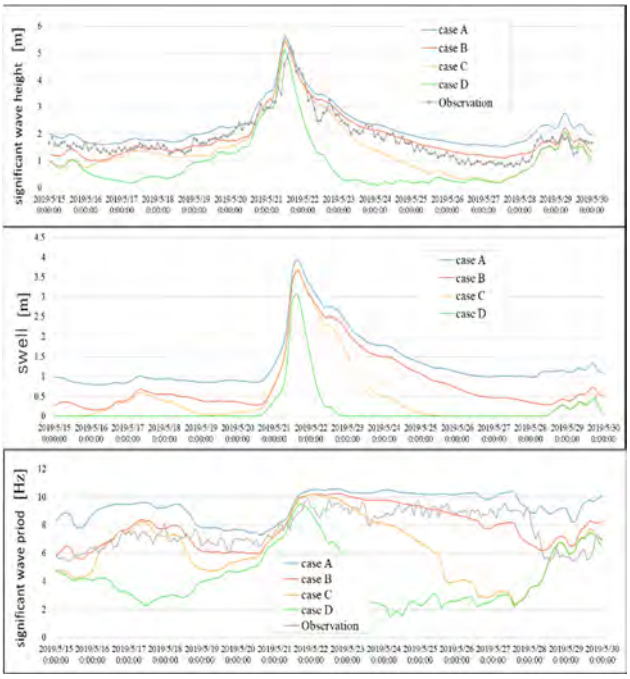

Fig. 2: The results of estimation by SWAN (case A, B, C, D) (Upper: significant wave height, Middle: swell, Lower: significant wave period)

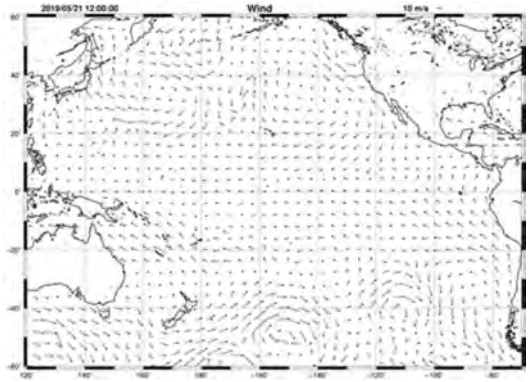

Fig. 3: Wind distribution on May 21

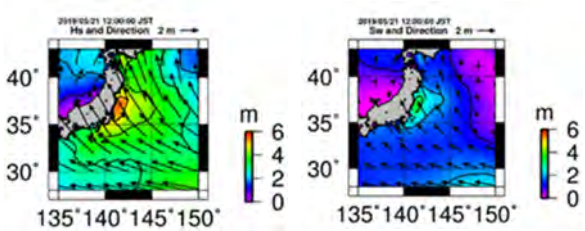

Fig. 4: Wave height distribution on May 21 (case B) (Left: significant wave, Right: swell)

CONCLUSIONS

The results of the estimation performed in this study indicate that, in order to accurately estimate the far-field swell component, it is necessary to establish a domain large enough to include most of the offshore wind disturbances within the calculation domain. However, it was also found that calculations from too large a region may overestimate the swell. In such cases, it was found that increasing the wave direction resolution can more accurately calculate the propagation of waves over long distances and improve the accuracy of wave height and period estimation.

REFRENCES

[1] SWAN USER MANUAL (SWAN Cycle Ⅲ version 41.01)

[2] Real Time Nowphas < https://www.mlit.go.jp/kowan /nowphas/index.html > (last visited Sep 18, 2022)

[3] Wind data on a 0.25° x 0.25° grid from the U.S. National Centers for Environmental Prediction (NCEP)

[4] Digital topographic data created by the National Oceanic and Atmospheric Administration (NOAA)

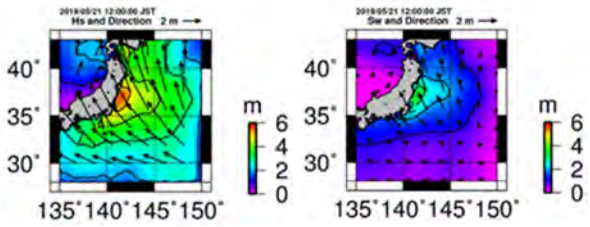

Fig. 5: Wave height distribution on May 21 (case C) (Left: significant wave, Right: swell)

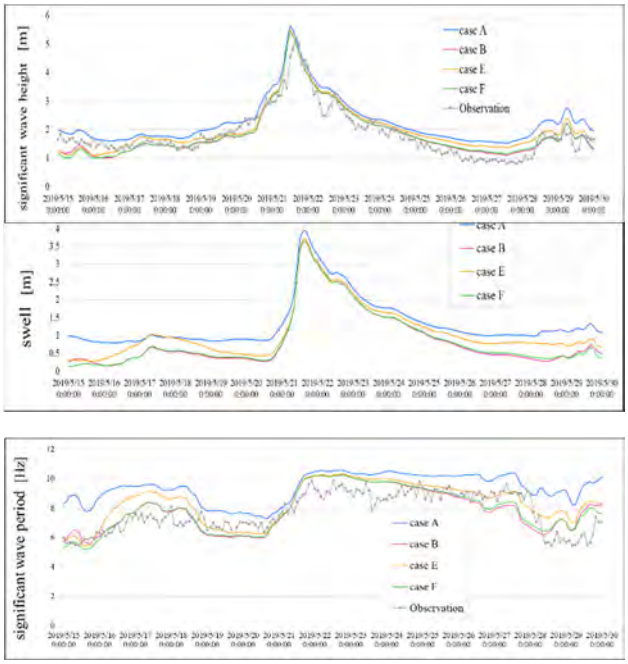

Fig. 6: The results of estimation by SWAN (case A, B, E, F) (Upper: significant wave height, Middle: swell, Lower: significant wave period)

High-resolution analysis of atmospheric optical fluctuations for laser communication using WRF model

Naoya Shimpuku[1], Jun Yoshino[1], Ichiro Tamagawa[1] and Tomonao Kobayashi[1]
1. **Gifu University, 1-1 Yanagido, Gifu 501-1193, Japan**

INTRODUCTION

Laser-based communications perform with ultra-high speed, high capacity, high reliability, compare with the current microwave-based ones. However, the quality of the communication is strongly dependent on the atmospheric conditions when they are used on the earth, because the atmospheric fructurations cause of instabitily of laser paths and suspeneded matters reduce its intensity. In daytime, the warm air is usually layered near the ground due to heating by the sunshine. The temperature difference in the layered air creates a density difference, which causes convection and fluctuations in the refractive index. In communications using laser beams, atmospheric fluctuations are risk of communication quality such as its degradation and interruption. In order to maintain the quality of this optical communication, the distribution (1) of the structure coefficient of refractive index fluctuation Cn^2, which is an index related to fluctuations, is predicted at high resolution with a numerical weather model.

METHODOLOGY

The numerical weather forecasting model, WRF (2) is employed for representing the meteorological condition near the ground in this study. It's usually used for simulating the weather in resolution from 1 km to several thoudand km. However, we calculate the weather finer than the usual use for evaluation of Cn^2. With this simulation, the popular meteorological parameters, such as the temperature, wind, and also special ones, like turbulence, friction velocity and heat transportation.

The optical fluctuation in the atmosphere is caused by layered thermal distributions and turbulent intensity of atmosphere. They are expressed with Monin-Obukhov's similarity rule (3) near the ground. It is evaluated from some meteological parametes; e.g. friction velocity and frictuation of temperature. These parameters are from represented weather condition simulated with WRF.

This calculation is performed for each horizontal and vertical grid, and the distribution of the structure coefficient of refractive index variation Cn^2 in the atmosphere is calculated and output as a figure.

MODEL SETTINGS

The center of this study was set at 35.4635°N, 136.7472°E, where is near Gifu University. Table 3.1 accounts for the optional settings in the WRF for this study. The computational domain was set up with four levels of two-way nesting (Fig. 3.1) to enable the analysis of optical path scale resolution. Only Domain 4 was set to be calculated using LES (Large Eddy Simulation). The calculation period was set from August 1, 2019, the day of the heat wave, to August 2, 2019 (UTC in Table 3.1). Calculations were performed one hour in advance for the purpose of familiarizing the calculations.

RESULTS

It was thought that many calculations would not satisfy the CFL condition (4) in the WRF calculation for Domain 4, so the calculation did not run properly and was limited to 19 hours. Therefore, the results show the distribution of the structure coefficient Cn^2 of the refractive index variation of the vertical section as shown in Figure 4.1 for every minute for 19 hours.

Table 3.1 WRF settings

input data	initial value: Local Forecast Model GPV(LFM) （Horizontal resolution 2km, Every 3 hours ）
	NCEP GFS-0p25 forecast value （Horizontal resolution 0.25°， 3 hour intervals）
computation period	2019-07-31_23:00:00 UTC ～
	2019-08-02_00:00:00 UTC
Computational domain	Domain 1 : 3km×3km （100×100 grids）
	Domain 2 : 1km×1km （100×100 grids）
	Domain 3 :333m×333m （100×100 grids）
	Domain 4 : 111m×111m （100×100 grids）
Number of vertical layers	55 layers （ground surface～500hPa）

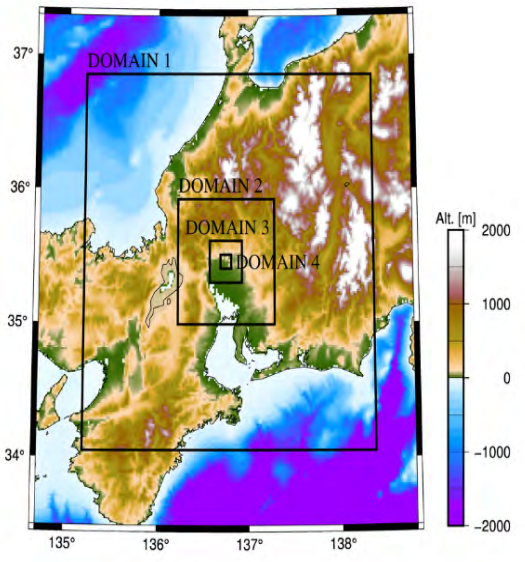

Figure 3.1 WRF nesting setting area Domain1～Domain 4

The horizontal axis of this figure indicates the east-west distance (m), the vertical axis indicates the elevation (m), and the arrows indicate the wind speed and direction in the vertical planes. The closer to the warmer color, the larger the value of the structure coefficient of refractive index variation Cn^2, indicating atmospheric instability.

Figure 4.2 shows the horizontal wind speed u (m/s) and vertical wind speed w (m/s) at the point of 777 m in altitude and 2,500 m in horizontal direction (black dot in Figure 4.1) and $\log_{10} Cn^2$ time variability time average (black line) and variability component (red line), respectively.

DISCUUSIONS

Figure 4.2 shows the horizontal wind speed u (m/s) and vertical wind speed w (m/s) at the point of 777 m in altitude and 2,500 m in horizontal direction (black dot in Figure 4.1) and $\log_{10} Cn^2$ time variability time average (black line) and variability component (red line), respectively.

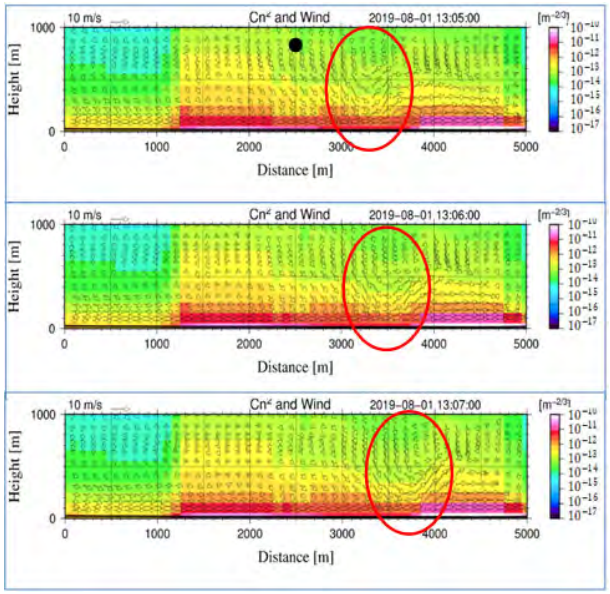

Figure 4.1 Change in the distribution of Cn^2

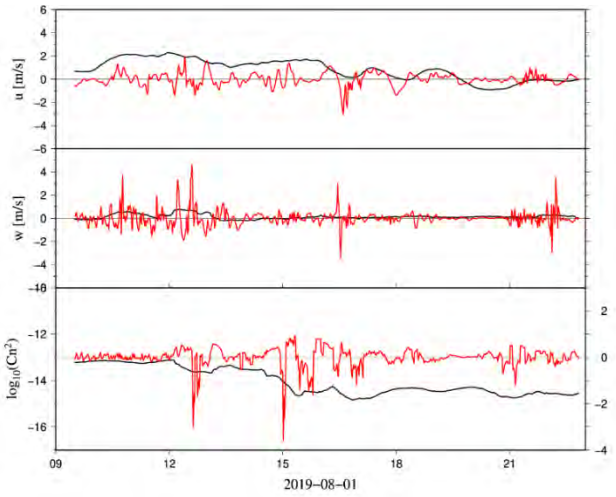

Figure 4.2 Time averaged and fluctuating components of vertical wind speed u and horizontal wind speed w and Cn2

5.1 Short-time horizontal variation of Cn^2

We can see wind speeds that behave like waves at the red circle in Figure 4.1. In the same region, there is a green region which correspond to the low Cn^2. Since both of them seem to be moving in the east-west direction, it is thought that air masses with a certain structure coefficient of refractive index variation Cn^2 are advected from the west to the east by the wind.

5.2 Vertical variation of Cn^2

As shown in 4.1, we can find the vertical downward wind and the vertical upward wind in the red circle. When there is downward wind, the green area, that is, the area where the value of the structure coefficient of refractive index variation Cn^2 is smaller than that of the surrounding area, can be seen in the large area. In the blue regions at the west side vertical downwind can also be found. It is thought that the air in the region with small (large) structure coefficient of refractive index variation Cn^2s advected downward (upward) by the vertical downward wind.

5.3 $\log_{10} Cn^2$ Regarding time variation

Focusing on the time averages in Figure 4.2, we can see that $\log_{10} Cn^2$ maintains an unstable value during the day and shows stability during the night. From this, we can assume that $\log_{10} Cn^2$ will increase with the sunrise in the morning when we could not obtain the result. In addition, when we focus on the fluctuation components, we can see that when local horizontal or vertical fluctuation in wind occurs, the fluctuation of $\log_{10} Cn^2$ is also remarkable. Especially when the wind speed in the vertical direction fluctuates locally and extremely, the fluctuation component of $\log_{10} Cn^2$ also tends to fluctuate evidently. When the local vertical upward wind blows, $\log_{10} Cn^2$ is small, and when the local vertical downward wind blows, the value of $\log_{10} Cn^2$ seems to fluctuate to a large value. It can be inferred that the air masses showing respective $\log_{10} Cn^2$ are advected both horizontally and vertically by the wind.

REFERENCES

(1)N. Akiyama, T. Kobayashi, J. Yoshino, I. Tamagawa, H. Yoshida, and Y. Takayama: Atmospheric transmission and stability for satellite-to-ground optical communication, Proc. of Space Science and Technology 64th, 1C10, 2020
(2)WRF Model Users Page:
http://www.mmm.ucar.edu/wrf/users/
(3)Monin, A.S. and A.M. Obukhov, 1954: Basic laws of turbulent mixing in the surface layer of the atmosphere. Contrib. Geophys. Inst. Acad. Sci., USSR, (151), 163–187 (in Russian).
(4)Seiichi Koshizuka, "Numerical Fluid Dynamics", Kaifukan, 1997, p. 26 - p. 27

Antibiotic resistance genes and 16S rDNA in large *Johkasou* treating residential area domestic wastewater

Haoning Su[1], Shinya Okumura [1], Yasushi Ishiguro [2] and Fusheng Li [2]
1. **Graduate School of Engineering, Gifu University, 1-1 Yanagido, Gifu 501-1193, Japan**
2. **River Basin Research Center, Gifu University, 1-1 Yanagido, Gifu 501-1193, Japan**

INTRODUCTION

Antibiotic resistance genes (ARGs) are emerging environmental contaminants and pose serious threat to public health. Wastewater from livestock, agriculture, industry, hospitals, antibiotic manufacturers, and households is the main source of ARGs. For *Johkasou*, a facility used to treat domestic wastewater from residential area simply, research related to ARGs is limited. The objectives of this study were (1) to quantify the ARGs in the wastewater of the whole treatment process in *Johkasou*, (2) to investigate the existing form of ARGs in relation to the size of suspended solids in treated wastewater, and (3) to explore the relation between ARGs and microbial activity.

METHODS

(1) Sample collection and pre-treatment

Water and sludge samples were collected from eight sampling points (**Fig. 1**) in a large-scale Johkasou located in Aichi, Japan. Sampling was performed weekly in 2 months, corresponding to the operation time after accumulated sludge cleaning. Samples were divided into two parts for storage: for physicochemical parameter analysis, samples were stored at 4 °C and processed within 48 h; and for ARGs analysis, samples were stored at −20 °C before analysis.

To classify ARGs on the remained suspended solids, sieves with the opening of 250, 125, 75 and 25μm respectively, and a membrane filter with the pore size of 3 μm were used to filter the treated wastewater. The filtrates were used for ARGs quantitation.

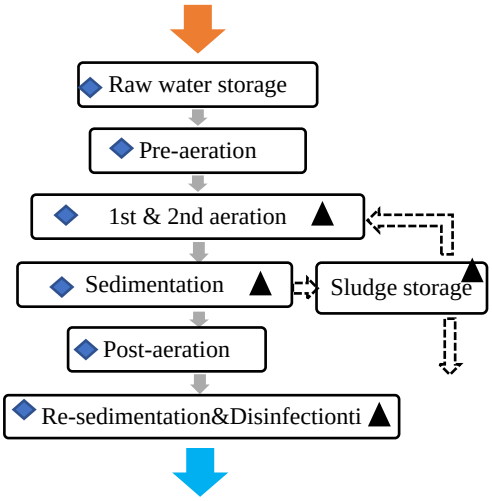

Fig. 1: Schematic flow diagram of the *Johkasou* with the sampling points (Water sample; Sludge sample).

(2) DNA extraction and determination of genes

DNA extraction for all samples was conducted using Power Soil DNA Extraction Kit (MOBIO, USA) based on manufacturer's manual. The extracted DNA was stored at −25 °C for determination of target genes by quantitative PCR (qPCR). Tetracycline resistance gene (*tet G*), a mobile genetic element (MGE) (integrase class 1 gene, intl 1), and total bacteria reflected by 16S rDNA were quantified by qPCR with the utilization of SYBR® Premix Ex Taq™ (TaKaRa, Japan) based on the manufacturers' manual.

RESULT AND DISCUSSION

(1) Abundance of ARG and MGE during treatment

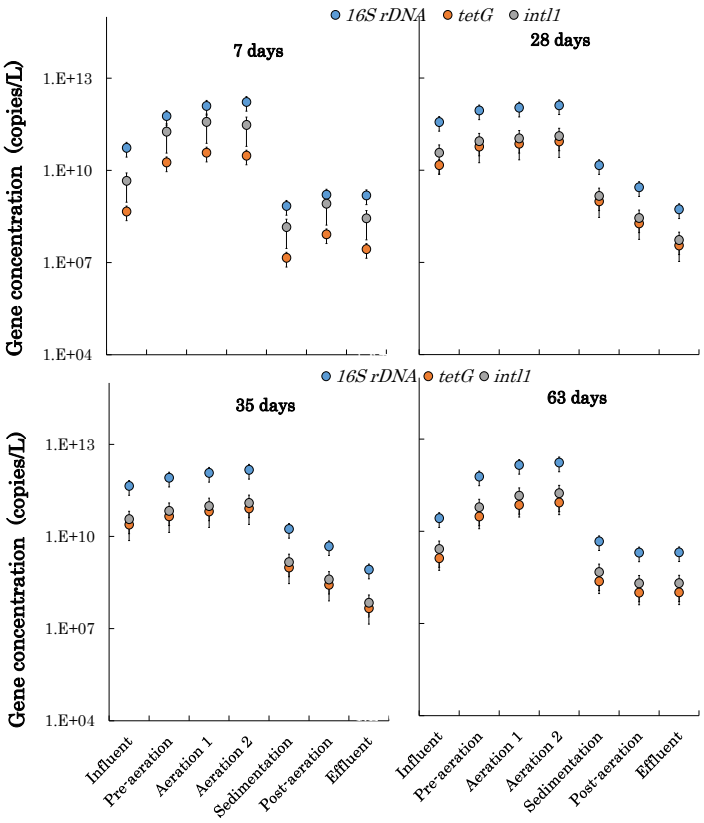

Fig. 2: Concentration changes of ARGs in wastewater during treatment (The data of 7, 28, 35 and 63 days after cleaning were plotted here as the examples).

The abundance of ARG, MGE and 16SrDNA in the treatment process showed *tetG* and *intl1* existed in all wastewater samples and more genes existed in biological treatment units (Pre-aeration, 1st aeration and 2nd aeration) with more microbial diversity and interactions (**Fig. 2**), possibly due to the high abundance, density, activity, and interactions of bacteria increase the rate of gene transfer. The reduction of genes observed in the sedimentation tank may indicate, most of the resistance genes that arrives with the wastewater and that grows and propagates through the treatment facility end up in the settled sludge. In the operation of 7 to 63 days after sludge cleaning, the fate and behavior of ARGs were similar, but the extent of ARGs reduction was higher for the time of 28 and 35

days from the influent to the effluent: 2.6 and 2.7 log removal of tetG; 2.8 and 2.7 log removal of intl1 (**Fig. 3**).

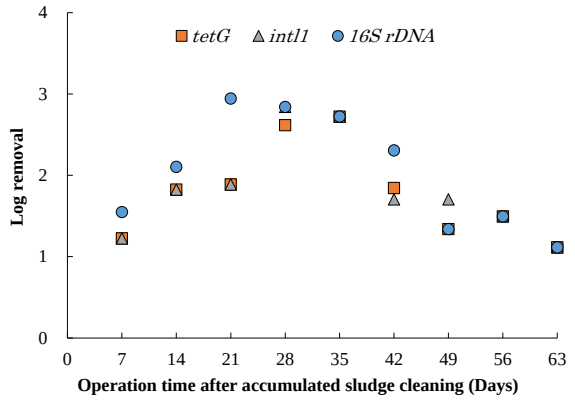

Fig. 3: Log removal of *tetG*, *intl1* and 16S rDNA in the operation time after sludge cleaning.

(2) Distribution of ARG on suspended solids

tetG and *intl1* were detected in all filtrates, with their concentrations varying within one order of magnitude (**Fig. 4A**). For the absolute abundances based on the dry weight of suspended solids, The highest absolute abundances of *tetG* and *intl1* were found in filtrate with small microparticles which are less than 3 µm (**Fig. 4B**). Compared to larger suspended particles, small particles are difficult to settle and can transport easily to the receiving water body. Therefore, the potential risk of the proliferation of ARGs is high.

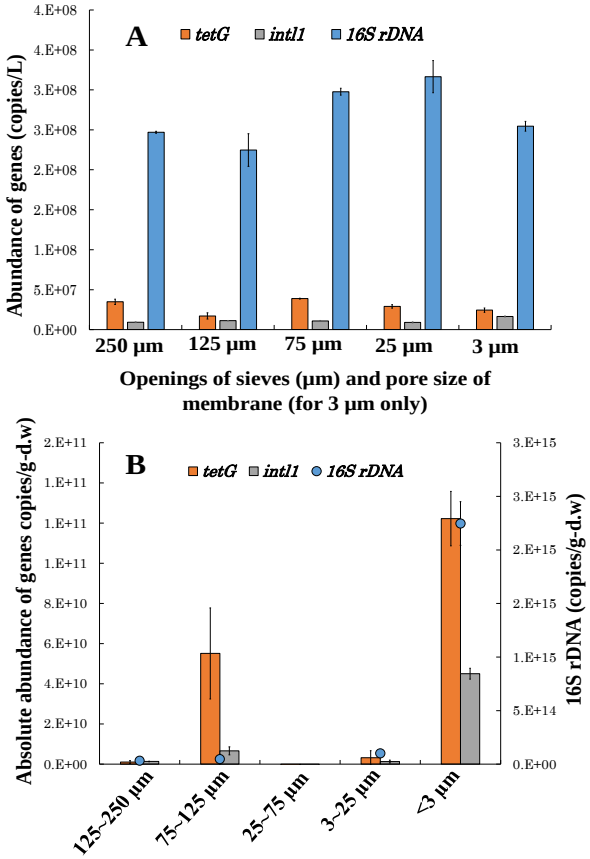

Fig. 4: tetG, intl1 and 16S rDNA abundance in treated wastewater after filtration through different sieves or membrane (A), and the absolute abundance in treated wastewater with different size (B).

(3) Correlations between ARG and microbial activity

The large-scale *Johkasou* contains an activated sludge sequencing batch reactor, and the high abundance, diversity, activity, and interactions in the reactor may suggest an increased rate of gene transfer, through horizontal and/or vertical transfer of ARGs (Qin et al., 2020).

The correlation analysis of the resistance genes and microbial activity in sludge is shown in **Fig. 5**. *tetG* and DHA showed positive correlations in the 4 sets of data after sludge cleaning for 14, 21, 28 and 35 days. Positive correlations may suggest that higher microbial activity could probably lead to a higher rate of gene dissemination. Additionally, the sludge with higher DHA also showed better settleability (SVI ranged from 91.0 to 116.8 mL/g), so more ARGs can be concentrated in the settled sludge.

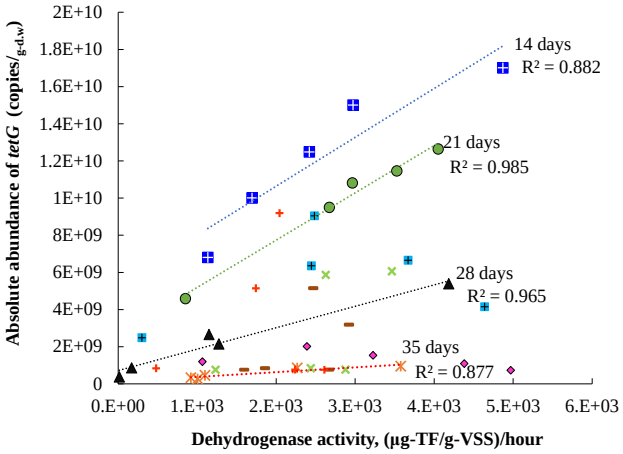

Fig. 5: Correlations between tetG and DHA in the sludge with different cleaning time intervals.

In this study, *tetG* and *intl1* were found existent in the whole treatment process of the investigated large-scale *Johkasou* for treating residential area domestic wastewater, more ARGs and 16SrDNA were found in biological treatment units. Positive correlations between *tetG* and DHA were revealed in the sludge. Higher abundance of ARGs is possibly due to the higher levels in bacteria concentration and microbial activity, which increased the rate of gene transfer. In the effluent, ARGs were detected from suspended particles with different sizes (including those with sizes below 3 µm), fine particles with this size are difficult to settle and exist in the treated water as suspended solids. Consequently, the high potential risk of ARGs dissemination is substantial.

Further investigations are required in order to line out the quantification of other ARGs (*sul1*, *sul2*, *qnrA* and *qnrS*) on the suspended particles with different sizes during the whole treatment process

REFERENCE

Zhou, C., Yin, J., (1996) A method for measurement of ttc-dehydrogenase activity. Acta Scientiae Circumstantiae. CNKI:SUN:HJXX.0.1996-04-003.

Ashbolt NJ, Amézquita A, Backhaus T, Borriello P, Brandt KK, Collignon P., (2013) Human health risk assessment (HHRA) for environmental development and transfer of antibiotic resistance. Environ Health Perspect121(9):993–1001.

Qin, K., Wei, L., Li, J., Lai, B., Zhu, F., Yu, H., Zhao, Q., Wang, K., (2020) A review of ARGs in WWTPs: Sources, stressors and elimination, Chinese Chemical Letters, Volume 31, Issue 10.

Statistical analysis of solar radiation under future climate in Chubu region

Tomoki Kitaoka[1], Jun Yoshino[1] and Tomonao Kobayashi[1]
1. Gifu University, 1-1 Yanagido, Gifu 501-1193, Japan

INTRODUCTION

Global warming is currently a major problem around the world. As a result, demand for power generation from renewable energy sources that do not emit greenhouse gases is increasing. The same as the other countries, Japan is also moving toward a decarbonized society and is focusing on renewable energy. Among these, solar power generation, which can utilize unused space and has high energy generation efficiency, is becoming increasingly popular. However, solar power has the disadvantage of being susceptible to climate change. If solar power generation continues to become more widespread, the effects of climate change on solar power generation will become more pronounced.

This study aims to estimate and analyze changes in solar radiation in the future climate for the Chubu region. Using the weather forecast database d4PDF, we will estimate solar radiation under the future climate.

MATERIALS

The d4PDF is an ensemble climate prediction database that contributes to global warming countermeasures. In order to fully evaluate the uncertainties associated with infrequent extreme weather events, the Ministry of Education, Culture, Sports, Science and Technology and the Climate Change Risk Information Creation Program conducted an unprecedentedly large number of ensemble experiments (up to 100 members) using high-resolution global atmospheric models and high-resolution regional atmospheric models, and the d4PDF is a database of the experimental results. The calculations were performed using the Earth Simulator under the "Earth Simulator Special Proposal" conducted by the Japan Agency for Marine-Earth Science and Technology (JAMSTEC).

The d4PDF consists of a global experiment using MRI-AGCM3.2, the global atmospheric model of the Meteorological Research Institute with a horizontal resolution of 60 km, and a regional experiment using NHRCM, the regional climate model of the Meteorological Research Institute covering the Japanese region with a horizontal resolution of about 20 km.
The global experiment is divided into the following three types of ensemble experiments;

- Historical experiment: 1951 - August 2011 x 100 members,
- 4°C rise experiment 2051 - August 2111 x 90 members,
- 2°C rise experiment 2031 - August 2091 x 54 members.

The global models use the following parameters as the input data; the observed changes in sea surface temperature (SST), sea ice, greenhouse gas concentrations, sulfuric aerosol concentrations, ozone concentrations, and volcanic aerosol concentrations in the past experiments. 100 members start their calculations from different initial values and are also subjected to small perturbations of sea ice and sea surface temperature (SST).

The 4° C rise experiment simulates a 4° C increase in global mean temperature compared to the pre-industrial revolution (1850). Six SST future change patterns 1) CCSM4, 2) GFDL-CM4, 3) HadGEM2-AO, 4) MIROC5, 5) MPI-ESM-MR, 6) MRI-CGCM3, and 15 perturbations to each pattern were added for a total of 90 patterns based on the global atmosphere-ocean coupled model experiment. By giving the distribution, a total of 90 member ensemble experiments were conducted.

For the 2° C rise, we simulated a 2° C increase in global mean temperature compared to the pre-industrial revolution (1850); as in the 4° C rise experiment. Six different SST future change patterns and added 9 different perturbations are prepared to each pattern for a total of 54-member ensemble experiments.

In the domain model experiments, dynamical downscaling was performed from the following 60 km resolution global experiment to 20 km resolution.

- Past experiment September 1950 - August 2011 x 50 members,
- 4°C rise experiment September 2050 - August 2111 × 90 members,
- 2°C rise experiment September 2030 - August 2091 x 90 members.

In this experiment, five data components, e.g. global solar radiation, direct solar radiation, scattered solar radiation, temperature, and wind speed from the historical experiment, 4°C rise experiment, and 2°C rise experiment of the domain model NHRCM are extracted to estimate and analyze solar radiation for future climate.

METHODS

In this section, we discuss to compare data from d4PDF's past experiments to bring them closer to actual observed data, and how to correct for this.

The data from the d4PDF's past experiments are used to compare the observed data. This time, we extracted five data from d4PDF: global solar radiation, direct radiation, scattered solar radiation, temperature, and the U and V components of wind speed. The data are then compared with the observation data at Tateno, Tsukuba City in Ibaraki Prefecture at Japan. The data period is from January 1982 to August 2011, which is the overlap between the d4PDF past data and the observation data. Figures 1 to 4 in the next section show the comparison. The total solar radiation is the sum of direct and scattered solar radiation and is therefore omitted.

In order to compare the observed data with data from previous d4PDF experiments, the following calculations were performed for direct and scattered solar radiation.

$$\text{Average value of observed data} \,/\, \text{Average value of d4PDF} \quad (1)$$

The values for direct and scattered solar radiation were 0.72 and 1.27, respectively. For direct irradiation, the d4PDF values tend to be larger than the observed data. Conversely, for scattered irradiation, the d4PDF values tend to be smaller than the observed data.

RESULTS AND DISCUSSION

A comparison of the corrected d4PDF data with the observed data is shown below.

The correction method for direct and scattered solar radiation is to approach the observed data so that the cumulative frequency distribution of the d4PDF data fits every 10 W/m². Next, for temperature, the following formula is applied.

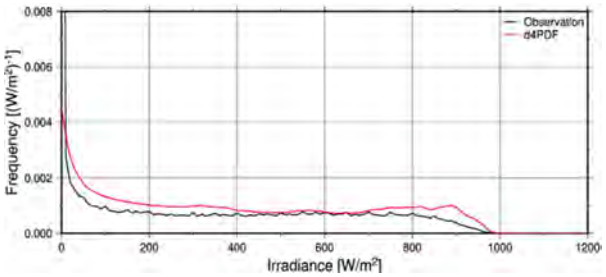

Fig. 1: Comparison of d4PDF and observed data for direct normal surface solar radiation

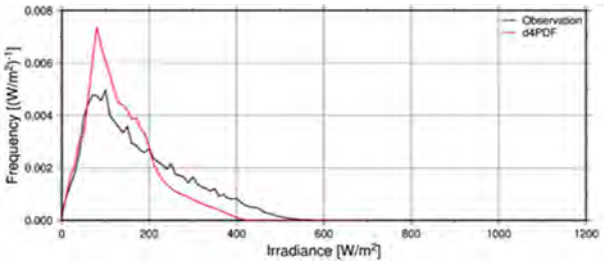

Fig.2: Comparison of d4PDF and observed data for scattered solar radiation

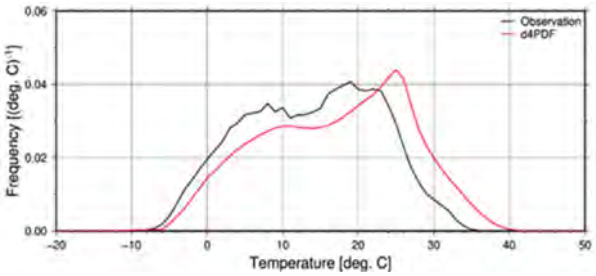

Fig.3: Comparison of d4PDF and observed data for temperature

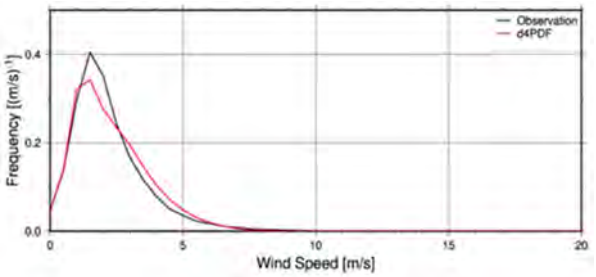

Fig.4: Comparison of d4PDF and observed data for wind speed

$$T_{Corrected} = 0.8887015946 \times T_{\mathrm{d4PDF}} - 1.296835973 \qquad (2)$$

Finally, the following method of correction in the U and V components of wind speed is used in the following equation.

$$u_{Corrected} = 0.94575 \times u_{\mathrm{d4PDF}} \qquad (3)$$

In order to compare the corrected d4PDF data from previous experiments with the observed data, the following calculations

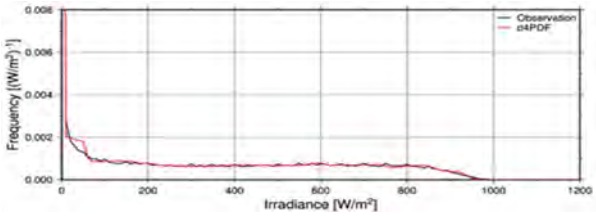

Fig. 5: Comparison of observed data and d4PDF data after correction for direct solar radiation on the normal surface

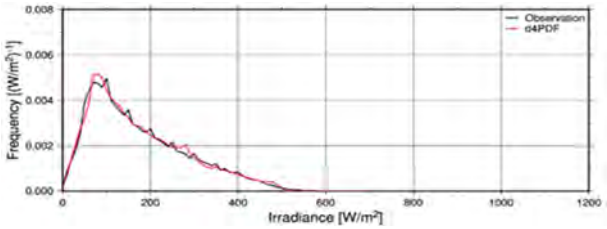

Fig. 6: Comparison of observed data and d4PDF after correction for scattered solar radiation

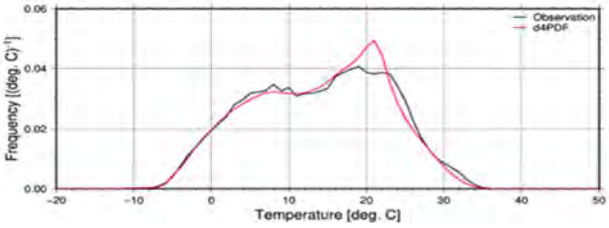

Fig. 7: Comparison of observed data and d4PDF after correction for temperature

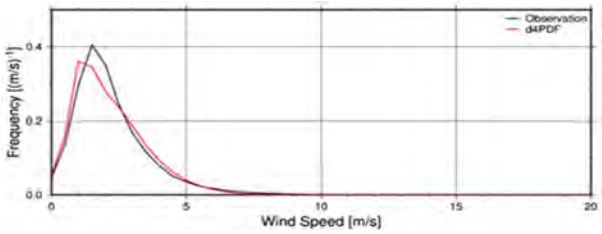

Fig. 8: Comparison of observed data and d4PDF after correction for wind speed

were performed for direct and scattered solar radiation.

Mean value of observed data／Mean value of corrected d4PDF (4)

In the case of direct solar radiation, the value was 0.99. In the case of scattered solar radiation, the accuracy was 1.00, which is considered to be considerably better. In the case of the U and V components of temperature and wind speed, the overall accuracy was sufficient due to the overlap between the observed data and the d4PDF. Therefore, this correction method is considered to be the best one to bring the d4PDF weather forecast data closer to the actual weather.

Therefore, there is no problem in using this correction method for the future climate data of the 4° C rise experiment and 2° C rise experiment for the central region and d4PDF.

Diagnosis of soil fertility by remote sensing data and GIS

Jieli Zhou[1] and Yongfen Wei[2]
1. **Graduate school of Natural Science and Technology, Gifu University, 1-1 Yanagido, Gifu 501-1193, Japan**
2. **River Basin Research Center, Gifu University, 1-1 Yanagido, Gifu 501-1193, Japan**

INTRODUCTION

Soil fertility is a measurement of the soil's ability to provide various nutrients needed for crop growth. Faced with the growing global demand for food due to the world population increase from 7.6 billion in 2020 to 9.6 billion in 2050, how to effectively assess soil fertility to maximize crop yields on limited arable land is a critical issue. The evaluation of arable land's soil fertility has mainly based on soil's physical and chemical properties, so far, in most cases, the evaluation is a small-scale-based approach and lacks quantitative and visualized strategies. The main purpose of this study is to use remote sensing data, GIS, field investigation data and laboratory analysis results of soil samples to comprehensively quantify and visualize the soil fertility of agricultural soil.

Study area

Kaizu City as shown in Fig. 1, located in the southernmost of Gifu Prefecture, was used as study area in this research. It has an area of about 112 square kilometers. The arable land accounts for about 37% of its total area. The main crops of rice, wheat and soybeans are cultivated in rotation. In this study, wheat was used as the research object to analyze soil fertility.

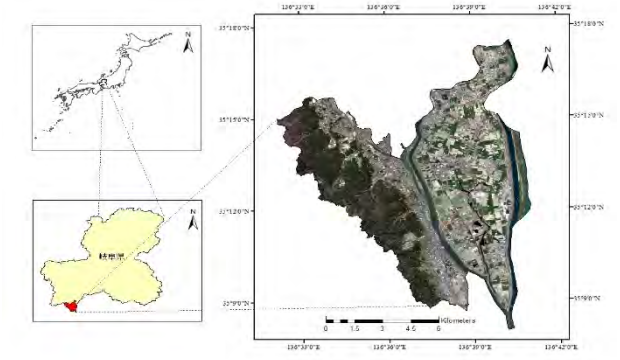

Fig. 1 Study area (Satellite image on April 15, 2022)

Research flowchart

This study was carried out according to the following flowchart.

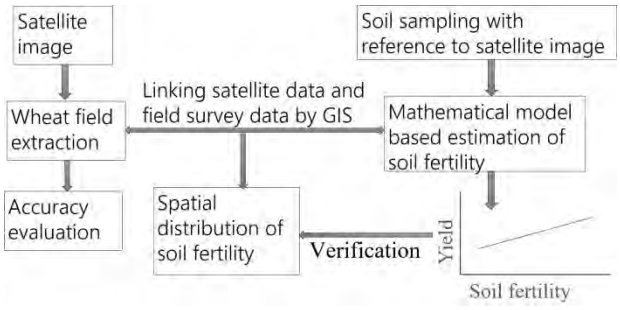

DATA AND METHODS

– Data

The following data were used in this study.

Satellite data

Sentinel-2 provides global 10-meter resolution multispectral images every 5 days. Besides, since it has a red edge band, which is more sensitive to vegetation information, therefore, it is widely used for mapping changes in land cover and monitoring the world's forests. In this study, Sentinel-2 satellite data obtained on the Copernicus Open Access Hub website were used.

Soil sampling

Field investigations were conducted after wheat harvest to avoid the effect of fertilization on soil fertility during wheat growth. And soil sampling was conducted from 5 blocks shown in Fig. 2 (No. 1- 5). In block No.1, four 10 × 10 m plots were selected for soil sampling, and three 10 × 10 m plots were selected in block No. 2- 5. For each plot, five samples were collected. Totally, 80 samples were collected from surface soil depths of 0-15 cm. The location of each soil sampling point was recorded using a handheld GPS.

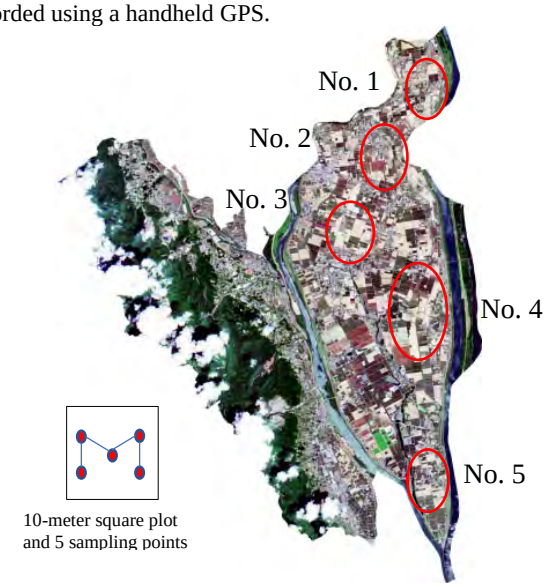

Fig. 2 Five blocks for soil sampling

—Method

Image-based wheat area extraction

Decision tree classification method was used to extract wheat area based on NDVI (Normalized Difference Vegetation Index) value and texture of the image. NDVI images of each month in the growing period of wheat were produced to improve the extraction accuracy (Fig. 3).

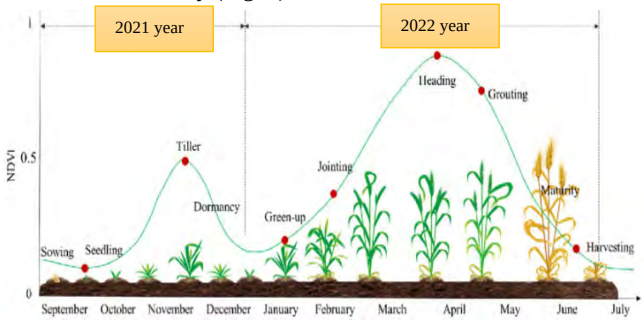

Fig. 3 Variation trend of NDVI in wheat growth period

The distribution map obtained was shown in Fig.4. According to the field investigation results, extraction accuracy of wheat area was 98%.

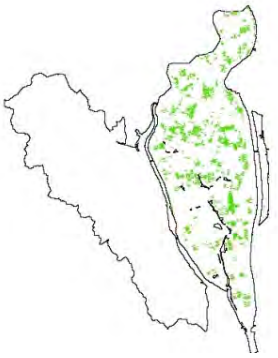

Fig. 4 Extracted wheat area

Sample measurement

For freeze-drying, 20g of soil was taken from each sample, and then stored in a -20°C freezer. The freeze-dried soil was used for DNA extraction and enzyme activity detection. The remaining soil is naturally air-dried and stored at room temperature for measuring soil physical and chemical properties affecting soil fertility, such as soil pH, soil organic matter (SOM), electrical conductivity (EC), organic carbon (OC), total nitrogen and so on. So far, parameters of soil moisture, soil pH, EC, DNA extraction, and dehydrogenase activity (DHA) have been measured.

Soil fertility index

Soil fertility index (SFI) proposed by Tülay Tunçay et al. (2021) was used to estimate agricultural soil fertility (Eq. (1).

$$SFI = [Rmax * \sqrt{\frac{A}{100} \times \frac{B}{100} \times \dots \dots \frac{X}{100}}] \quad (1)$$

In this equation, A, B …X mean rating values for different soil parameters of soil physical and chemical properties, which was graded into 5 different levels from 100 to 10. Rmax is a ratio of (A + B+ ·····+X) to total numbers of soil parameter used.

SFI was reported to be effective for quantifying the spatial distribution of soil fertility. However, biological parameters were not considered. This study also took into account biological influence factors such as DNA and DHA.

RESULTS AND DISCUSSION

Fig. 5 indicated the distribution of SOM, EC, DNA (16S rDNA), NDVI, DHA and soil moisture. These maps produced according to Kriging interpolation, a geostatistical interpolation method that considers both the distance and the degree of variation between known data points when estimating values in unknown areas. Observing Fig. 5, we can find that these parameters were relatively high in the central part of Kaizu City, but relatively low at the lower ends of Kaizu City. Especially in the vicinity of the third block, the values of these parameters were generally the highest.

NDVI is an index that reflects the growth and health of vegetation. From both two figures of SOM and NDVI, it can be seen that the distribution of high and low values is roughly the same, indicating that SOM and NDVI are highly correlated.

From the distribution map of dehydrogenase activity (DHA) and moisture, it can be seen that the dehydrogenase activity and the moisture are most active near the third block. Based on these maps, it can be roughly estimated that the soil fertility in the third block is the highest, while in the southernmost part of Kaizu City has the lowest soil fertility, and the soil fertility in the bloke No. 2 and No. 4 is almost at a medium level.

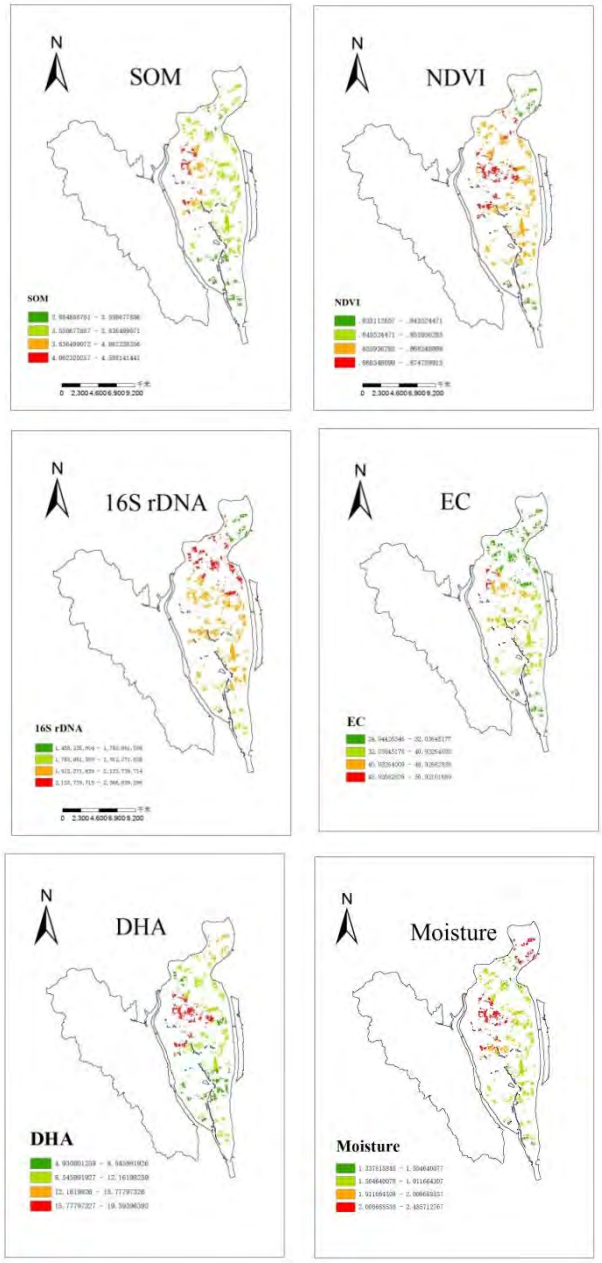

Fig. 5 Distribution map of soil parameters

The final objective of this study is to quantify and visualize soil fertility in agricultural soil using remote sensing data, GIS, field survey data and laboratory analysis results of soil samples. So far, the extraction of wheat has been completed, and the distribution of some soil parameters also clarified. However, to realize the quantitative and visual evaluation of soil fertility, the measurement results of other soil parameters are still needed. At the same time, finding the relationship between soil fertility and crop yield is also of great importance for validating and improving soil fertility.

REFERENCES

Tülay Tunçay et al, Assessing soil fertility index based on remote sensing and GIS techniques with field validation in a semiarid agricultural ecosystem. Journal of Arid Environments. Volume 190, 2021.

Potential hosts and transfer of As, Cr, and Pb-induced resistance genes in soil under coal mining disturbance

Yajie Wang[1] and Fusheng Li[1,2]

1. **Graduate School of Engineering, 1-1 Yanagido, Gifu 501-1193, Japan**
2. **River Basin Research Center, Gifu University, 1-1 Yanagido, Gifu 501-1193, Japan**

INTRODUCTION

Coal continues to be a major global primary energy (Arratia-Solar, 2019), and the concerns about the impacts of coal production on the environment have been intensifying due to the considerable growth in coal consumption in recent years. Heavy metals including chromium (Cr), cadmium (Cd), nickel (Ni), copper (Cu), zinc (Zn), arsenic (As), and lead (Pb) are possible to be released during coal production with dust and wastewater. Heavy metal contaminations in soil seriously threaten the safety of soil ecology due to their high toxicity, non-biodegradability, and accumulative property. Bacteria as the most abundant organism in soil are sensitive to the contents of heavy metals. Long-term stress from these elements promotes the soil bacterial species with strong resistance to grow as dominating ones after adapting to their toxicity. The metal resistance genes (MRGs), *arsB*, *chrB*, and *pbrT*, are the genetic basis for bacteria adaption under stress from As, Cr and Pb, respectively. The investigation on the potential host of *arsB*, *chrB*, and *pbrT* and their transfer will provide information for an in-depth understanding of the mechanism behind the adaption of bacteria to the stress from Cr, As, and Pb. The aim was to identify the potential host bacteria of As, Cr, and Pb-induced resistance genes and clarify the transfer of the genes in soil under the disturbance of coal mining for better management of coal production.

MATERIALS AND METHODS

Six coal mines in Luliang, Shanxi Province of China with different scale (M1: 0.6, M2: 1.2, M3: 1.5, M4: 1.8, M5:3.0, M6: 8.0 × 10^6 t) were selected for study. In each mine, surface soil (1-5cm) was collected from three different sites (0, 1, and 3km apart from center of the mine). Organic matter (OM), total nitrogen (TN), total phosphorus (TP), and seven heavy metal elements (Cr, Ni, Cu, Zn, As, Cd, and Pb) were measured.

The potential ecological risk index (*RI*) was used to assess the ecological risk of heavy metals in coal mine soil. The formulas are as follows:

$$RI = \sum_{i=1}^{n} E_{r,i} = \sum_{i=1}^{n} (T_{r,i} \times C_{f,i})$$

$$C_{f,i} = C_{D,i} / C_{R,i}$$

where, n is the number of heavy metals, E_r is the potential ecological risk of single heavy metal, T_r is the heavy metal toxic response factor (Xiang et al., 2022), C_f is the single heavy metal pollution index, C_D is the measured heavy metal concentration, and C_R is the geochemical background value.

The abundance of MRGs (*arsB*, *pbrT*, and *chrB*), Mobile Gene (*intl1*), and total bacterial (*16S rDNA*) were measured through quantitative real-time PCR (qPCR). For comparation, the abundance of antibiotic resistance gene (AGRs: *tetG*, *tetM*, and *sul1*) were also measured. The bacterial community structure was analyzed through high-throughput sequencing technology. The relations between the potential ecological risk of heavy metals and the abundance of *arsB*, *chrB*, and *pbrT* were examined by spearman correlation analysis using "psych" packages in R (version 4.0.3) and redundancy analysis (RDA) using "vegan" packages in R (version 4.0.3). The potential host bacteria at species level were obtained through the co-occurrence analysis drawn using Gephi 0.9.2 based on R language correlation analysis ($p < 0.01$).

RESULTS

The concentration of heavy metals in soil of different coal mines showed variations. The statistical analysis results based on the concentrations of heavy metals and basic physiochemical properties of the soils reflected by pH, EC, moisture, total phosphorus (TP), total nitrogen (TN), and organic matter (OM) will be shown in the presentation. The potential ecological risk of single heavy metal was shown in **Table 1,** which varied in the range of 0.3-82.5. Cd was the major contaminant.

In total, 963 bacterial species were identified from soil samples. The top 20 species displayed according to the magnitude of the relative abundance were chosen for the histogram analysis (**Fig. 1**). *Pseudomonas_sp_108Z1* belonging to Proteobacteria dominates in M1, and the corresponding relative abundance was significantly higher than that in other mines.

The absolute abundance of MRGs, ARGs, *intl1* and *16S rDNA* in soil of the six coal mines was shown in **Fig. 2**. The abundance of MRGs in M2-M5 was higher than that of ARGs. *arsB* was the most abundant metal resistance gene (**Fig. 3**).

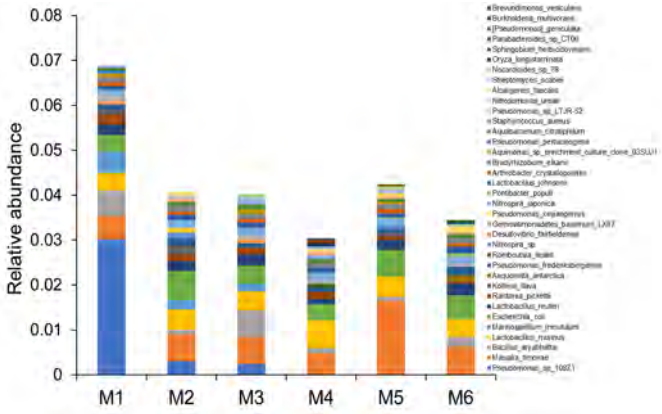

Fig. 1 Bacterial community for the top 20 dominant taxa at species level in soil of the coal mines (M1-M6).

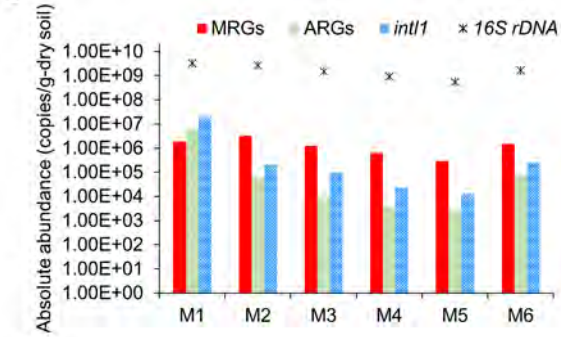

Fig. 2 Absolute abundance of MRGs, ARGs, *intl 1* and *16S rDNA* in soil of the coal mines (M1-M6).

Based on the data of the six coal mines, eight potential host bacteria of *arsB* and *pbrT*, two poential host bacteria of *chrB* were identified (**Fig. 4**). The potential host bacteria of MRGs in M1 were different from M2-M5. The potential host bacteria of MRGs in the soil 0, 1, and 3km apart from the center of the mine showed variations. The relevant results will be shown in the presentation. The MRGs (*arsB*, *pbrT*, *chrB*) and ARGs (*tetG*, *tetM*, *sul1*) were categorized into different classes.

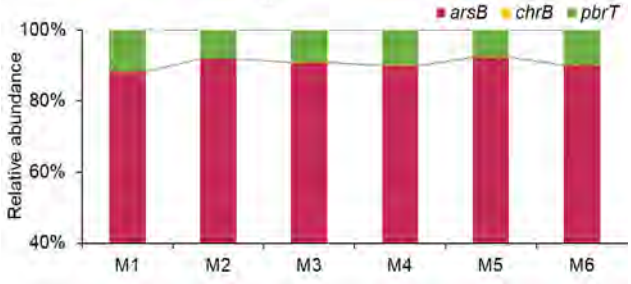

Fig. 3 Relative abundance of MRGs (*arsB*, *chrB* and *pbrT*) in soil of the coal mines (M1-M6).

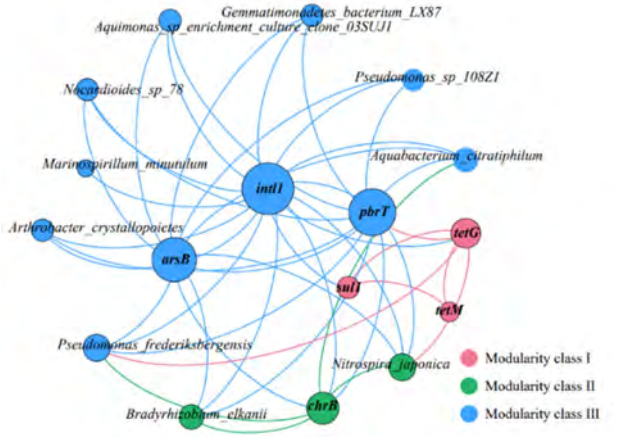

Fig. 4 Potential host bacteria of MRGs (*arsB*, *pbrT*, and *chrB*), ARGs (*tetG*, *tetM*, and *sul1*), and Mobile Gene (*intl1*) in soil of the coal mines.

The potential ecological risk of heavy metals in coal mine soil showed negative correlations with the abundance of MRGs (**Fig. 5**). The abundance of MRGs positively correlated with that of the total bacteria (*16S rDNA*), and mobile gene (*intl1*). Cd, Cr and Zn significantly and negatively correlated with the abundance of *16S rDNA* and *intl1* (relevant results will be shown in presentation).

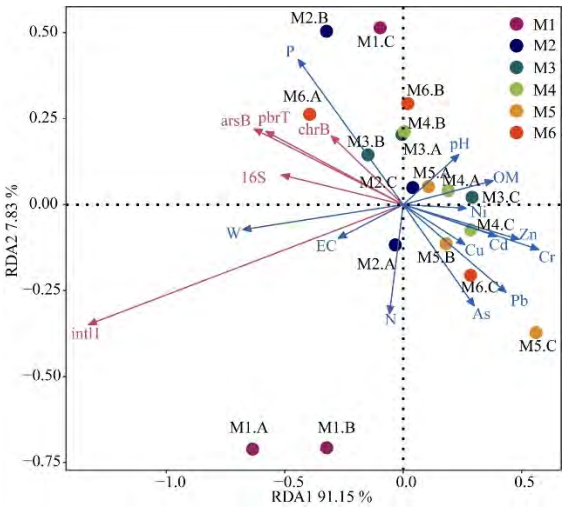

Fig. 5 Effect of potential ecological risk of heavy metals on the distribution of MRGs, *16S rDNA* and *intl1* in soil of the coal mines. P: total phosphorus; W: water content; N: total nitrogen; OM: organic matter; 16S: 16S rDNA. As, Cr, Pb, Ni, Cu, Zn, and Cd represent the corresponding potential ecological risk index.

CONCLUSION

This study identified the potential host bacteria and explored the transfer of MRGs (*arsB*, *chrB*, and *pbrT*) in coal mine soils. The potential host bacteria in M1 were different from M2-M5. The potential host bacteria showed variations in the soil 0, 1, and 3km apart from the center of the mines. The variations of potential host bacteria may be due to the different bacterial compositions. The abundance of MRGs was closely related to that of the total bacteria (*16S rDNA*), and mobile gene (*intl1*), which is negatively associated with heavy metals. Heavy metals may control the spreading of MRGs by inhibiting their vertical and horizontal transfer.

【Reference】

Arratia-Solar, A., 2019. Help curtail new coal mines. Nature 567, 175.

Xiang, Q., Yu, H., Chu, H., Hu, M., Xu, T., Xu, X., He, Z., 2022. The potential ecological risk assessment of soil heavy metals using self-organizing map. Science of The Total Environment, 843, 156978.

Table 1 The mean values of potential ecological risk of heavy metals in soil of the coal mines (M1-M6).

Coal mine	M1	M2	M3	M4	M5	M6	Average M1-M6	Average contribution (%)
As	3.73	3.23	3.51	4.50	5.57	3.28	3.97	7.1
Cr	1.17	1.02	1.42	1.36	1.56	1.10	1.27	2.3
Pb	3.24	2.67	3.88	3.35	3.46	3.00	3.26	5.9
Ni	4.28	3.63	4.23	5.06	4.66	3.97	4.31	7.7
Cu	3.31	3.41	3.70	3.44	3.77	3.02	3.44	6.2
Zn	0.52	0.44	0.66	0.51	0.58	0.52	0.54	0.9
Cd	36.72	32.01	53.56	38.47	37.58	35.40	38.95	69.9
Overall risk (RI)	52.98	46.41	70.96	56.68	57.17	50.28	55.75	-

Can activated carbon allow antibiotic resistance genes to access into its pores

Sri Anggreini[1] and Fusheng Li[2]
1. **Graduate School of Engineering, Gifu University, 1-1 Yanagido, Gifu 501-1193, Japan**
2. **River Basin Research Center, Gifu University, 1-1 Yanagido, Gifu 501-1193, Japan**

INTRODUCTION

The emergence and proliferation of antibiotic resistance genes (ARGs) in the environment have become a global health issue. Nowadays, antibiotic resistance causes 700,000 deaths globally each year (O'Neill. 2016). The existence of ARGs has been confirmed in drinking water sources and tap water, which threaten human health. Activated carbon (AC) adsorption is used in drinking water treatment for removal of trace organic compounds. ARG may enter the pore of AC depending on the pore size and surface properties of AC. However, little is known about the access possibility of ARG into the pores of AC. Previous studies reported that granular AC adsorbers increased the abundance of ARGs due to the enrichment of ARGs in the biofilm (Su et al. 2018). Detailed information on the fate and behavior of ARG during contact with AC is still limited. The objective of this study was to investigate the possible access of ARGs into the pore of AC. For this purpose, the tetracycline resistance gene (*tetG*) was selected as a target gene and ten types of commercially available ACs with different pore size distributions were used in this study.

MATERIALS AND METHODS

Activated carbon – Ten commercially available ACs were used, namely carbon A, B, C, D, E, F, G, H, I, and J. The physicochemical properties of ten types of AC are displayed in **Table 1**. The surface morphology and elemental composition of AC were observed by scanning electron microscopy (SEM) and energy dispersive X-ray analyzer (EDX). The charge characteristics of AC were evaluated by the pH of point of zero charges (pH_{PZC}). The BET pore distribution was determined from the nitrogen adsorption technique using the Micromeritics 3Flex instrument. The functional groups present on the surface of ACs were investigated by Fourier transform infrared spectroscopy (FTIR).

Table 1. Physicochemical properties of different types of AC

Type	Origin	Surface area (m^2/g)	Total pore volume (cm^3/g)	pH_{pzc}
A	Coal-based	956	0.69	6.3
B	Coal-based	745	0.28	6.4
C	Coconut shell-based	1322	0.66	7.2
D	Coal-based	820	0.44	6.5
E	Coal-based	856	0.55	6.8
F	Wood-based	1,290	1.64	5.1
G	Wood-based	866	0.37	7.6
H	Coconut shell-based	1238	0.59	7.5
I	Coal-based	775	0.48	7.8
J	Wood-based	1,053	0.62	8.45

Amplicon solutions containing target genes – The amplicon solution of *tetG* was prepared by referring to the TA cloning method (Takara, Japan). The *E. coli* DH5α containing plasmid pMD20 which carries target genes (*tetG*) was used in this study. After TA cloning, the confirmed colonies containing the desired plasmid were cultured overnight with LB medium and ampicillin. Plasmid pMD20 was extracted from *E. coli* DH5α using a plasmid extraction kit (MACHEREY-NAGEL, Germany). Non-quantitative PCR (LifePro, China) was performed to amplify the target gene. A designed primer was used to amplify *tetG* with the amplification products at 133 bp (45.22 nm). The amplification product was isolated by gel electrophoresis and purified using a Gel and PCR Clean-up kit. The purified amplification product was diluted with sterile deionized water to obtain the amplicon solution.

Contact experiments of ARG with AC – Contact experiments were conducted in 5 mL vials at room temperature. The amplicon solution containing only *tetG* was applied as the blank control. The AC dose was set as 1 g/L. After 180 minutes of shaking, centrifugation was conducted for 10 minutes at 12,000g to separate AC particles. The obtained supernatant was subjected to ARG quantification. The concentration of ARGs before and after contact with AC was determined by qPCR. The pseudo-first and pseudo-second-order kinetic models described below were used to analyze the data from the experiments.

$$\frac{dq_t}{dt} = k_1(q_e - q_t) \qquad (1)$$

$$\frac{dq_t}{dt} = k_2(q_e - q_t)^2 \qquad (2)$$

where q_t (copies/mg) is ARG adsorbed onto AC at time t, q_e (copies/mg) is adsorption capacity at equilibrium, k_1 and k_2 (copies.min/mg) are the pseudo-first and pseudo-second-order rate constant, respectively.

RESULTS AND DISCUSSION

The residual concentrations of *tetG* during contact with various types of AC are shown in **Fig. 1**. Most ACs showed low residual concentrations except carbon-B. The lower residual concentration of *tetG* can be attributed to the pore size, pore volume, and surface chemistry of AC. The size of *tetG* is 2.2–2.6 nm in width and 45.22 nm in length. *TetG* probably can enter the pore of AC by stretching into an elongated form and fixed into the active site of AC. However, carbon-B possessed more pores in the size region between 0-1.5 nm as displayed in **Fig 2**. The lowest reduction of *tetG* was obtained from carbon-B (0.75 log reduction). The size exclusion effect probably prevented *tetG* from entering the pores of carbon-B which has more pores with sizes less than 1.5 nm.

Model analysis indicated that the pseudo-second-order kinetic model fitted all experimental data much better than the pseudo-first-order ones. The average correlation coefficient (R^2) of pseudo-first and pseudo-second-order were 0.5722 and

0.9975, respectively. The estimated value of q_e as shown in **Fig. 3** agreed well with the experimental ones. The q_e values followed the order F > I > J > G > C > B > H > A > E > D, indicating wood-based ACs had higher capability to accept ARG than coal-based ACs.

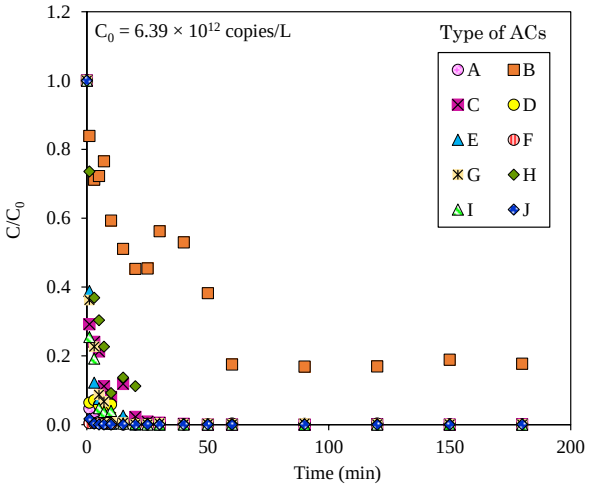

Fig. 1 Residual concentrations of *tetG* during contact with different types of AC.

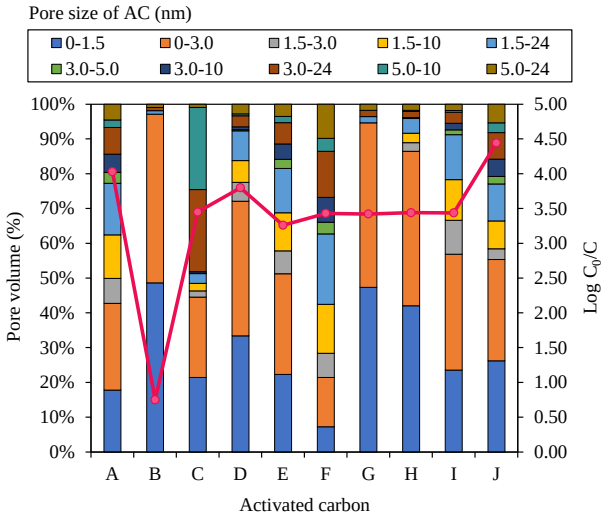

Fig. 2 Relationship between pore size distribution of AC with reduction of *tetG* after contact at 180 minutes.

The correlation coefficients of q_e with the properties of AC are summarized in **Table 2**. The correlation analysis using 10 types of AC indicated that q_e has a good correlation with pore volume in the specific size region of AC. When ACs were classified based on their raw materials, the R^2 of q_e become bigger in wood-based ACs. It was indicated that q_e was significantly influenced by the raw material of ACs. This result is consistent with the adsorption capacity changes mentioned previously. A good positive correlation of q_e from ten types of AC and wood-based ACs is noticed with the pore size regions of 3-5 and 3-10 nm. The negative correlation of q_e was found in the size region between 5-10 nm. This is related to the attraction force between *tetG* and active site of AC. *TetG* that has entered the external pores of AC will diffuse through the big and small internal pores. Smaller internal pores have a greater attraction force compared to bigger ones. Therefore, the pore size region between 3-5 nm was more effective for admission of *tetG*.

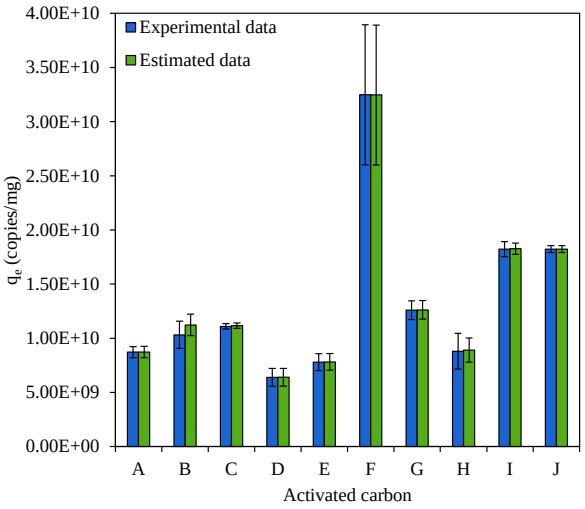

Fig. 3 Adsorption capacity of *tetG* on different types of AC.

Table 2. Correlation of model-estimated q_e with the pore volume of specific size regions, surface area, total pore volume, and pH_{PZC} of ACs.

Pore size (nm)	Linear correlation coefficient		
	10 ACs	5 Coal-based ACs	5 Wood-based ACs
0-1.5	-0.666	-0.052	-0.977
0-3.0	-0.743	0.307	-0.989
1.5-3.0	0.417	0.342	0.917
1.5-10	0.572	0.122	0.966
1.5-24	0.666	0.052	0.977
3.0-5.0	0.574	-0.136	0.981
3.0-10	0.652	-0.234	0.973
3.0-24	0.251	-0.307	0.142
5.0-10	-0.007	-0.376	-0.202
5.0-24	0.790	-0.448	0.990
Surface area	0.380	-0.480	0.217
Total pore volume	-0.213	-0.189	0.911
pH_{PZC}	-0.290	0.837	-0.744

CONCLUSIONS

The access possibility of ARG into different types of AC was investigated. AC has a big capacity to admit ARG to enter the pore and fixed inside the pores. *TetG* may enter the pore of AC by extending into an elongated shape. Wood-based ACs had a higher capability to accept ARG than coal-based ACs.

REFERENCES

O'Neill, J., 2016. Tackling drug-resistant infections globally: final report and recommendations, The Review on Antimicrobial Resistance (London, UK).

Su, H.C., Liu, Y., Pan, C., Chen, J., He, L., Ying, G. 2018. Persistence of antibiotic resistance genes and bacterial community changes in drinking water treatment system: From drinking water source to tap water. *Science of the Total Environment*. 616–617, 453–46.

Improvement of membrane filtration performance by pre-coating with powdered activated carbon

Wenqing Li [1] and Fusheng Li [2]

1. **Graduate School of Natural Science and Technology, Gifu University, 1-1 Yanagido, Gifu 501-1193, Japan**
2. **River Basin Research Center, Gifu University, 1-1 Yanagido, Gifu 501-1193, Japan**

INTRODUCTION

Membrane filtration is a new technology being increasingly considered as an alternative to conventional sand filtration for drinking water production. Membrane fouling is an important factor that limits its application to most surface water sources (including rivers, lakes and reservoirs). Membrane fouling refers especially to biofouling and fouling by dissolved organic substances, with the latter being occurring in almost all cases where membrane filtration is applied to treat surface water which contains, to different extents, naturally occurring organic matter (NOM), a mixture of organic components with different physicochemical properties. Powdered activated carbon (PAC) can remove dissolved organic matter through adsorption and is thus considered effective to alleviate membrane fouling when used as a pretreatment prior to membrane filtration. However, this method has the shortages: one is related to the adsorption life of PAC and the other one is related to the filtration resistance from the mixed cake layer formed on membrane surface by the added PAC and the originally exited suspended particles in water.

In this study, membrane filtration using membrane pre-coated with PAC is investigated. Pre-coating with PAC is considered to enable the formation of a thin barrier layer for contact adsorption of NOM and for inhibiting the direct contact of suspended particles in water with the membrane surface. The investigation is focused on evaluation of the effects on membrane fouling and dissolved organic matter removal, for which, membrane filtration experiments are conducted using membranes with different pore sizes and PAC with different particle sizes and coated thicknesses.

MATERIALS AND METHODS

Nagara River water filtered through 0.2 μm membrane was used as the water for study. A series of batch membrane filtration experiments are planned by filtering the water with 0.1 μm hydrophilic PVDF membrane (effective filtration area of 10.7cm^2). Three PAC types are compared: W-PAC (wood-based), S-PAC (wood-based) and CB-PAC (coconut shell-based); and, each PAC type is categorized into three fractions with different particle size ranges through sieving: 22-44 μm, 44-63 μm and 63-88 μm. The thickness of pre-coated PAC on the membrane surface is varied by the total weight of PAC loaded through filtration of designated amounts of PAC solution prepared using pure water through the membrane: 0 mg/10.7cm^2, 6.45 mg/10.7cm^2, 12.9 mg/10.7cm^2, 25.8 mg/10.7cm^2.

The images of Scanning Electron Microscope (SEM) for non-pre-coated and pre-coated membrane are showed in **Fig. 1**. The extent of the fouling of membrane is evaluated by the flux over the filtration process and the images of SEM. The filtration flux, J ($m^3 \cdot m^{-2} \cdot h^{-1}$), is computed based on the following equation,

$$J = \frac{\Delta V}{A \cdot \Delta T} \quad (1)$$

where, ΔV is the accumulative volume of water filtered within the filtration time length of ΔT, A is the membrane surface area. The adsorption performance of the pre-coated
PAC is evaluated based on the measurements for dissolver organic carbon (DOC), UV absorbance at 260 nm (UV260), fluorescence excitation-emission matrix (EEM) and molecular weight distribution (MW) for water before and after treatment.

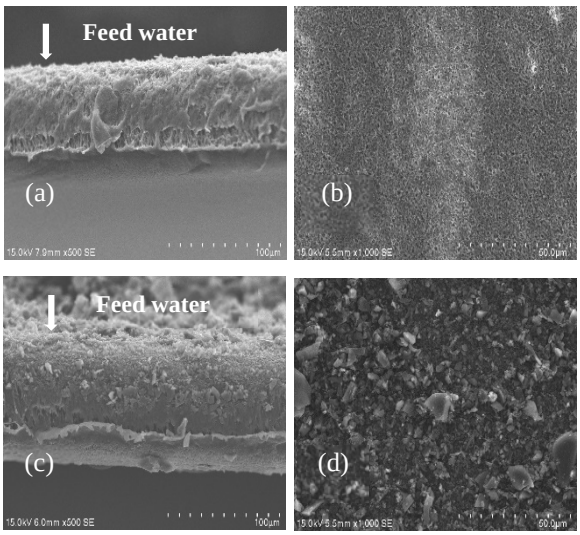

Fig. 1. SEM images of membrane: a and b are the cut section and surface of membrane before pre-coating; c and d are the cut section and surface of membrane after pre-coating of PAC (25.8mg/10.7cm^2)

RESULTS AND DISSCUTION

The results on the changes of filtration flux for the membrane filtration experiment conducted with pre-coated PAC with the size of 22-44 μm for the PAC type of W-PAC are shown in **Fig. 2**. It can be seen from the figure that compared to the experiment without PAC pre-

coating, the experiments with PAC pre-coating resulted in flux decline, with the extent of decline being more significant for the two experiments with the smaller thickness of PAC (6.45 mg/10.7cm^2 and 12.9 mg/10.7cm^2).

The concentrations of dissolved organic matter in the water after treatment reflected by UV260 are shown in **Fig. 3**. UV260 decreases significantly at the beginning, and then increase gradually with the increases of the filtered water volume. The larger the thickness of pre-coated PAC, the lower the value of UV260. This may indicate that pre-coating PAC can improve the filtered water quality, therefore reduce the existence of humic substances that could cause membrane fouling, but at the same time the carbon layer itself causes membrane filtration resistance.

The results of dissolved organic matter reflected by TOC are shown in **Fig. 4**. It can be seen from the figure that with the increase of the thickness of PAC pre-coated, TOC in the filtered water decreases more obviously, and then similar to the profile of UV260, TOC increases with the increases of filtered water volume. This also indicates the effect of PAC pre-coating on the filtered water quality and membrane filtration resistance development.

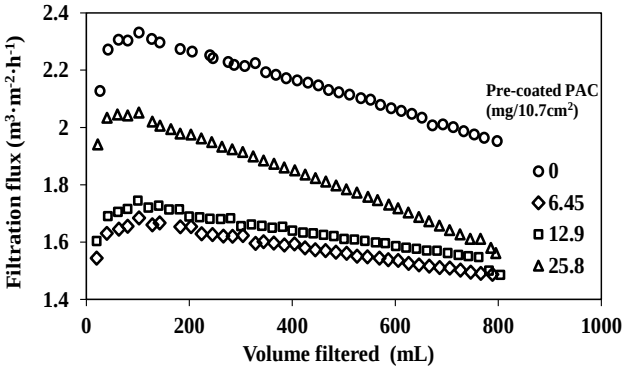

Fig. 2. Changes in filtration flux with the increase of cumulative filtration volume.

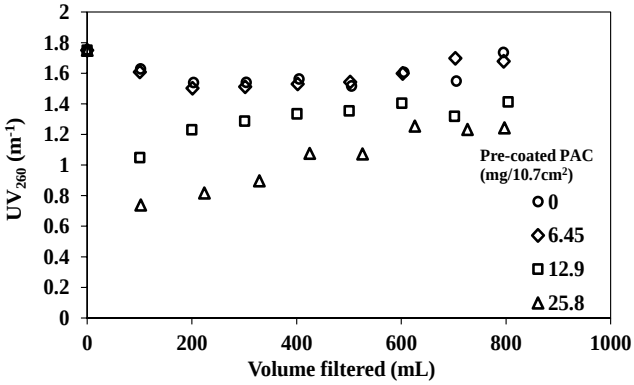

Fig. 3. Changes in UV260 with the increase of cumulative filtration volume.

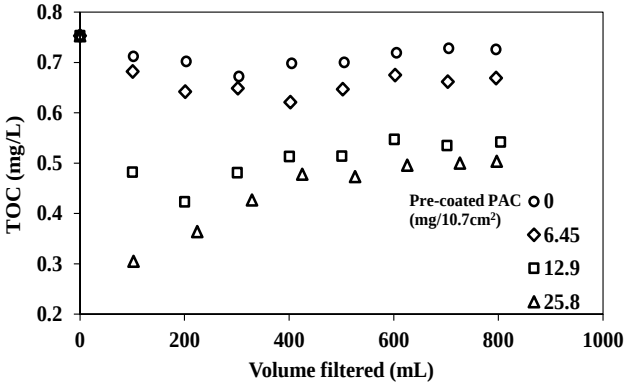

Fig. 4. Changes in TOC with the increase of cumulative filtration volume.

SEM images of membrane with precoated PAC (25.8mg/10.7cm^2) after filtration process are showed in **Fig. 5**.

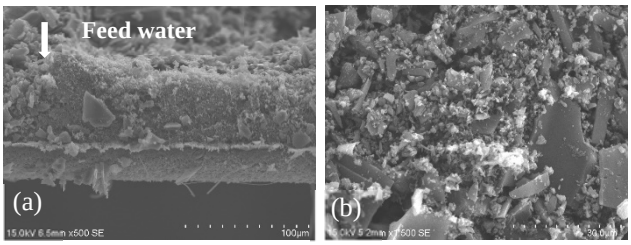

Fig. 5. SEM images of membrane with precoated PAC (25.8mg/10.7cm^2) after filtration process: a is the cut section of membrane; b is the surface of membrane

CONCLUSION

The pre-coating PAC can reduce the existence of humic substances that could cause membrane fouling through adsorption, and improve the filtered water quality. However, the carbon layer itself caused membrane filtration resistance. Of the three tested layer thickness, the largest one revealed the smallest membrane filtration resistance, suggesting the existence of optimal pre-coating condition, which will be investigated.

REFERENCES

Amaral, Pauline, et al. “Superfine Powdered Activated Carbon (S-PAC) Coatings on Microfiltration Membranes: Effects of Milling Time on Contaminant Removal and Flux.” Water Research, vol. 100, pp. 429–438, 2016,

Zhang Li, Graham Nigel, et al. “Targeting membrane fouling with low dose oxidant in drinking water treatment: Beneficial effect and biological mechanism.” Water Research, Vol.209, pp.73-78, 2022 Light in a Stratified Water Column. American Naturalist 174:190-203.

Effect of bacteria on *Uroglena sp*. growth in surface water

Ramayandi[1], Sarkar Kanika[1], Nurul Syuhada Abdul Latif[2] and Fusheng Li[3]
1. **Graduate School of Engineering, Gifu University, 1-1 Yanagido, Gifu 501-1193, Japan**
2. **Faculty of Engineering, Gifu University, 1-1 Yanagido, Gifu 501-1193, Japan**
3. **River Basin Research Centre, 1-1 Yanagido, Gifu 501-1193, Japan**

INTRODUCTION

Uroglena sp. (golden algae) is a free-swimming, colonial microalgae species whose individual cells are connected by a system of dichotomously branched structures (cytoplasmic threads or gelatinous stalks) radiating from the center of the colony. The presence of *Uroglena sp*. leads to a fishy odor in the water source, and the specific compounds that cause the fishy odor in *Uroglena* have been identified as 2,4-heptandienal, 2,4-decadienal, and 2,4,7-decatrienal.

The heaviest blooms of *Uroglena sp*. occur in spring (April to May). *Uroglena sp.* blooms are unpredictable because of the interaction of many different factors, including water temperature, salinity, flushing rate, turbulence, light, predation, and interspecies competitions and inhibitions.

Bacteria and microalgae are ubiquitous and abundant microorganisms in aquatic environments. Many studies have shown their influence on each other, both stimulative and inhibitory. Knowing the stimulative and inhibitory effects of bacteria for *Uroglena sp.* is very important in monitoring the growth of this microalgae. Therefore, the objective of this research is to investigate the effect of bacteria on *Uroglena sp.* growth in surface water.

MATERIALS AND METHODS

Surface water

The surface water sample was collected from a natural reservoir-a water source for drinking water treatment. It was collected in May and September, using a Kemmerer sampler from the surface of the pond (up to 1 meter in depth).

Incubation experiment

The water sample was divided and placed into 1 L Borosilicate glass reactors, and incubated at temperatures of 5, 10, 15, 20, and 30 °C for 30 days, respectively. The incubation was duplicated for all temperatures. Incubators (FCI-280GHS) with white fluorescent lamps were used. Samples (each for about 100 mL) during incubation were collected from each reactor at designated time points within the incubation period.

Analytical methods

The parameters measured include pH, electrical conductivity (EC), dissolved oxygen (DO), oxidation-reduction potential (ORP), microalgae, total bacteria (16SrDNA), dissolved nitrogen (DN), dissolved phosphorus (DP), dissolved organic carbon (DOC), and UV_{260}.

Total bacteria were measured by filtering 50 ml of the culturing sample using a 0.2 µm polytetrafluoroethylene (PTFE). Filters containing bacteria were isolated for their microbial genomic DNA using the DNaeasy PowerSoil Pro kit. All the extracted DNA samples were analyzed by Quantitative PCR (qPCR).

Furthermore, the number of microalgae was calculated under an inverted microscope of brand OLYMPUS BX53 by placing a sample (1 ml) into a Sedgewick rafter cell chamber.

The remaining cultured sample was filtered through a cellulose acetate membrane with a pore size of 0.2 µm for the subsequent analysis of DOC, DN, DP, and UV_{260}.

RESULTS AND DISCUSSIONS

Growth of *Uroglena sp.* in water samples of May and September

The initial number of *Uroglena sp.* in the May and September samples were 146 cells/mL and 5 cells/mL, respectively. The number of *Uroglena sp.* then increased after incubation. The peak growth of *Uroglena sp.* in both samples were different at each temperature where the highest growth was recorded at the temperature of 5 ˚C. The increase in temperature reduced the growth of *Uroglena sp.* and caused it to lyse faster.

Figure 1 shows the *Uroglena sp.* number during the incubation time for the May, and September samples respectively. For both samples, at the beginning of incubation, Uroglena sp. growth rose higher at temperatures of 10-20˚C. At 5˚C of incubation, *Uroglena sp.* in the May sample survived up until the 24th day then disappear completely. This is different with the September sample where it grew up until 1 month with the number still being high on the last day of incubation. However, at 30˚C, *Uroglena sp.* did not grow at all during incubation for May sample and grew only for 3 days for the September sample.

The results of this study indicate that *Uroglena sp.* in the September sample can grow longer than *Uroglena sp.* in the May sample. This is because the ratio of the number of *Uroglena sp.* and other microalgae in the May sample is higher, causing faster nutrient uptake compared to the September sample.

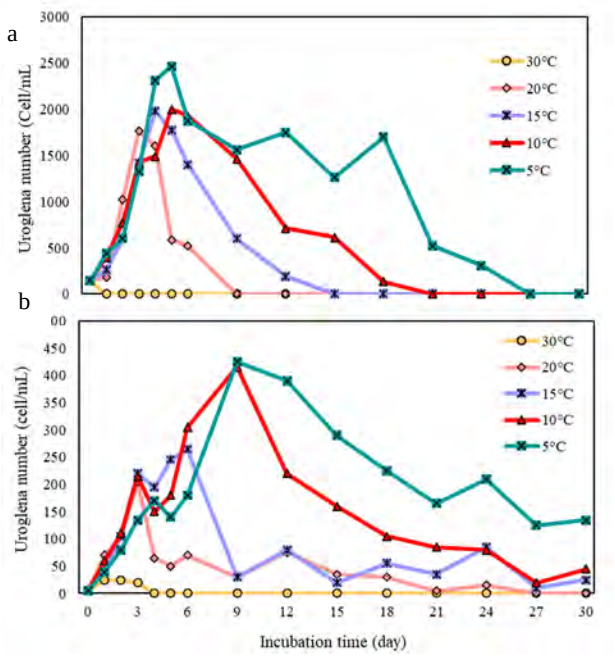

Fig. 1: *Uroglena sp.* number during incubation for water sample of a) May and b) September.

Interrelation of *Uroglena sp.* with other parameters

PCA was conducted with the aim of showing parameters that have positive and negative relationships with *Uroglena sp.*

The PCA results in the May sample demonstrate the similarity through clustering among *Uroglena sp.*, several microalgae (*Peridinium sp.*, *Chlamydomonas sp.*, and *Lepocinclis sp.*), pH, and nutrients such as DN and DP. However, other parameters such as microalgae (*Sphaerocystis sp.*, *Gelonkinia sp.*, *Scenedesmus sp.*, and *Nitzchia sp.*), total bacteria (16SrDNA), UV260, DOC, ORP, and DO were divergent from *Uroglena sp.*

As for the September results *Uroglena sp.* samples were in the same clustering with several microalgae species (*Microcystis sp.*, *Lepocinclis sp.*, and *Mallomonas sp.*), DP, DO, and UV260. While total bacteria and other parameters diverged from *Uroglena sp.*

The results of this analysis show that several parameters have a consistent relationship with *Uroglena sp.* in both incubation samples, both positive relationships such as DP and microalgae (*Lepocinclis sp.*) and negative relationships such as total bacteria, microalgae (*Sphaerocystis sp.*, *Scenedesmus sp.*, and *Nitzchia sp.*).

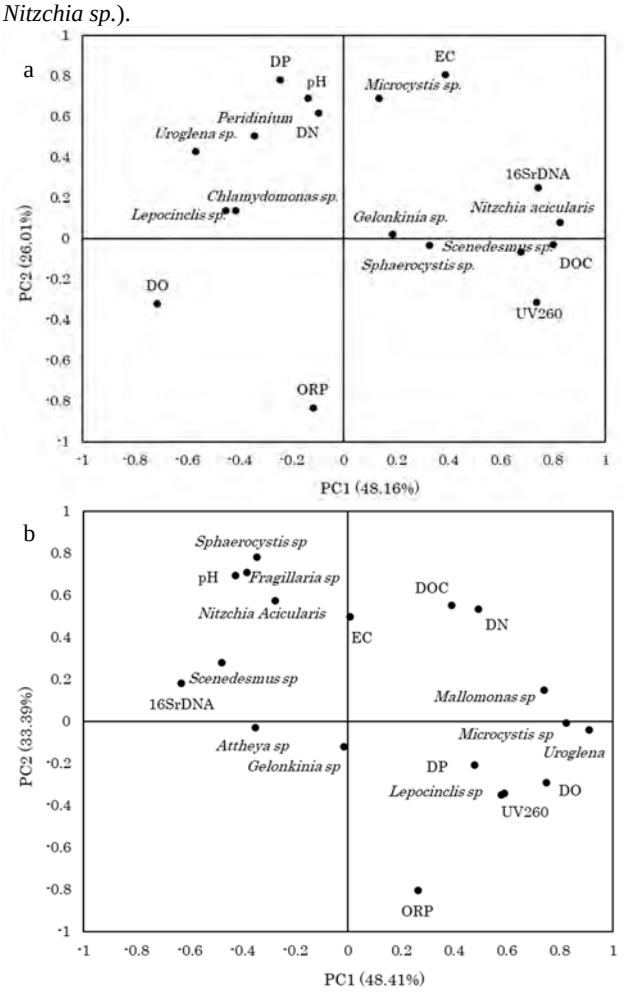

Fig. 2: Principal Component Analysis of interrelation *Uroglena sp.* and other parameters for water sample of a) May and b) September

Relationship between *Uroglena sp.* and bacteria (16SrDNA)

In this study, total bacteria had a negative relationship with *Uroglena sp.;* this result was consistent in both incubation samples.

The initial bacterial count in the September sample was higher than the May sample at $7.5x10^9$ copies/L and $8.7x10^8$ copies/L, respectively. The number of bacteria continued to increase in the May sample, while the number of bacteria in the September sample decreased slightly at low temperatures, only at high temperatures did the number of bacteria increase.

Higher temperatures can promote the growth of bacteria that can affect the growth of *Uroglena sp*. Although *Uroglena sp.* is a photo-phagotrophic organism that ingests bacteria for nutritional purposes. However, the results of this study show an excess number of bacteria (>$1x10^{10}$ copies/L) at high temperatures can inhibit the growth of *Uroglena sp*. This might be due to the inability of *Uroglena sp.* to compete with bacteria for nutrient uptake.

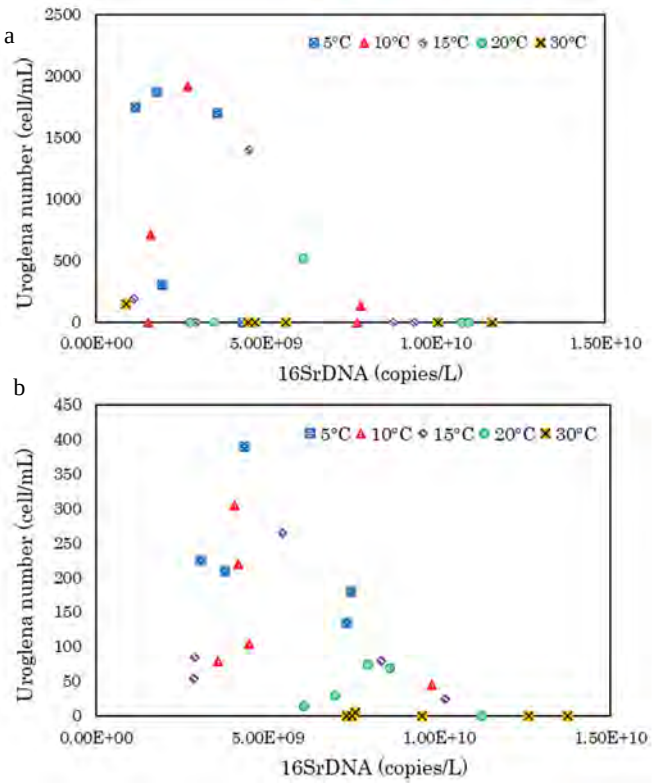

Fig. 3: The relationship of *Uroglena sp.* with bacteria (16SrDNA) during incubation for samples of a) May and b) September

CONCLUSION

The growth of *Uroglena sp.* was the highest at 5 ˚C in May and September incubation samples, but *Uroglena sp.* grew longer in the September sample. The growth of *Uroglena sp.* has a negative relationship with bacteria. Excessive amounts of bacteria may inhibit the growth of *Uroglena sp.*

REFERENCES

Kimura Bon. 1989. Studies on Chemical and Biological Factors Influencing in the Growth of *Uroglena Americana*, a Red Tide Chrysophyceae in Lake Biwa. The Journal of Shimonoseki of Fisheries. 38, 23-70.

Green W. R., Hufhines B. 2017. A rare Uroglena bloom in Beaver Lake, Arkansas, spring 2015. Lake Reserve Management. 33, 8-1

The United Graduate School of Agricultural Science, Gifu University
1-1 Yanagido, Gifu 501-1193, Japan
Tel: +81-58-293-2984 (or, 2985)
E-mail: renno@gifu-u.ac.jp
Home Page: http://www.ugsas.gifu-u.ac.jp/eng/

Promotion Office of Gifu University Rearing Program
for Basin Water Environmental Leaders, Gifu University
1-1 Yanagido, Gifu 501-1193, Japan
Tel: +81-58-293-2085
E-mail: bwel@green.gifu-u.ac.jp
Home Page: https://www.green.gifu-u.ac.jp/BWEL/eng/index.html

ISBN978-4-909365-08-8